The Pennsylvania State University

The Graduate School

College of Engineering

PHOTONIC ENGINEERING FOR BIOLOGICAL STUDY

A Thesis in

Electrical Engineering

by

Fei Wu

© 2006 Fei Wu

Submitted in Partial Fulfillment
of the Requirements
for the Degree of

Doctor of Philosophy

December, 2006

The thesis of Fei Wu was reviewed and approved* by the following:

Shizhuo Yin
Professor of Electrical Engineering Department
Thesis Adviser
Chair of Committee

Karl M. Reichard
Assistant Professor of Acoustics

Timothy J. Kane
Associate Professor of Electrical Engineering and Meteorology

Zhiwen Liu
Assistant Professor of Electrical Engineering

W. Kennneth Jenkins
Professor of Electrical Engineering
Head of the Department of Electrical Engineering

*Signatures are on file in the Graduate School.

ABSTRACT

My dissertation focuses on designing and developing prototypes of optical tools in the laboratory that can facilitate practical medical therapies. More specifically, this dissertation examines two novel biophotonic techniques: 1) a frequency multiplexed confocal microscope with the potential to provide rational therapy of congestive heart failure (CHF), and 2) the “optical comb” with the potential to improve results of retina reattachment surgery and accelerate post surgical recovery. Next, I will discuss the background, design and initial experimental results of each study individually.

Part I: The Frequency Multiplexed Confocal Microscope

CHF is one of the largest threats to human health currently. Nearly 5 million Americans are living with heart failure, and 550,000 new cases are diagnosed each year. Observations on humans as well as experimental animal models indicate that heart cell (myocyte) contractile abnormalities partly account for pump dysfunction observed in the heart disease state which leads to CHF. Therefore, understanding the mechanisms by which contraction in a single myocyte is regulated is important in our quest for effective therapy for CHF. Recently high-resolution imaging suggests that the ion transporters involved in cardiac excitation-contraction coupling are grouped together to defined regions (t-tubules and triads) of the cardiac cell membrane. Despite the important question of whether these small domains do

indeed exist in the cardiac myocytes, there is no straight-forward approach published to-date to quantify and to track simultaneous changes of calcium ion and sodium ion concentration in a living cardiac myocyte during an action potential.

Fluorescence confocal microscopy is a powerful tool for life science because of its capability to optically section a thick specimen and obtain the 3-D image of that sample. However, a conventional confocal microscope requires pixel-by-pixel scanning, and as a result, has poor temporal resolution (i.e. slow imaging speed), which makes it difficult to monitor the fast dynamics in cells. To overcome the limitations of existing confocal microscope technology, this dissertation proposes a non-scanning, real-time, high resolution technique (a multi-point frequency multiplexed confocal microscope) to measure 3-D intracellular calcium ion concentration in a living cardiac myocyte. This method can be also applied to measure the intracellular sodium ion concentration, or other ions in which high quantum-yield fluorescent probes are available. The novelty of the proposed research lies in the introduction of carrier frequency multiplexing techniques which can differentiate fluorescence emitted at different spatial locations in cardiac myocyte by their modulated frequency. It therefore opens the possibility to visualize the transient dynamics of intracellular dynamics at multiple locations in cells simultaneously, which will shine a new light on our understanding of CHF.

The procedure for frequency multiplexing proposed is described below. Multiple incident laser beams are focused onto different locations in an isolated rat cardiac myocyte with each beam modulated at a different carrier frequency. The fluorescence emission at each location therefore bears the same modulated frequency as the stimulation laser beam. Each fluorescence signal is sent to the photo multiplier tube (PMT) after being spatially filtered by a single mode fiber (functioning as a pinhole). Since each signal has a different carrier frequency, only one signal detector is required to collect multiple signal streams which eliminates the errors introduced by difference of multiple detectors. After taking the Fourier Transform of the collected data, multiple peaks can be found in the frequency domain. Each peak refers to a corresponding location in the sample. The temporal information of the fluorescence signal variation at each location can be obtained by demodulating the low frequency information from the carrier frequency, followed by an inverse Fourier transform.

Part II: The “Optical Comb”

Retinal detachment refers to separation of the inner layers of the retina from the underlying retinal pigment epithelium. It can cause degeneration of the retina and may lead to permanent vision loss if not promptly treated and hence is considered an ocular emergency. Currently, the only treatment available for retinal detachment is surgical reattachment.

Recent research findings provide a new explanation for the mechanism of visual loss due to detachment. Diffusion caused by the detached retina is but one of the factors of visual impairment, another factor could be the misalignment of the photoreceptors. During post surgery recovery, the photoreceptors and pigment epithelium regenerate and regain original contour; thus the vision may continue to improve over many months. To accelerate the recovery, ways to enhance photoreceptor realignment are required. In the second part of my dissertation, a novel technique called “optical comb” is proposed to tackle the problem.

The idea of an “optical comb” is developed from the general working principle of the well known “optical tweezers” in the optical literature, which can pull micro-objects through the trapping force produced by a focused laser beam. If we can manage to incident the focused laser beam onto the misaligned photoreceptors and further scan it back and forth, trapping forces that produced may be able to “comb” the photoreceptors to be aligned, and thereby help with post surgery recovery. A series of experiments have been carried out to demonstrate the plausibility of this idea. First, several micro glass rods with size similar to human’s photoreceptors (6 microns in diameter and 30 microns in length) were used. We observed that when the laser beam is focused close to one end of the micro rod originally laid on a glass coverslip, the rod is pulled to stand upright successfully, and we can manipulate the direction it faces by controlling its relative position to the laser beam. We are now experimenting with this combing technique with detached bovine retina samples to further verify its feasibility over live animal cells.

TABLE OF CONTENTS

LIST OF FIGURES

ACKNOWLEDGEMENTS

I would like to gratefully acknowledge the enthusiastic supervision of Dr. Shizhuo Yin during this work. I also thank Dr. Xueqian Zhang and Dr. Zhiwen Liu for their generous help and insightful suggestions. I would like to give my deeply thanks to my committee members, Prof. Karl M. Reichard and Prof. Timothy J. Kane, for their timely and generous support on this study. All members of Electro-Optics Laboratory in Electrical Engineering Department are also recognized and acknowledged.

I am deeply indebted to my parents Jingru Li and Zhaoming Wu, my brother and sister in Law Tong Wu and Yin Mo for their understanding, endless patience and encouragement when it was most required. Finally, I am grateful to my wife, Yan Wu for her assistance, support in many ways.

PART I: FREQUENCY DIVISION MULTIPLEXED MULTI-CHANNEL HIGH SPEED FLUORESCENCE CONFOCAL MICROSOCPE

Chapter 1: Introduction to Confocal Microscope

1.1 Introduction

The patent filed by M. Minsky [1], named double focusing stage scanning microscope and dated 1961, is the earliest prototype of the confocal microscope. It is only in 1975 that the first operational confocal microscope system was demonstrated at Oxford University by Sheppard et al [2], and the first confocal microscope image was produced in 1977. Despite the early quietness of this technology, confocal microscopy has become an effective tool in many disciplines ranging from biological research to semiconductor manufacturing and has proven to be one of the most exciting advances in optical microscopy in the last century [3].

A typical arrangement of a confocal microscope is shown in Figure 1.1. The light from the focal plane of the objective lens is focused through a small aperture (confocal pinhole) on the detector. In comparison, most of light from out of focus planes is blocked. Because this aperture is optically conjugate to the spot focused within the specimen, it preferentially excludes signals emanating from other than the plane of focus. Therefore, the confocal microscope has a unique optical sectioning feature so that a high signal-to-noise-ratio (SNR) image of a incredibly thin slice section can be obtained over the thick scattering media (e.g., a cell). Furthermore, the resolution in the lateral

direction can be improved by a factor of up to two [4], according to the Raleigh criterion, the point spread function is sharpened by a factor of 1.4 relative to a conventional system of the same aperture.

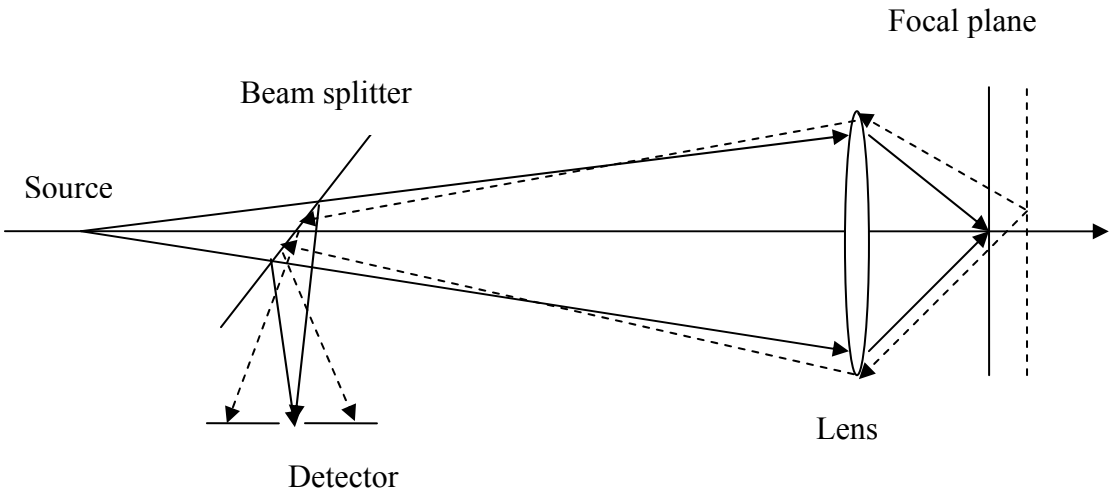

Figure 1.1 The origin of the depth discrimination in confocal optical systems

A confocal microscope can operate either in a bright field (reflection or transmittance) mode or a fluorescence mode. In biomedical applications, fluorescence confocal microscopy is most commonly used for detecting fluorescent labels. When used in the fluorescent mode, this system has the effect of producing an image in which the detected signal intensity closely approximates the stain density at the focused plane.

In a traditional confocal microscope design, the parallel processing requirement of an optical system is relaxed and only one object point is imaged at a time. Scanning the entire field of view is necessary to obtain the whole two dimensional image. A possible drawback to this approach concerns the relatively slow speed of image acquisition which should be sufficiently short to prevent motion artifacts.

In the past several decades, several types of confocal microscopes were developed [8-13] to achieve high imaging speed. In a point scanning confocal microscope, one of the scanners has to operate at a high speed (15,700lines/s) to achieve the video rate of 30 frames/second. Alternatively, the sample can be simultaneously illuminated with multiple foci, as in a tandem scanning confocal microscope that uses a spinning Nipkow disk. A modified version of this microscope improves light-collecting efficiency by incorporating microlenses into the Nipkow disk, making it suitable for fluorescence imaging. Multifocal excitation and parallel detection with microlens arrays have also been reported for multiphoton microscopy [9]. A new method for the reflectance imaging uses a dispersive grating to spectrally map the output of a broadband light source onto a parallel array of foci, thus eliminating the need to scan in the fast axis [8, 12, and 14]. Unfortunately, although several types of multi-channel confocal microscopic techniques were developed, it is very difficult to directly apply these techniques to the fluorescence confocal microscope without sacrificing the imaging quality. For example, since the emission wavelength of the fluorescent light is determined by the fluorescent label, which is independent of the wavelength of the incident exciting beam, the wavelength division multiplexing technique [8, 10, 11, and 14] can not be applied. Another major challenge comes from the weak fluorescent signal. To effectively detect the weak fluorescent signal, a PMT is usually used. In general, a PMT is a single pixel detector. However, many multiplexing techniques (such as

using microlens and pinhole arrays [9]) require a highly sensitive imaging detector (i.e., an array of detectors). Note that although PMT arrays have very recently been used as the detection modules (e.g., Zeiss' LSM 510 META detection module), they usually have a very limited number of pixels (e.g., 32). In addition, these PMT array based detection modules are very expensive. On the other hand, the sensitivity of the CCD based imaging detector is limited by the imaging speed. At the same SNR level, the higher the sensitivity, the lower the speed is. A commonly available CCD imaging detector used for this application has a frame rate of around 30 frames/second (i.e., the video rate), which is not fast enough to monitor fast dynamics in cells. The high speed CMOS-based-imaging detector has a feature of fast optical sensing, however it is limited by its high noise level caused by the comparatively complex device design and the current semiconductor processing technique.

Nearly 5 million Americans are living with congestive heart failure (CHF), and 550,000 new cases are diagnosed each year (http://texasheart.org/HIC/Topics/Cond/CHF.cfm). Understanding excitation-contraction abnormalities of cardiac cells in disease states is important for rational therapy to be designed. To study fast dynamic biological behavior (e.g., the cardiac myocyte contraction), it would be great if a fast imaging speed confocal microscope were available. For instance, a long-standing problem in cardiac research is how to obtain the transient 3D distribution of calcium in a cardiac myocyte during excitation-contraction [5, 6, and 7]. In cardiac cells, ion concentrations (especially Ca^{2+}) fluctuate within the cell on a beat-to-beat basis. Precise information of ion distributions and dynamics is crucial for understanding not only normal physiology at the cellular level but also alterations in ion homeostasis in pathophysiological states.

Recent experimental data imply, but do not directly prove, that ion concentrations just under the cardiac cell membrane (submembranous domain) may be substantially different than those measured in bulk cytosol. For example, the measured equilibrium potential of Na^+/Ca^{2+} exchanger showed that the submembranous Na^+ concentration was 7 times higher than that measured in bulk cytosol. In addition, tail currents measurements of the Na+/Ca^{2+} exchanger, after the action potential was interrupted, exceeded the values that would be expected from the bulk cytosolic Ca^{2+} concentration, suggesting much higher Ca^{2+} concentrations in the submembranous region. The situation is further complicated by the observed Ca^{2+} sparks, localized release of Ca^{2+} from the sarcoplasmic reticulum, in the cardiac cell. Despite these intriguing observations, to-date there is no published literature on the simultaneous determination of submembranous and cytosolic ion concentrations during a cardiac contraction cycle. This is most likely due to the fact that currently there are no methodologies which can provide satisfactory data with both high time and spatial resolution for ion distributions and dynamics in the myocytes. In engineering terms, no existing technique can simultaneously allow for both high spatial and temporal resolution for tracking multiple fluorescence points in cells.

To overcome the limitations of the existing confocal technology, in this chapter, we present a non-scanning multi-point fluorescence confocal microscope via FDM technique, which not only has a high spatial resolution but also has a high temporal resolution (up to the ns range, only limited by the life time of the fluorophores and the response time of the PMT). This technology can be applied to both the PMT and the PMT array based detection modules. In both cases, it increases the effective number of pixels (i.e., the number of pixels in the PMT multiplies the number of the frequency

division multiplexed channels) in the detection module. Thus, we expect this frequency division multiplexed fluorescence confocal microscope can be a very effective tool to study the transient dynamics in living cells.

1.2 Working principle of the FDM confocal microscope

Comparing with a traditional confocal microscope design (shown in Figure 1.1), the proposed design has several unique features. First, the incident stimulating laser beams are modulated at different carrier frequencies; second, the single mode fibers replace the generally used pin holes or slits as the spatial filter in front of photo detectors; third, there are incident angles when multiple stimulating laser beams are coupled into the objective lens; fourth, the design can be implemented either in reflectance/transmittance or fluorescent mode.

Frequency division multiplexing (FDM) has been widely used in telecommunication, television cable service and many other areas for a long time. The underlying reason is that many systems used for transmitting signals provide more bandwidth than that is required for any one signal (the individual signals to be transmitted are assumed to be band limited), and it is straightforward to modulate the individual signals at different carrier frequencies. The modulated signals are then summed and transmitted simultaneously over the same communication channel. The carrier frequencies are carefully designed so that the spectra of the modulated sub-channels do not overlap to each other. Through the multiplexing process, the individual input signals are allocated distinct segments of the frequency band. To recover the individual channels in the de-multiplexing process, it requires two basic steps: band-pass filtering to extract the modulated signal corresponding to a specific channel in the frequency domain, followed by demodulation to recover the original signal.

In our design, the transmitting systems are single mode fibers and fluorescence signals from different locations of the sample are the individual signals.

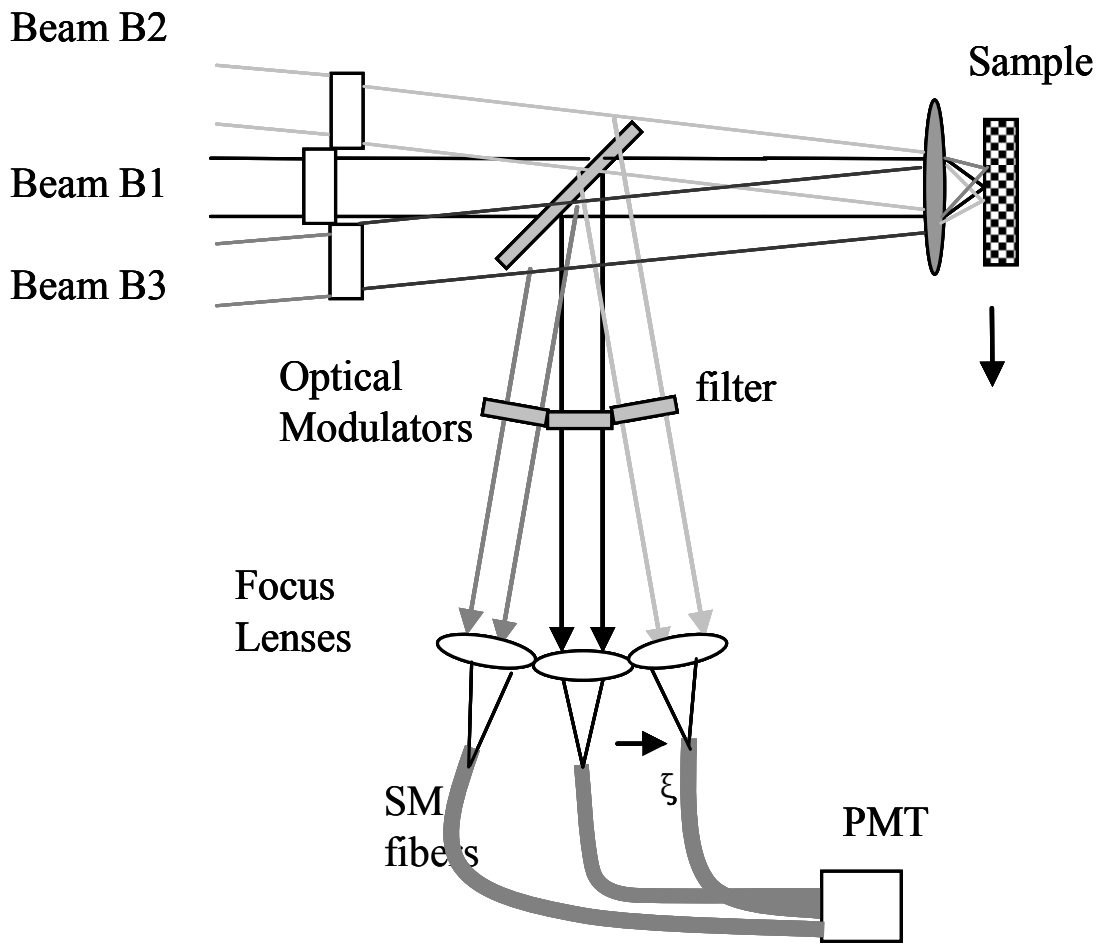

Figure 1.2 an illustration of multi-channel confocal architecture by using multiple optical fibers and a single PMT photodetector

The fiber-optical multi-channel confocal microscope in reflectance or fluorescence mode is schematically shown in Figure 1.2. This microscope design can also work in transmittance mode by slight revision of the setup. Multiple TEM_{00} Gaussian beams with equal intensity from the same laser source, but slightly different incident angles are coupled into the back aperture of the imaging objective lens. The incident laser beams are focused to different locations by the objective lens on the object plane because of the different incident angles. The incident laser beams are intensity modulated at different carrier frequencies. The reflectance or fluorescence signal emitted at each point therefore inherits the carrier frequency of the stimulating laser beam. Each signal is collimated back by the same objective lens and coupled into different single mode (SM) optical fibers via corresponding focus lens in front of each fiber end. Finally the signals from different locations in the detected sample, guided by multiple SM fibers, are detected by a single photo multiplier tube (PMT).

The point detector is the key element in a confocal microscope system and is usually realized by placing a small pinhole in front of the photodetector. As all the considerable advantages of confocal microscopy follow directly from the use of a point detector, it is important to know how small a practical detector must be in order to approximate a true point detector. It is reasonable, in general, to try to use as small a detector as possible, although in many applications we may not have this freedom because of signal-to-noise problems. This is particularly true in the imaging of weakly fluorescing biological samples. It is therefore necessary to discuss how the strength of the optical sectioning property deteriorates as the detector becomes larger. The choice of suitable size and shape of a pinhole has been discussed for both the bright field and the fluorescence imaging mode [15-21]. The finite sized detector results in partially coherent imaging in bright field mode, compared to incoherent imaging in fluorescence mode. However, in certain cases, it is more flexible to use the

optical fiber as the spatial filter instead of pinholes [22-24]. In our design, we use single mode fibers because it is convenient to combine fluorescence signals from different channels and output them to a single photodetector, which makes the signal detection part compact and flexible.

1.2.1 Brightfield mode

In order to analyze how optical fibers function as spatial filters in the confocal microscope, we need to obtain the field amplitude at the end surface of the fibers. In terms of Snyder and Love [25], an arbitrary electrical field $U(x,z)$ can be expanded as a superposition of a complete set of orthonormal modes in an optical fiber [25] as follows:

$$U(x,z) = \sum a_j e_j(x) \exp(i\beta_j z) \qquad (1.1)$$

Where $e_j(x)\exp(i\beta_j z)$ is a complete set of the modes in a particular optical fiber and propagates along the z direction without attenuation, β_j is the propagation constant and a_j is the modal amplitude. The detected field of the PMT is given by an overlap integral over the area between the incident optical field at the fiber face and the mode pattern of the fiber.

$$I = \left| \iint_s U(x, z=0) \cdot e_1 dS \right|^2 \qquad (1.2)$$

Where e_1 denotes the profile of the TEM_{00} mode in the fiber, and S is the cross-section area of the fiber. We can then introduce an effective point spread function $h_{2eff}(x)$ of the fiber and focus lens [24], given by:

$$h_{2eff}(x) = h_2(x) \otimes e_1(x) \qquad (1.3)$$

Where $h_2(x)$ refers to the point spread function of the focus lens in front of the SM fiber. From above derivation, it is not difficult to find out that the single-mode fiber acts as a coherent detector [24] which is an important feature of the confocal microscope in brightfield mode. This ensures that the imaging is always coherent irrespective of the fiber dimensions and gives the possibility of performing coherent signal processing at the same time as signal detection. Hence, it makes the coherent signal processing possible.

Alternatively we can describe the above derivation results in terms of an effective pupil function. Recalling that the point spread function is given, essentially, by the Fourier transform of the pupil function of the objective, we can write the effective pupil function P_{2eff} from Eq. (1.3) as

$$P_{2eff} = P_2 \cdot E_1 \qquad (1.4)$$

where P_2 is the pupil function of the objective lens and E_1 is the Fourier transform of e_1. Thus the effect of the detector may be thought of as introducing an effective filter of amplitude transmittance E_1. Thus the question as how closely a confocal microscope with an optical fiber

detector resembles a true confocal microscope with a point detector can be answered by discussing how E_1 varies over the extent of pupil P_2.

To analyze the imaging formation in our multi-point fluorescence confocal system, we first consider the one-dimensional case and a single-channel fiber-optical reflectance confocal microscope which the excited laser beam normally incidents into the back aperture of the objective lens for simplicity [26]. The point spread function is given by:

$$g_1(x) = h_1(x_1)\left[e_1^*\left(x/M_2\right) \otimes h_2(x)\right] = h_1(x_1)h_{2eff}(x) \qquad (1.4)$$

$h_1(x_1)$ and $h_2\left(\frac{x}{M_2}\right)$ are point spread functions of the objective lens and focus lens in front of the SM optical fiber.

When the laser beam has an incident angle θ to the optical axis of the imaging objective lens, the point spread function of the system considering the incident angle can be correspondingly revised to

$$g_1(\zeta) = h_1(x_1)\exp(j\mu_0 x_1)\left[e_1^*\left(x/M_2\right) \otimes h_2(x)\right] \qquad (1.5)$$

Where ζ is the spatial frequency of the incident angle and can be expressed as $\frac{Sin\theta}{\lambda}$; $M_2 = \frac{f_2}{f_1}$ are the magnifications of the objective lens and the focus lens, f_1 and f_2 are the focal length of objective lens and the focus lens correspondingly.

Correspondingly, the in-focus optical transfer function is

$$c(l) = P_1\left[\lambda f_1\left(l + \frac{\zeta}{f_1}\right)\right] \otimes \left[E(M_1 l) P_2(\lambda f_2 l)\right] \qquad (1.6)$$

Where $P_1(\lambda f_1 l), P_2(\lambda f_2 l)$ are the pupil functions of the objective lens and the focus lens separately, $E(l)$ is the Fourier transforms of $e_1(x)$ and l is the radial spatial frequency in the transverse direction in the case of circular single-mode fibers and circular pupil functions of the lenses. If $e_1(x)$ is a delta function that refers to a point detector, then $E(l)$=1; and if ζ is 0 corresponding to zero incident angle of excitation laser beam, Equation (1.6) reduces to the coherent transfer function of the traditional confocal microscope.

The numerical calculations of Equation (1.6) are plotted in Figure 1.3, compared with the coherent transfer function of the traditional confocal microscope with a point source and a point detector, corresponding to the parameter A=0. $A = \left(2\pi a_0 r_0 / \lambda d\right)^2$ is dimensionless fiber spot sizes, a_0 is the objective pupil radius, and d is the focus length of the focus lens [26]. It can be seen that the cutoff spatial frequency is twice that of the conventional microscope. The larger the value of the parameter

A is, the decrease of C(L) is more quickly as the spatial frequency m increases. Eventually, the plots of C(L) become narrow when A becomes a large value.

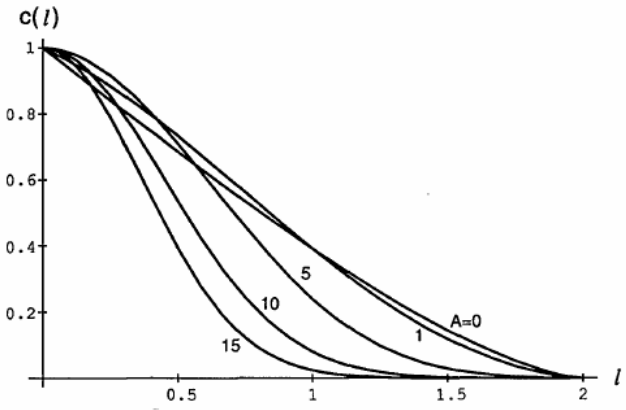

Figure 1.3 In-focus transverse coherent transfer function C(L) for A.

For the defocus case, the pupil function can be expressed as

$$P_1(r,u) = \exp\left[\left(iu/2\right)\left(r/a_0\right)^2\right] \qquad (r < a_0) \qquad (1.7a)$$

$$P_1(r,u) = 0 \qquad (r > a_0) \qquad (1.7b)$$

Where u is an axial optical coordinate and can be expressed as

$$u = \left(8\pi/\lambda\right) z \sin^2\left(\alpha/2\right) \qquad (1.8)$$

$\sin(\alpha/2)$ is the semiangular aperture. If we substitute the Equation (1.7) into Equation (1.6), we can obtain

$$c(l,u) = P_1\left[\lambda f_1\left(l + \frac{\zeta}{f_1}\right), u\right] \otimes \left[F(M_1 l) P_2(\lambda f_2 l, u)\right] \qquad (1.9)$$

To investigate the strength of optical sectioning in this model of system, we first consider a uniform planar object that is scanned through the focus. In this case the amplitude reflectivity $r_f = 1$ corresponds to $R_f = \delta(0)$. Then the detected intensity varying with the axial optical coordinate u is defined as

$$I(u) = \left|c(l=0,u)\right|^2 = \left|\frac{A\{1-\exp[-(A-iu)]\}}{[1-\exp(-A)](A-iu)}\right|^2 \qquad (1.10)$$

Substitute A=0, we can get

$$I(u) = \sin^2(u/2) \Big/ (u/2)^2 \qquad (1.11)$$

The above result complies with the traditional confocal microscope with zero pinhole size. The numerical calculations of Equation (1.10) are shown in Figure 1.4. When A increases, the plots of detected intensity become broad. This effect confirms that the optical sectioning effect decays as A

increases. In Figure 1.4(b), we plot the half width $u_{1/2}$ of the curves I(u) as a function of the dimensionless fiber spot size. The half-width does not change much when A<=1.

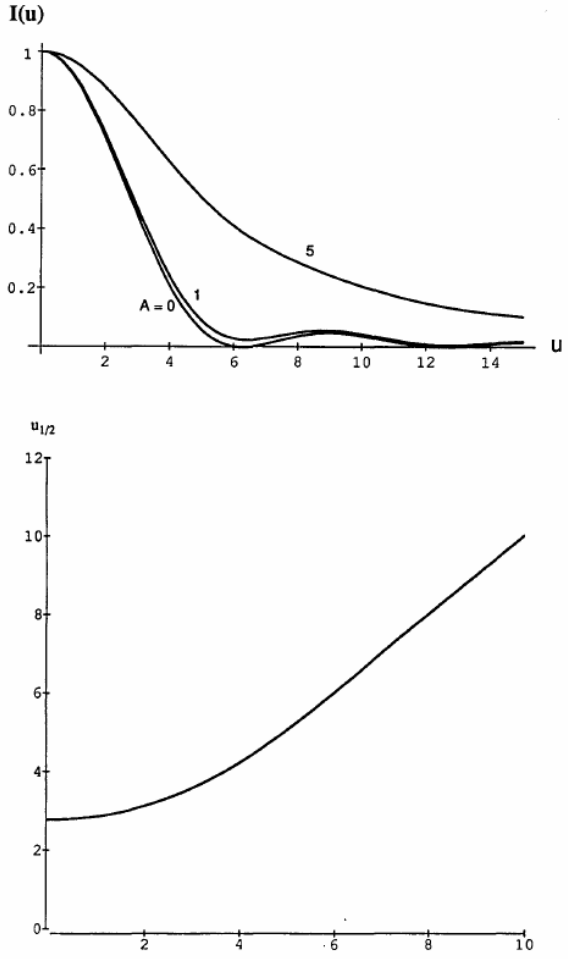

Figure 1.4 (top) Variations of the detected intensity with the axial optical coordinate u in the case of a perfect reflection object.
(bottom) Half-width of the detected intensity of the top figure as a function of the dimensionless fiber spot size A. [26]

1.2.2 Fluorescence mode

If the microscope works in fluorescence mode, the imaging property is different from the above derived results. This is because the fluorescence light is produced by an emitting process of spontaneous radiation, so that the fluorescence light is spatially-incoherent radiation. In other words, the image intensity of a fluorescent object at a given point is the superposition of the intensity from all points in the object; therefore destroys the spatial coherence of the illuminating radiation and produces an incoherent fluorescent field proportional to the illuminating radiation, $I_e(x)$. The stimulation light intensity point spread function $I_i(x)$ can be expressed as

$$I_i(x) = I_e(x) \otimes \left| h_1(x) \exp(j\zeta x) \right|^2 \tag{1.12}$$

And the fluorescence signal detected is

$$I(x) = I_i(x) \left[\left| e_1\left(\frac{x}{\beta M_2}\right) \otimes h_2\left(\frac{x}{\beta}\right) \right|^2 \otimes O(x) \right] \tag{1.13}$$

where $\beta = \frac{\lambda_f}{\lambda e}$ is the ratio of the fluorescence to the stimulating wavelength and O(x) is the fluorescence distribution at object plane of the objective lens.

1.3 Experimental system description

To verify the feasibility of the frequency division multiplexed multi-channel confocal microscope, we build a two-channel experimental demonstration system, which is illustrated in Figure 1.5. The output of a Coherent Innova 300 Argon ion laser at a wavelength of 488nm is divided into two beams by a beam splitter (i.e., BS1 as illustrated in Figure 1.5). The two beams are then intensity modulated at different carrier frequencies of 3000 Hz and 4000 Hz, respectively, by two optical choppers (that were conventionally used for lock-in amplifiers). The two beams are then recombined by another beam splitter (i.e., BS2). After passing through BS3, these two modulated beams are coupled into the back aperture of the objective lens (Nikon, 60x, NA1.4, PlanApo) at slightly different incident angles. The two modulated Gaussian beams are focused at two different locations in the sample (or target) by the objective lens to form two focusing spots. The distance between the two focused points can be adjusted by tuning the relative angle between two incident beams, which can be realized by adjusting the reflection angles of mirrors M1 and M2. The fluorescence emission from the sample at two focusing spots is collected by the same objective lens and reflected to the detection system by BS3. To view the sample and the locations of focusing spots, the fourth beam splitter (BS4) is added in the detection portion of the system. The reflected light from the BS4 is viewed by a CCD imaging system. The transmitted light from the BS4 first passes though a bandpass fluorescence filter, which blocks the exciting laser beams and only transmits the fluorescence light. The transmitted fluorescence light beams from two focusing spots are then focused into two single mode (SM) optical fibers by two focus lenses, as illustrated in Figure 1.5. One fiber corresponds to one spot. The SM fibers serve two functions. First, they are used as pinholes to filter out the out-of-focus light to achieve the confocal imaging. Second, they

allow us to conveniently couple two light beams into a single PMT photodetector (Hamamatsu H7827-002).

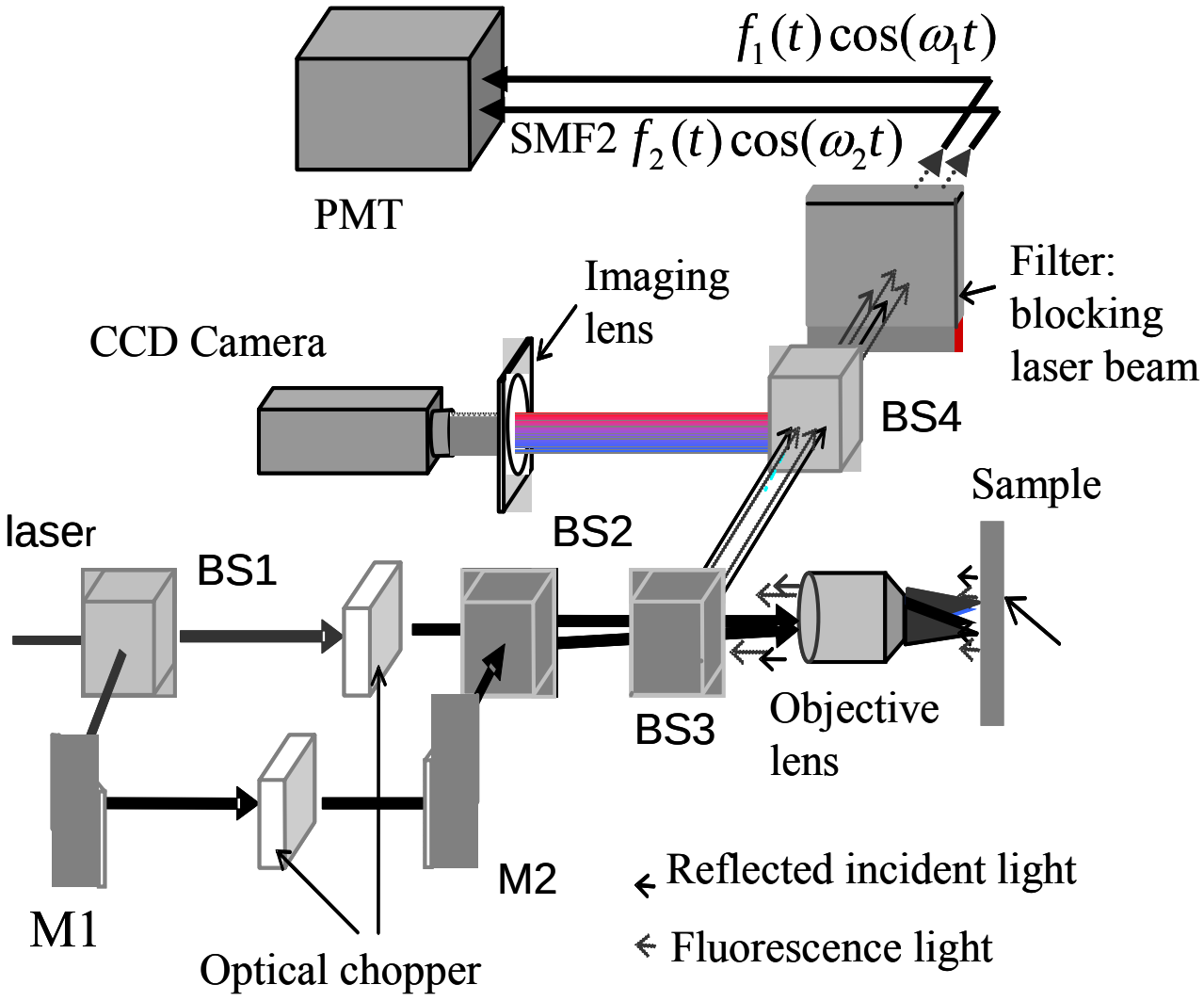

Figure 1.5 an illustration of a two-channel frequency division multiplexed fluorescence confocal microscope. BS: beam splitter; M: mirror.

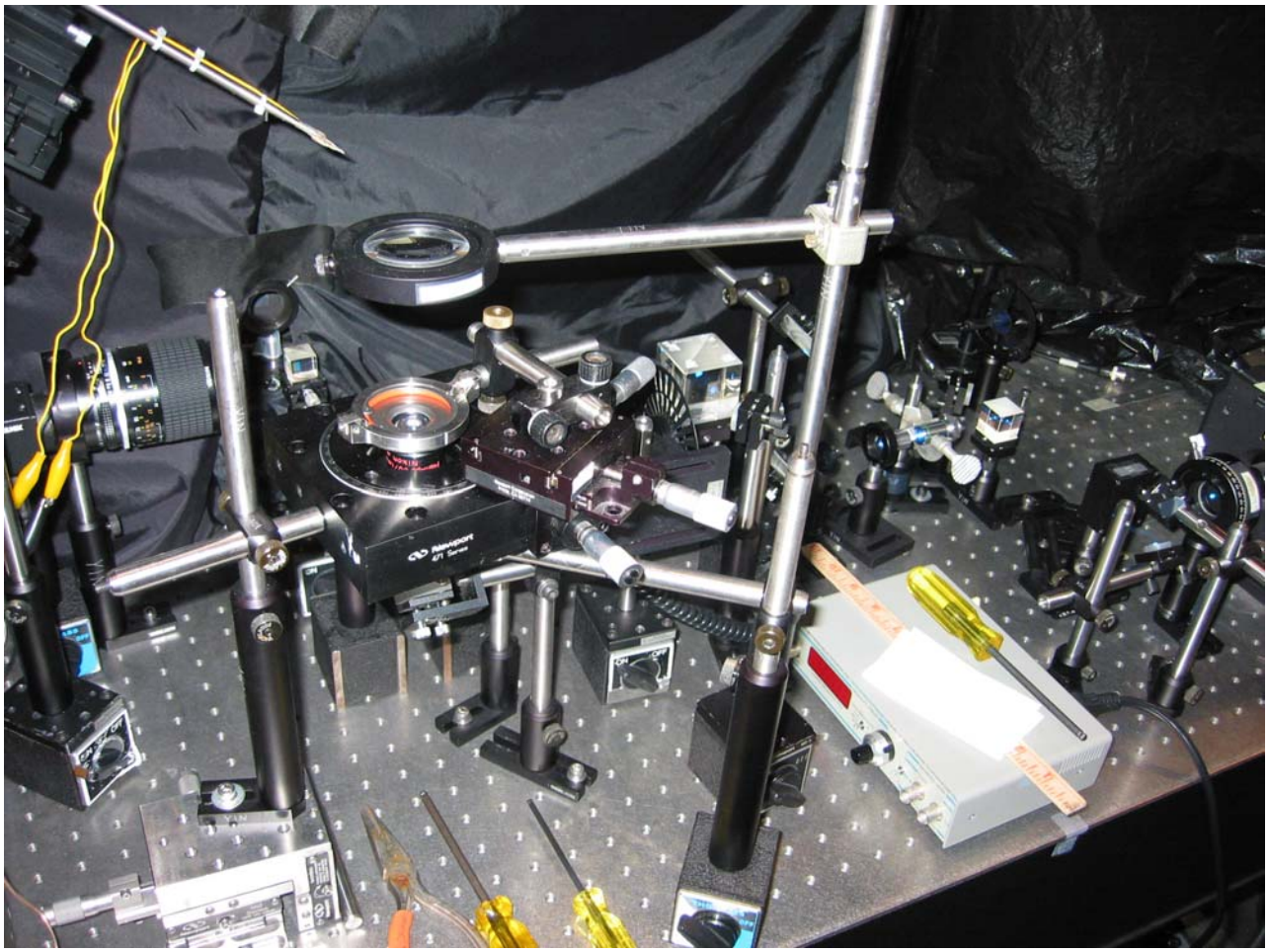

Figure 1.6 Experimental setup of a two-channel FDM confocal microscope on an optical table.

1.3.1 Objective Lens

Microscope manufacturers offer a wide range of objective designs to meet the performance needs of specialized imaging methods. Identification of the properties of individual objectives is usually very easy because important parameters are often inscribed on the outer housing (or barrel) of the objective. The specifications of objective lens are introduced as follows:

1. Numerical Aperture: a critical value that indicates the light acceptance angle, which in turn determines the light gathering power, the resolving power, and depth of field of the objective. To attain higher working numerical apertures, many objectives are designed to image the specimen through another medium that reduces refractive index differences between glass and the imaging medium. The Nikon objective lens in our setup is a high-resolution objective which can achieve numerical apertures up to 1.40 when the immersion medium is special oil with a refractive index of 1.51.

2. Working Distance: the distance between the objective front lens and the closest surface of the cover glass when the specimen is in focus. It is 1.1mm for our objective lens. Most transmitted light objectives are designed to image specimens that are covered by a cover glass (or cover slip). The thickness of these small glass plates is now standardized at 0.17 mm for most applications, although there is often some variation in thickness within a batch of coverslips.

3. Mechanical Tube Length: the length of the microscope body tube between the nosepiece opening, where the objective is mounted, and the top edge of the observation tubes where the oculars (eyepieces) are inserted. Tube length of our objective lens is 160mm.

4. Optical Corrections: the Nikon objective lens in our setup is corrected with grade PlanApo which is the highest degree of correction for spherical, chromatic aberrations and field curvature corrections.

1.3.2 Photodetector-PMT

In a fluorescence confocal microscope, the preferred photodetector is currently a PMT. The exceptional high signal gain of a PMT makes it a perfect photodetector to the extremely weak fluorescence signal output of the confocal microscope. The PMT operates in the following manner: some of the photons impinging on the photocathode (PC) material deposited on the inside of an evacuated glass envelope are absorbed, causing photoelectrons (PE) to be emitted into the vacuum; each PE is drawn toward a nearby electrode, or dynode, held at about 100-200 V positive to the PC; the geometry and materials of the dynode have been chosen to ensure that almost every incoming PE produces a number of secondary electrons (SE). The number produced per incoming PE, the SE coefficient, is roughly proportional to the dynode voltage and varies between 5 and 20 in a PMT operating at high gain [27]; these are in turn attracted to the second dynode, where the process of charge multiplication is repeated; after 10-14 stages, the size of the charge pulse initiated by each PE has been amplified to times, producing a current pulse that can usually be detected by electronic amplifiers without introducing additional noise.

In our setup, a H7827-002 PMT (Hamamastu) incorporating a 19mm (3/4”) diameter head-on photomultiplier tube, a high-voltage power supply circuit and a low noise amplifier is used as the photodetector. This amplifier has a current-to-voltage conversion factor of 0.1V/uA and a frequency bandwidth of DC to 200 kHz.

1.4 Data processing

Assume that the fluorescent light intensities as a function of time for two spots are $f_1(t)$ and $f_2(t)$, respectively. Due to the frequency modulations, the intensities at fiber 1 and fiber 2 are $f_1(t)\cos(\omega_1 t)$ and $f_2(t)\cos(\omega_2 t)$, respectively. The intensity detected by the PMT is then the summation of these two intensities. Mathematically, the detected PMT signal, $s(t)$ can be written as

$$s(t) = f_1(t)\cos(\omega_1 t) + f_2(t)\cos(\omega_2 t) \qquad (1.14)$$

The output from the PMT is sent to a data acquisition board, which converts the analog electric signal to a digital signal. The digital output from the data acquisition board is sent to a personal computer. The personal computer processes the data by taking the Fourier transform of the detected signal, $s(t)$. In the frequency domain, Equation (1.14) can be shown to be,

$$S(\omega) = F_1(\omega - \omega_1) + F_2(\omega - \omega_2) \qquad (1.15)$$

where $S(\omega), F_1(\omega), F_2(\omega)$ denote the Fourier transform of $s(t)$, $f_1(t)$, $f_2(t)$, respectively. As long as the carrier frequencies (i.e., ω_1 and ω_2) and their difference (i.e., $\omega_1 - \omega_2$) are larger than or equal to twice of the highest signal frequency, there will be no overlap between the two signals in the frequency domain, as illustrated in Figure (1.7). Thus, one can easily separate two signals in the frequency domain by using a frequency bandpass filter. Note that it is not difficult to realize the required carrier frequency for this fluorescence confocal microscope application because one can

modulate the light at a speed up to tens of Gigahertz while most dynamic behaviors in the cell are in the Kilohertz range. Therefore, we can real time detect and distinguish fluorescent emissions from multiple points by using a single pixel highly sensitive PMT, which offers the advantages of both high sensitivity and high speed.

The data processing can be done in two different methods. In the first method, we can partition the measured fluorescence signal into many millisecond time windows. For each window, we can perform the Fourier transform and extract the fluorescence signal at the two different carrier frequencies (i.e., corresponding to two different locations). To extract the useful signals, we can integrate over the interested frequency bands with the carrier frequencies as the central frequencies. As a result, the transient dynamics at the two locations can be obtained straightforwardly by plotting the corresponding integration results in a temporal sequence separately. This process is illustrated in Figure 1.8. It can be easily implemented by using Labview with a build-in function short-time Fourier transform (STFT). The benefit of this method is the ability to monitor the experimental results in real-time with millisecond temporal resolution. In the second method, we deal with the whole trunk of data instead of partitioning them into small windows. The data are first saved into a file and stored in the hard disk. When processing the data, the file is first read into the memory of the personal computer and processed. The data processing procedure can be elucidated by Equation (1.16).

$$
\begin{aligned}
&F(\omega) = \int f(t) * \exp(-i\omega t)dt \\
&F_1(\omega) = BandPass[F(\omega)]_{\omega 1}^{\omega 2} \\
&F_2(\omega) = BandPass[F(\omega)]_{\omega 3}^{\omega 4} \\
&f_1(t) = \int F_1(\upsilon)\exp[i\upsilon \cdot t]d\upsilon \\
&\upsilon = \omega - \frac{\omega_2 + \omega_1}{2}; \\
&f_2(t) = \int F_2(\sigma)\exp[i\sigma \cdot t]d\sigma \\
&\sigma = \omega - \frac{\omega_4 + \omega_3}{2};
\end{aligned}
\qquad (1.16)
$$

where $f(t)$ is the signal detected by the PMT and $F(\omega)$ is the its frequency spectrum; $F_1(\omega)$ and $F_2(\omega)$ are the shifted frequency spectra of $f_1(t)$ and $f_2(t)$ respectively, which are the temporal signals at two different locations; $F_1(\upsilon)$ and $F_2(\sigma)$ refer to the frequency spectra of $f_1(t)$ and $f_2(t)$ respectively. The second data processing method helps alleviate the requirement of collecting and processing the data in real time.

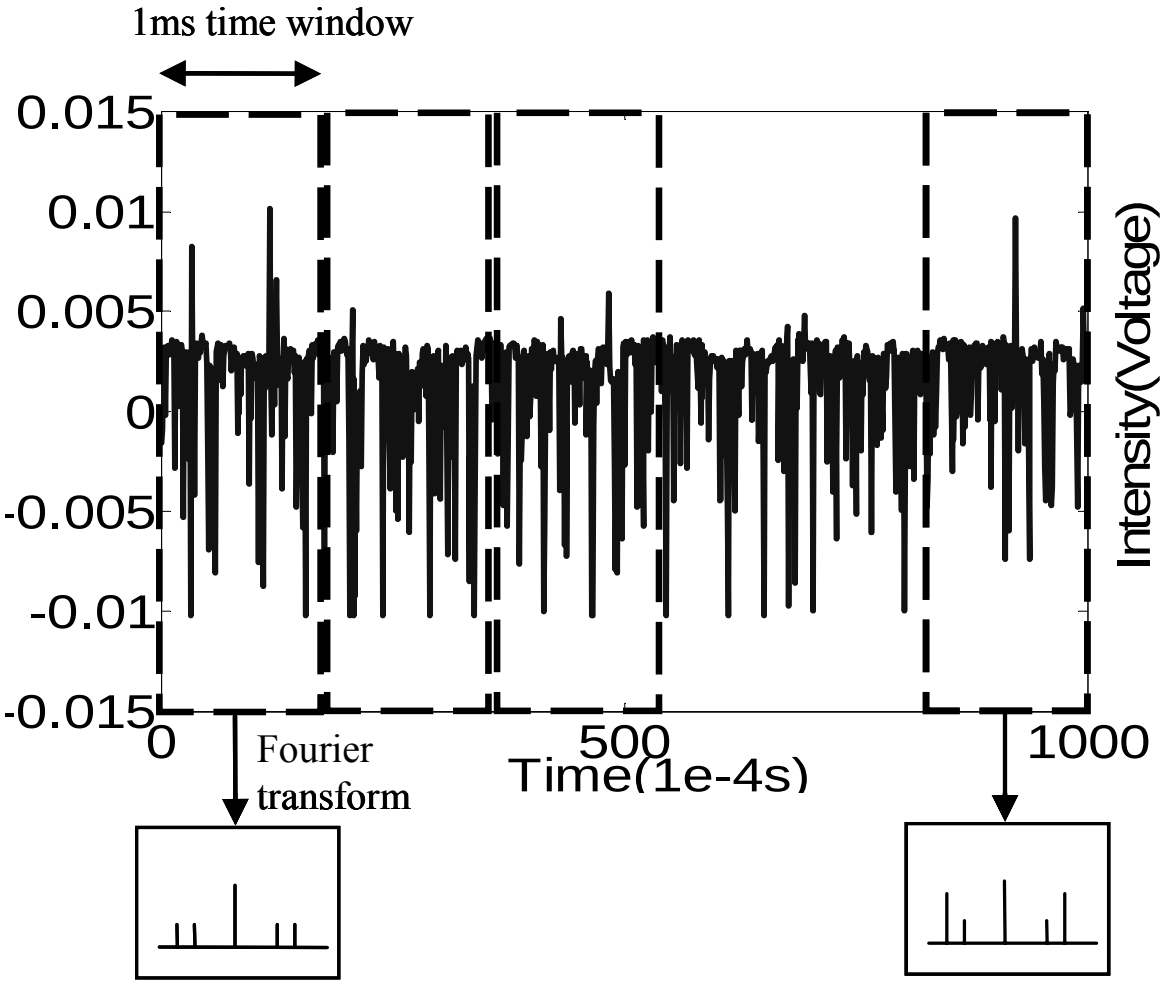

Figure 1.7 Schematic diagram illustrating the process to obtain the temporal signal.

If there were no noise, the simulation results of a beating signal (due to the summation of two sinusoidal waves at different frequencies) would appear as illustrated in Figure 1.9(a). Figure 1.9(b) shows the real experimental signal results from the PMT. Due to the existence of the noise, the beating curve is not as nice as the curve shown in Figure 1.9(a), but one can still see the beating frequency between two sinusoidal waves. Figure 1.10 shows the Fourier transform result of Figure 1.9(b). Two high peaks are obtained, corresponding to two different locations in the detected sample. We can see the two peaks are well separated to each other which indicates that there is no spectrum overlap (crosstalk) between two signals.

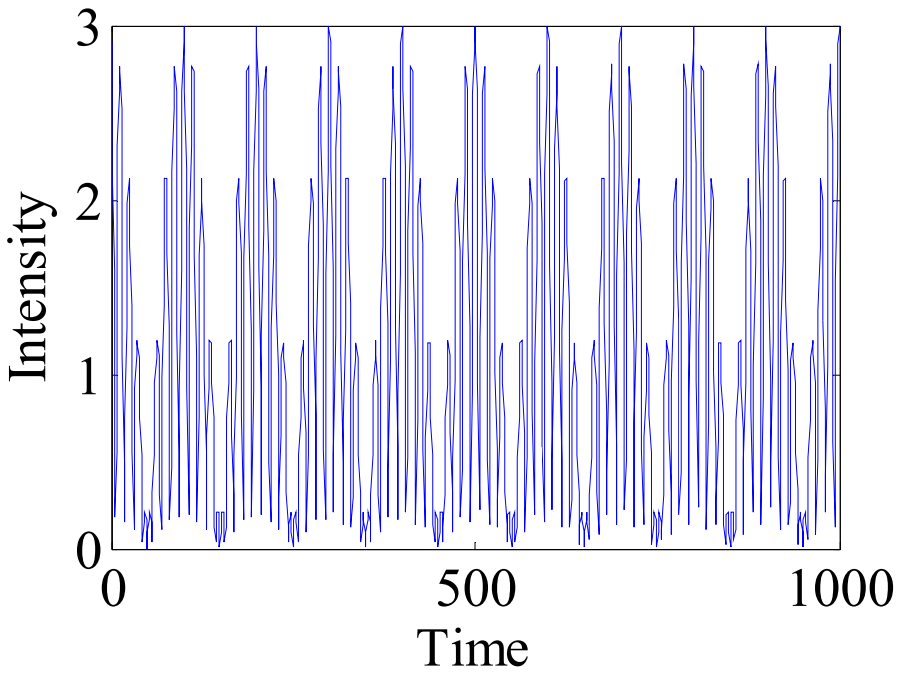

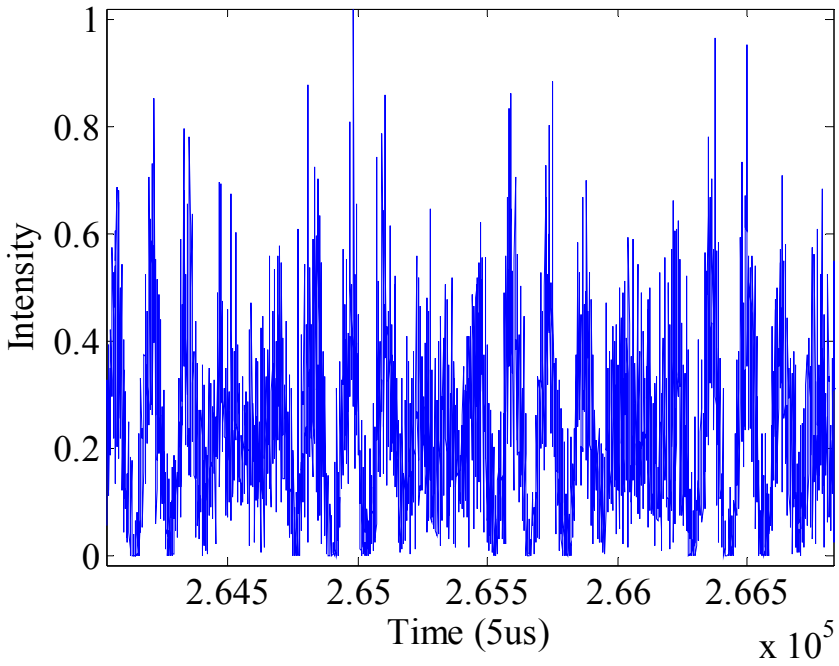

Figure 1.8 (a) simulated noise free signal of a two-channel FDM confocal microscope; (b) Detected signal of a two-channel FDM confocal microscope.

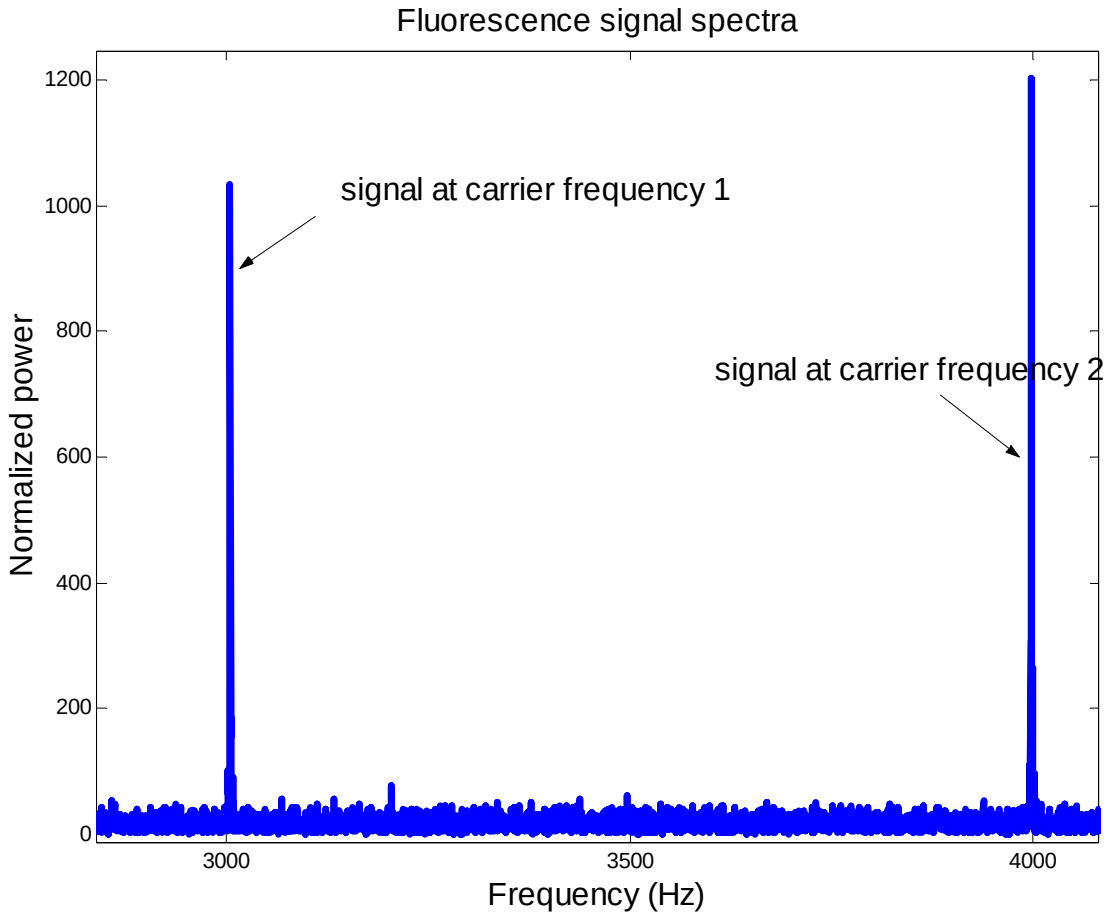

Figure 1.9 detected signal in the frequency domain. The fluorescent signal intensity of each spot can be determined by measuring the intensity of the frequency component at the corresponding carrier frequency.

CHAPTER 2: STUDY THE CALCIUM ION DYNAMICS IN LIVING CARDIAC MYOCYTE

2.1 The Calcium ion dynamics in a living cardiac myocyte

The advances in modern fluorescence microscopy have led to a much deeper understanding of cellular function on the basis of the underlying molecular architecture. The possibility of measuring intracellular ion concentrations with high spatial resolution has significantly contributed to our knowledge about the mechanism of cellular signaling and the very central role of Ca^{2+} ions as the ubiquitous 'second messenger' in cells.

Ca^{2+} ions inside a cell are present in various states as shown in Figure 2.1. Ca^{2+} ions are present as either free ions or bound to various buffer systems, including the fluorescence indicators used in fluorescence microscopic experiments. Additionally, Ca^{2+} ions are sequestered and bound in organelles. In contrast to most other ions, free Ca^{2+} ions are present in very low cytosolic concentrations, ranging between 10-100 nM. Additionally, Ca^{2+} ions are bound to intrinsic and extrinsic intracellular buffers with various amounts of Ca^{2+} binding sites. In experiments using fluorescence techniques, the fluorescence indicator very often acts as the main extrinsic Ca^{2+} ion buffer itself. Also, membrane bound organelles, as e.g. the endoplasmatic reticulum (ER) or mitochondria can sequester Ca^{2+} ions to a very large extend. These different states of Ca^{2+} ions interact by complex processes. In addition to the transport of Ca^{2+} ions by diffusion, Ca^{2+} ions are released from intracellular stores and actively transported by cellular proteins. Ca^{2+} signaling mostly involves transient increases in the intracellular free Ca^{2+} ion concentration (Ca^{2+} transients). Ca^{2+}

ions are derived from two major sources. Either they enter the cell from the extracellular space through ion channels in the external cell membrane driven by the large concentration gradient, or they are released from the internal Calcium ion stores, the ER and the Sarcoplasmic Reticulum (SR), where the free Calcium ion concentration is in the mM range, similar to the extracellular space.

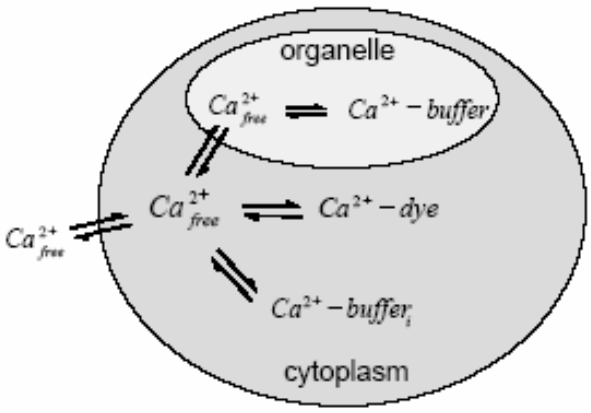

Fig. 2.1 The complex interplay of calcium ions in a cellular environment

Recent high-resolution imaging suggests that the ion transporters involved in cardiac excitation-contraction coupling are grouped together to defined regions (t-tubules and triads) of the cardiac cell membrane [28]. In addition, the cleft space between the L-type Ca^{2+} channel and the SR Ca^{2+} release channel (ryanodine receptor or RYR) is sufficiently small so that on opening of the Ca^{2+} channel, even though only a small amount of Ca^{2+} ions enters the cell, the local Ca^{2+} concentration in this "cleft" between the Ca^{2+} channel and RYR is likely to be substantially higher than that

measured in the myoplasm. Other indirect evidence also suggests the existence of a "submembranous" domain in which the concentration of Ca^{2+} and Na^{+} ions are significantly different than those in bulk myoplasm. Thus, the existence of a submembranous domain with ion concentrations significantly different from those measured in bulk cytosol has major ramifications in terms of understanding the mechanisms of excitation-contraction coupling in the cardiac myocyte.

Despite the importance of answering the question (whether the submembranous domains of Ca^{2+} concentration and Na^{+} concentration do indeed exist in the cardiac myocyte or not), very few studies have provided direct measurements. Using electron microprobe X-ray analysis, Na^{+} concentration in rabbit papillary muscle was reported to be higher near the sarcolemma and fall to levels equal to that in bulk cytosol within 200-300nm of the sarcolemma. It should be noted that electron microprobe X-ray analysis measures total, not free ion concentrations and therefore the apparently increased Na^{+} concentration near the sarcolemma may reflect the binding of Na in the subsarcolemmal space, which could in turn alter the Na^{+} diffusion. In addition, the technique is necessarily destructive, and cannot be used to follow temporal changes in Ca^{2+} concentration and Na^{+} concentration at submembranous domains in a living myocyte stimulated to contract.

2.2 Fluorophores：Fluo-4 and Di-4-ANEPPS

2.2.1 Calcium ion marker Fluo4

Fluo-3 and Fluo-4 are two popular Calcium ion markers made by Invitrogen. Since being introduced in 1989, Fluo-3 has revealed the spatial dynamics of many elementary processes in Calcium ion

signaling. Fluo-4 is an analog of Fluo-3 with the two chlorine substituents replaced by fluorines. This fairly minor structural modification results in increased fluorescence excitation at 488nm and consequently higher signal levels for confocal microscopy. We used both of them in our experiments. At the early stage of the experiments, Fluo-3 is used. However, to improve the signal-to-noise ratio, we later switch to Fluo-4 for stronger fluorescence signal. The emission spectra of Fluo-3 and Fluo-4 are shown in Figure 2.2. We can see the fluorescence emissions of both fluophores saturate at a Calcium concentration level of around 1uM.

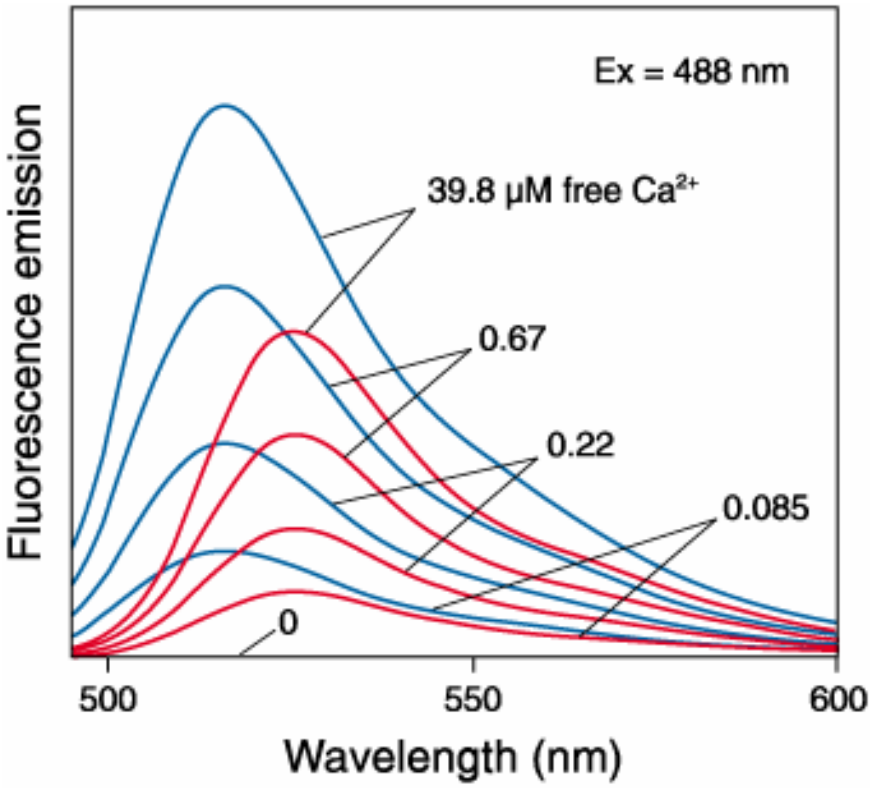

Figure 2.2 shows the emission spectrum of Fluo3 (red) and Fluo-4 (blue).
http://probes.invitrogen.com/handbook/print/1903.html

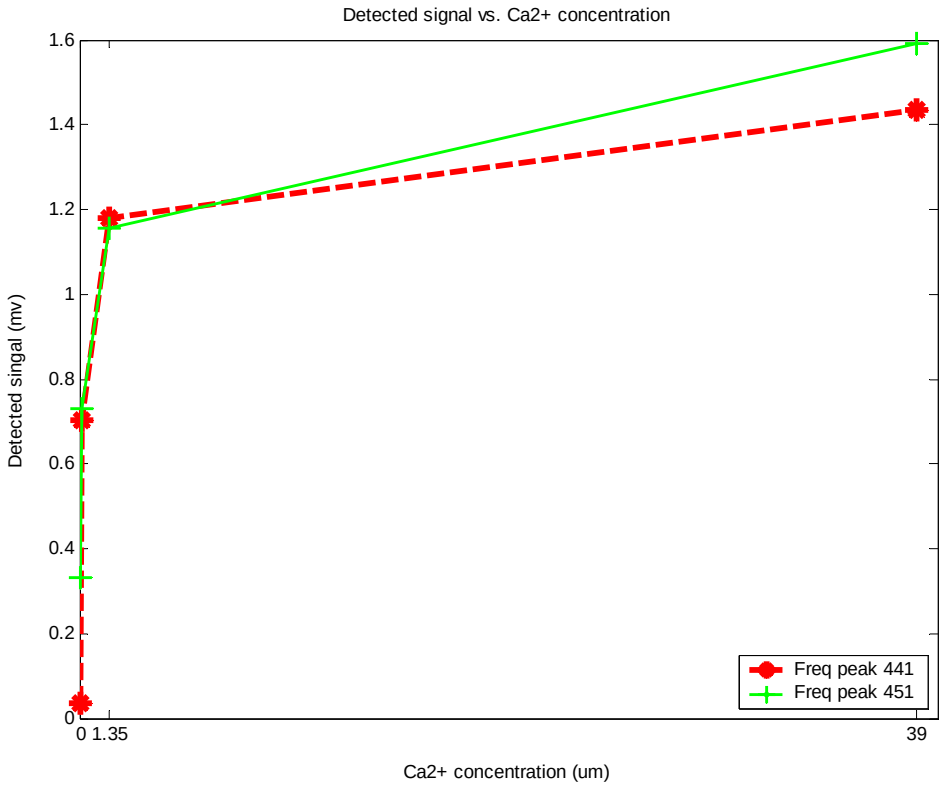

Figure 2.3 Fluorescence signals intensities vs. Calcium ion concentrations.

The Figure 2.3 shows the measured results verses different Calcium ion concentrations using our experimental setup. The two curves correspond to two different incident laser beams. The green curve refers to the detected fluorescent signal excited by laser beam with an intensity of 0.3mw and the red curve is 0.15mw. The fluorescence signal saturates when the Calcium ion concentration is over 1.35uMol. Our data comply with the reported results from Invitrogen. Fluo-5F, Fluo-5N and Fluo-4FF are analogs of Fluo-4 with lower Calcium ion binding affinity, making them suitable for detecting intracellular calcium levels within range of 1uMol-1mMol.

2.2.2 Surface membranes and transverse tubules labeler Di-4-ANEPPS

The confocal laser excitation beams are required to direct separately onto the cell membrane region and the bulk cytosol simultaneously. However, a rat cardiac myocyte has a very complicated structure. To make the measurements meaningful, we have to accurately locate the excitation laser beam onto the right positions. It is very important to label the surface membrane and the transverse tubules (t-tubules) structure.

It has been suggested that the t-tubules play a central role in cell activation because many of the proteins involved in excitation-contraction coupling appear to be concentrated at the t-tubules. The location of sarcolemmal Ca^{2+} handling proteins is important because of their role in excitation-contraction coupling and because the Ca^{2+} release channels (ryanodine receptors [RyRs]) of the arcoplasmic reticulum (SR) are concentrated close to the t-tubule.

The t-tubules of cardiac myocytes have a mean diameter of ~200 to 300 nm [29], although within a single rat ventricular myocyte, the diameter of individual tubules can vary from 20 to 450 nm, but more than half the t-tubules have diameters between 180 and 280 nm [30]. Early studies of cardiac muscle showed that they occur at intervals of ~2 mircon along the longitudinal axis of the ventricular myocyte. The structure of the t-tubules is shown in Figure 2.4.

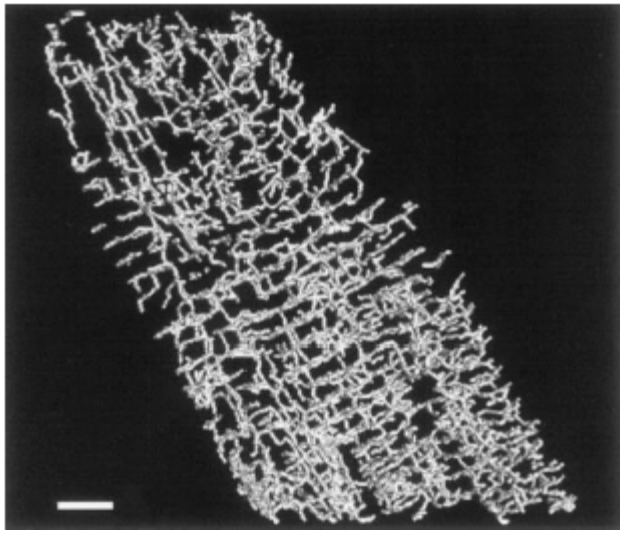

Figure 2.4 Three-dimensional structure of the t-tubular system in a living rat ventricular myocyte, [31]

To ensure that one of the modulated laser excitation beams locates at or near the cell membrane, while the other is in the bulk cytosol, we "doubly" label the myocyte with a fluorescent membrane potential indicator, Di-4-ANEPPS. It distributes to the charged plasma membrane (surface membranes and transverse tubules) with little-to-no signal in the cytosol. The sample cells are incubated with the lipophilic fluroscent indicator Di-4-ANEPPS (5um; Invitrogen). Di-4-ANEPPS exhibits fairly uniform 10% per 100mv changes in fluorescence intensity in model membrane systems. The ANEP dyes are essentially nonfluorescent in aqueous solutions and exhibit spectral properties that are strongly dependent on their environment. The fluorescence excitation/emission maxima of di-4-ANEPPS bound to neuronal membranes are ~475/617nm. Di-4-ANEPPS respond to an increase in membrane potential (hyperpolarization) with a decrease in fluorescence excited at approximately 440nm and an increase in flurescence excited at 530nm. These spectral shifts permit

the correlation of the change in fluorescence signal with membrane potential. The detailed emission spectrum of Di-8 ANEPPS are shown in Figure 2.5.

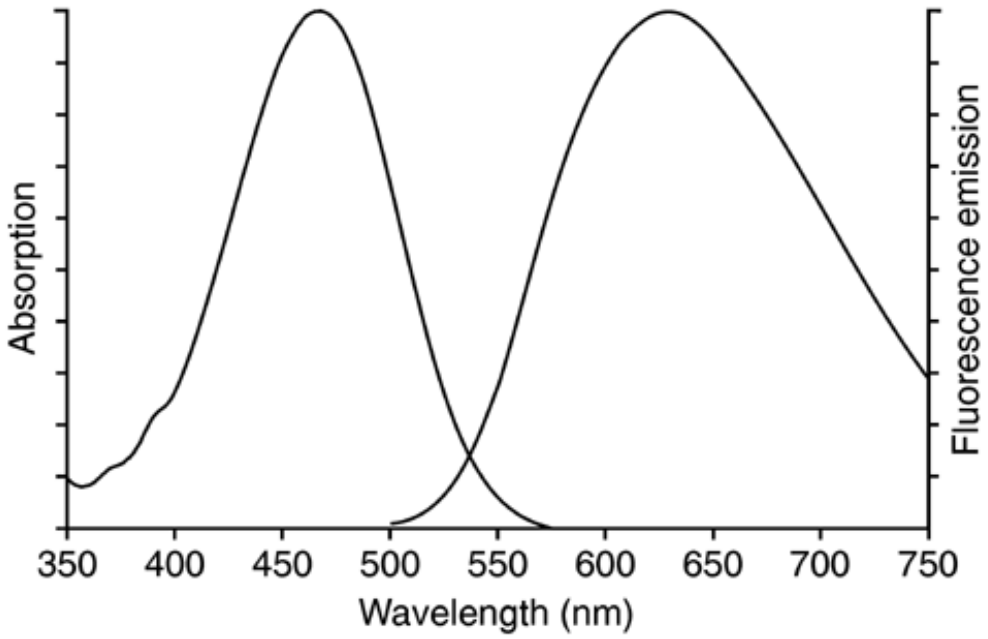

Figure 2.5 Absorption and fluorescence emission spectra of Di-8-ANEPPS bound to phospholipids bilayer membranes.

2.3 Experimental design

To track simultaneous changes in Ca^{2+} ions at submembraneous regions and Ca^{2+} ions in the bulk cytosol region of a living cardiac myocyte during an action potential, in this thesis, we applied our FDM fluorescence confocal microscope to simultaneously measure Ca^{2+} ions at the submembraneous region and Ca^{2+} ions in the bulk cytosol region of the same living cardiac myocyte.

Living rat cardiac myocytes are used as samples. They generally have a dimension around 100 μm in length and 20 μm in width. The rat cardiac myocytes are freshly isolated at the Hershey Medical Center and delivered to the University Park campus by a shuttle bus. The delivery time is about 2 hours. The myocytes are incubated at around 37^0C during the delivery to keep their viability. The healthy myocytes are quiescent in their original shapes while dying myocytes contract together. The myocytes with good viability could give a large contraction (shortening by 10 to 20%) when stimulated electrically. The resting rat myocytes are loaded with the fluorescence Ca^{2+} ion indicator Fluo-4 AM ester dye (1.8 μM, 30min) for 20 minutes at room temperature after they arrive, followed by 30min for deesterificaiton [32]. The samples bathed in the control solutions are then transferred to a Dvorak-Stotle culture chamber and mounted onto the FDM two-channel confocal microscope built on top of a vibration-resistant optical table.

Since Fluo-4 is a single wavelength excitation fluorescent probe, its fluorescent intensity is proportional to the excitation light intensity, the volume of the focused optical light point, fluorescent probe concentration, in addition to free Ca^{2+} ion concentration. To ensure the fluorescent intensity of Fluo-4 reflects the free Ca^{2+} ion concentration in the region interrogated and

to make the measured signals from different channels comparable to the other, the intensities of the two excitation beams are measured at two focusing spots and further balanced by adjusting the intensity of one of the beams until two beams have equal intensity. Furthermore, all the optical light paths are fixed to ensure the volumes of the focus points are constant and equal to the other.

It should also be noted that binding of Ca^{2+}ions to buffers, including the fluorescence indicator, is limited by the kinetic on- and off-rate constants of the buffer. Therefore, for very fast changes in free Ca^{2+} ion concentration, buffers may not be in equilibrium with free Ca^{2+} ions. This is especially important to consider and to compensate for when using fluorescence indicators to determine intracellular Ca^{2+} ion concentrations. It should also be noted that fluorescence indicators themselves affect the free Ca^{2+} ion concentration due to their own binding affinity. Also, the distribution of the dye inside the cell is often not known in detail. Binding to the surface or clustering inside membrane bound organelles can significantly alter the fluorescence signal obtained in various experimental situations.

In our design, two methods are combined to locate the focused laser beams to the right positions in the samples. First by labeling the cell surface membrane and t-tubular structures, we can direct one laser beam onto the submembranous region where the Di-4 signal is stronger. The other laser beam is directed to a cytosol region with little or no Di-4 signal. In our experiment, the cells are resuspended in control solution and imaged using the confocal microscope to detect the Di-4 fluorescent emission. Fluorescent emission of Di-4 is also excited at 488 nm by the argon-ion laser. Emission components longer than 550 nm are detected to label the membrane and t-tubule in the cell.

The second method involves the back scattering pattern of the laser beam. Light scattering occurs as a consequence of fluctuations in the optical properties of a material medium. A completely homogeneous material can scatter light only in the forward direction, therefore, no back scattered light can be observed. When a laser beam is incident on the myocyte, scattering happens because of the inhomogeneous structure of the cell. The back scattering pattern of an incident laser beam depends on the position of the focused beam. The pattern will be very complicated if the laser beam is incident onto the organelles since the organelles generally have very inhomogeneous structures. Comparatively, the back scattering pattern of the cytosol will be less in intensity and simpler in pattern since the cytoplasm is more homogenous in a cell body. A colored CCD camera in the experimental setup is used to monitor the samples and record the back scattering patterns of the stimulation laser beams. In an ideal case, the focused laser beam should be positioned in a myocyte with minimum scattering observed. In our experiment, if we finely adjust the laser beam position into a point where minimum blue laser light can be observed from the CCD camera, then we expect the focused beams to have a better chance in the cytosol. In Figure 2.6, the two different back scattering patterns of incident laser beams are recorded by a colored CCD. In the upper picture, we can see a strong and complex scattering light at the left focus and a week back scattering pattern at the right focus. In the lower picture, the fluorescence light of Fluo-4 can be seen at the left focus, which suggests the focused incident beam points into the cytosol.

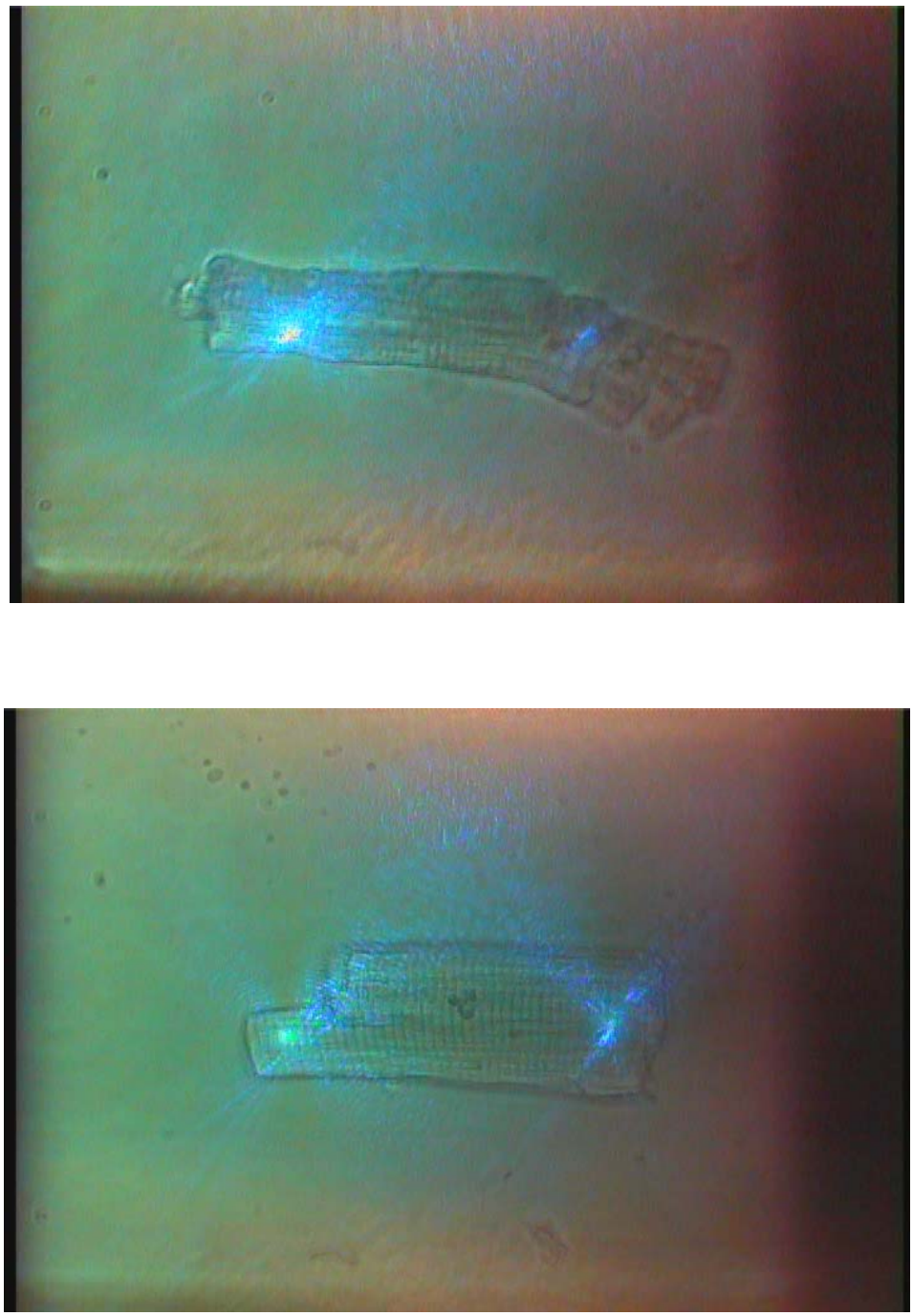

Figure 2.6 Back-scattering pattern of incident laser beam (488nm, blue) by isolated cardiac myocyte.

In our model of the FDM confocal microscope, we assume that the object function is time-independent which implies that the transition lifetime of the sample is much longer than the period of the pulse train. However, a good living cell could give a large contraction when stimulated electrically so that it introduces motion artifacts into the detected signal, which have to be eliminated. Butanedione monoxime (BDM) has been widely used to inhibit contraction during optical recordings of cardiac calcium ion dynamics in rabbit and canine cardiac myocytes. We also used it as the excitation-contraction uncoupler in the early stage of our experiments. However, we found the concomitant abolition of Calcium ion transients of cardiac cells as long as the BDM was doped into the control solution, which agrees with an earlier report [33] that BDM markedly abbreviates cardiac action potentials of rat cardiac myocytes. Therefore, we switch to CytoD as the excitation-contraction uncoupler and our experimental results proved CytoD is not only an effective excitation-contraction uncoupler, but also has no significant influence on other action potential parameters. In our experiment, the CytoD is applied to the cardiomyocyte by adding a 2-5ul drop of CytoD solution into the culture chamber using a pipette.

The procedure of the experiment is as follows: 1) balance the two incident laser intensities using the optical power meter; 2) balance the signal detection efficiency of two channels by finely tuning the optical alignment of the two fiber couplers and using a calcium calibration buffer kit as the sample; 3) load the rat myocyte samples with Fluo-4 and Di-4 following the loading instruction of the product manuals; 4) load isolated cardiac myocytes in the culture chamber and mount it on the stage of the confocal microscope; 5) find the proper cell which means the myocyte is in good shape and rests quiescently in the control solution, upon electrical stimulation, the sample should give a significant contraction; 6) load the CytoD into the culture chamber and assure the myocyte keeps

resting upon electrical stimulation; 7) move the detected sample by tuning the translation stage and the rotation stage so that the incident laser beams point to proper positions in the cell; 8) record the Di-4 signal by inserting a 550nm long pass filter in the fluorescent signal path; 9) record the Fluo-4 signal by replacing the long pass filter by a 520-540nm bandpass filter while no electrical stimulation is applied to the cell; 10) record the Fluo-4 signal while the cell is stimulated by a 1Hz 2-4ms suprathreshold rectangular voltage pulses train via a pair of extracellular platinum electrodes.

2.4 System calibration

The volume of the focus illuminated by the excitation laser beam is estimated similar to the case of a conventional single point fluorescent confocal microscope. With the lateral being Δr and the depth being Δz, the resolutions of this multiplexed microscope can be estimated by

$$\Delta r = 0.61\frac{\lambda}{NA}$$
$$\Delta z = 0.5\frac{\lambda}{NA^2} \qquad (2.1)$$

where λ is the fluorescent wavelength and NA is the numerical aperture of the objective lens. In our experiments, λ is 0.5um and NA is1.4. The lateral and axial resolutions are around 0.2um and 0.1um, respectively, which is good enough for studying the Calcium ions of rat cardiac myocytes.

The section capability of the confocal microscope depends on the size of the pinhole used. In our case, it is a single mode fiber with a mode field diameter (MFD) of 3.5um at a wavelength of 515nm

and a focus lens with N.A. of 0.15. To measure the reflectance axial response curves of the two channels, a stepper motor-driven plane mirror is scanned axially through focus in the microscope with a step size of 0.1 micron. The experimental results are shown in Figure 2.7. Both channels have a similar optical sectioning ability with the half-widths about 3 um in the axial direction of the objective lens, and two focused beam waists are at the same transversal plane, which indicates that the curve of field aberration has been well corrected by the objective lens. The detected sectioning thickness is larger than the theoretically estimated value. The possible reasons are: First, the Nikon objective lens is designed with a tube length of 160mm. However, it is used as an infinite corrected objective which leads to an imperfect imaging of the lens. Second, single mode fibers serve as pinholes. The cross section area of the single mode fiber is larger than the optimized value. Third, the output from the Argon ion laser is not a perfect Gaussian beam due to the aging of the laser system. To correct the distorted wavefront, we can insert a spatial filter to clean up the output of the Argon ion laser if a better imaging resolution is requested.

To make the data collected by two different channels comparable, it is important to balance the signal detection efficiencies. The detection efficiencies of the two-channel confocal microscope are calibrated as follows: three different buffers are used as the calibration samples; the Calcium ion concentrations of the three buffers are 39umol, 1.35umol and 0umol. Samples with different Calcium ion concentration are prepared by employing a reciprocal dilution method to Calcium ion calibration buffer kits (Invitrogen) which contains 50mL of 10mM K2EGTA and 50ML of 10mM CaEGTA. Both solutions contain 100mM KCL and 30mM MOPS, pH 7.2 and are prepared in deionized water (resistance 18Mohm). These stock solutions can be blended to make buffers having free Calcium ion ranging from 0um to 39umol.

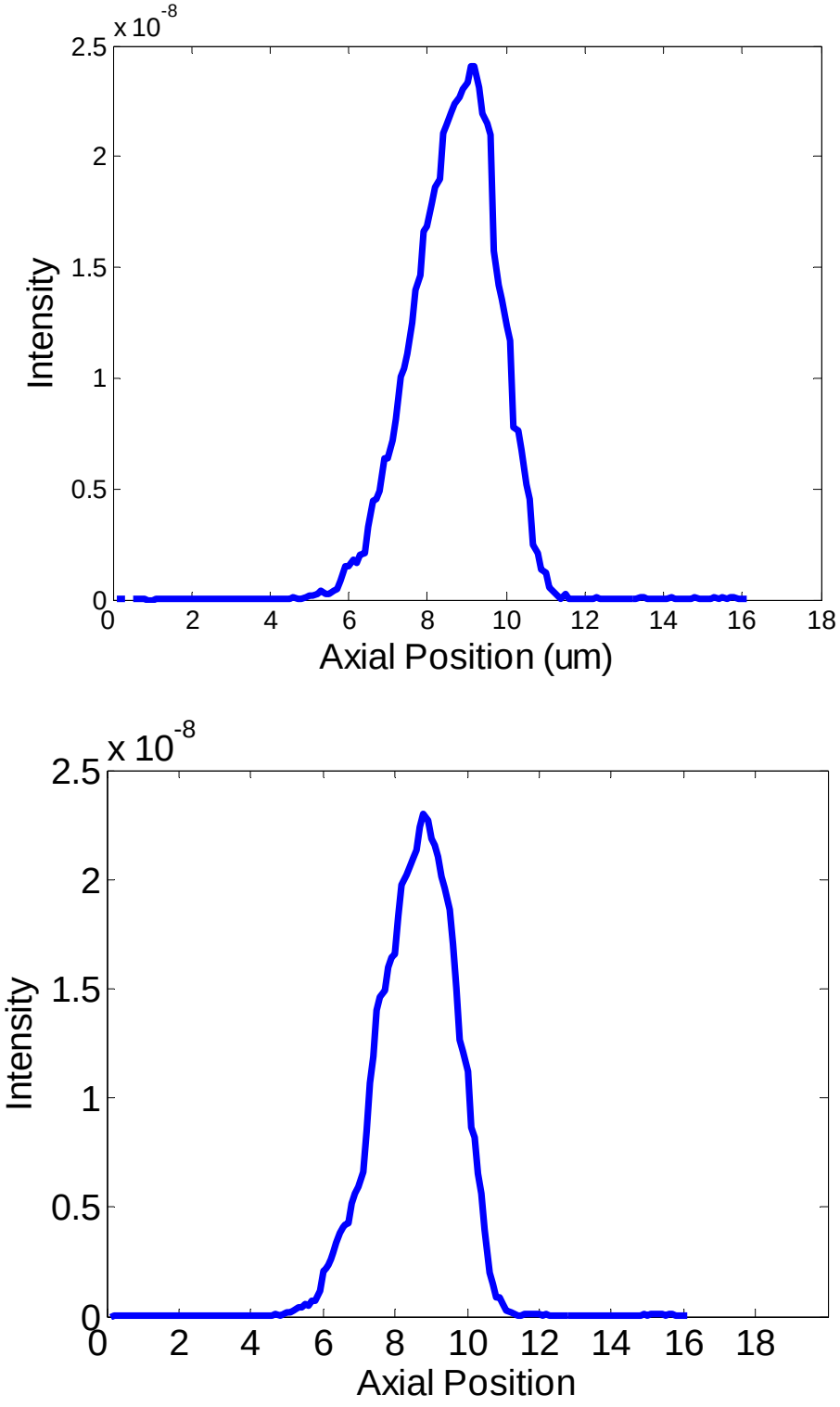

Figure 2.7: Measured Z axial profile of two different channels of the confocal microscope.

The buffer loaded with Fluo-4 (10mM) is sandwiched by two 0.17mm cover slips with a 0.17mm thick Teflon spacer in between. Two incident laser beams are focused into the buffer volume. The intensities of the laser are adjusted by tuning the injection current at the operator panel of laser. The injection current is set to be between 29A and 35A which corresponds to an output intensity from 10mW to 20mW. A diffraction limited excitation by no more than a few mW of appropriate visible ion laser radiation generally saturates typical fluorophores. The output intensity is much higher than what is necessary. However, it is preferable to run lasers at high output levels because the output intensity of the Argon-ion laser is more stable than that at low output levels. We usually keep the injection current around 30A with the auto-track function on to prevent the laser output from fluctuation and deviation. A continuous adjustable metallic reflection optical attenuator is put into the optical path of the incident laser to lower the optical intensity and prevent the saturation from happening. The back high reflective mirror of the laser cavity needs to be finely optimized every two weeks to keep the laser operating at its best condition. Another continuous adjustable reflective optical attenuator is inserted into the optical path of one of the channels to balance the incident laser intensities of two channels.

The experimental calibration results are shown in Figure 2.8 and Figure 2.9, and each figure represents one channel of the microscope. The fluorescence signals are collected for 4 seconds and they fluctuate with time. Despite a certain level of the noise, it is shown that signals from samples with different concentrations are well separated which means a reasonable SNR can be achieved. In Figure 2.8, the red curve refers to the highest calcium ion concentration (39uMol) and the highest incident laser power (286uW). The value of the red curve decreases with time which is not observed

at the other two curves. Photobleaching contributes to the decrease and suggests that a lower incident laser power should be used in our experiment. The detected signal of the 0mol concentration buffer is from the dark current of the PMT and leakage of the incident laser by the filter (Omega filter OD3).

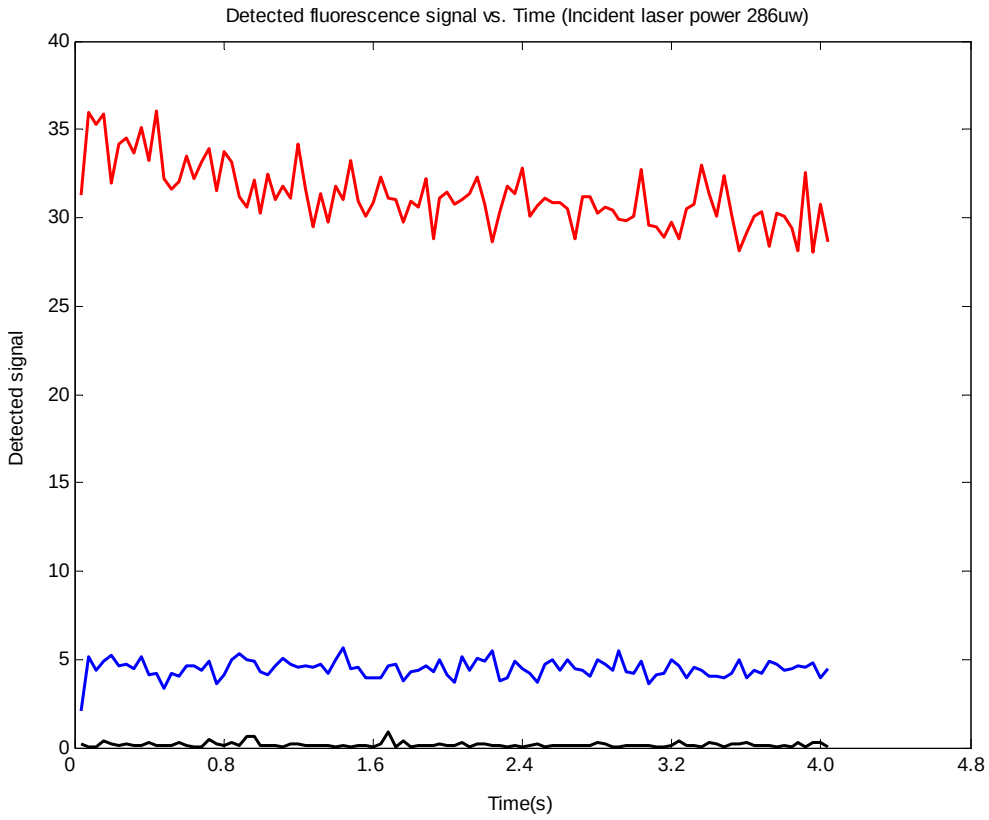

Figure 2.8: Fixed incident laser intensity 286uw, detected fluorescence signal at different Calcium ion concentration of channel one.

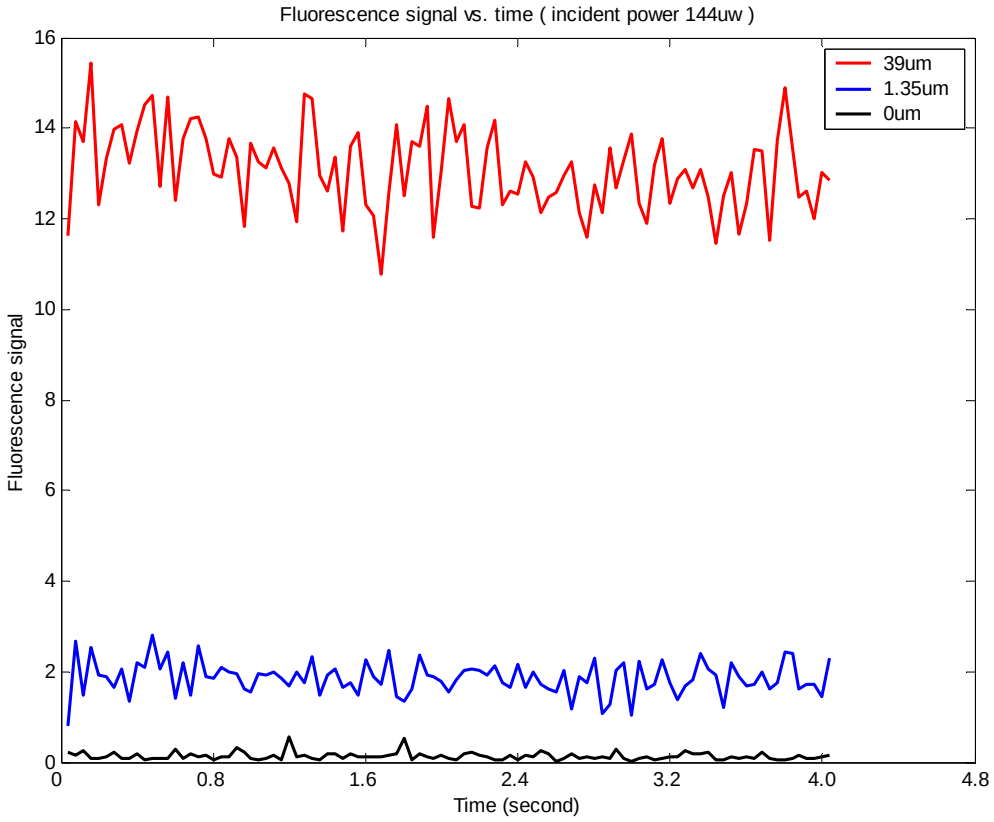

Figure 2.9: Fixed incident laser intensity 144uw, Fluorescence signal at different Calcium ion concentration for channel 2.

The balanced calibration signal is shown in Figure 2.10. The calibration sample is again a free Calcium ion buffer loaded with fluorescence dye sandwiched between two glass cover slips. The intensities of the incident laser beams are equal. The Calcium ion concentration and dye molecules are uniform in the buffer. Therefore, the fluorescence signals from two different channels should be

the same if the system is calibrated perfectly. From the experimental results, the detected fluorescence signals of channel 1 and 2 are very close to each other, and the difference can be further corrected by adding a weight while doing the data processing.

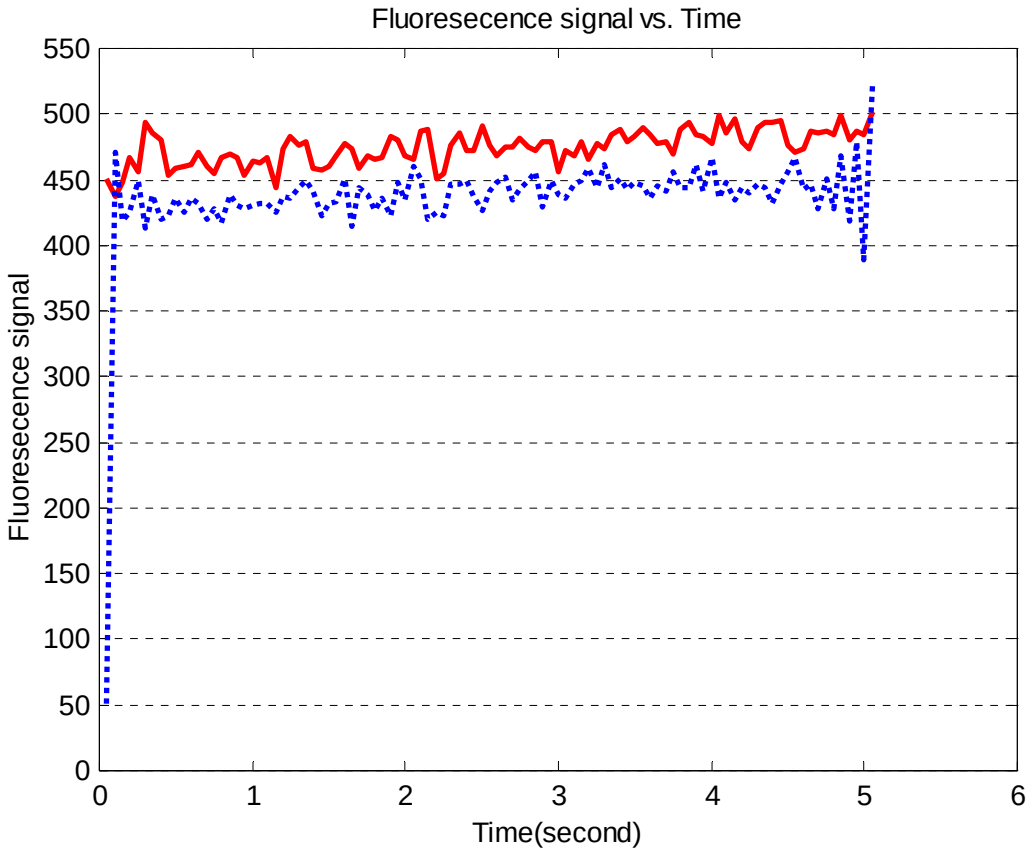

Figure 2.10 Calibration results of two channels using high concentration calcium calibration buffer, red and blue curves refers to two different channels.

2.5 Experimental results

In the experiment, we first recorded the Fluo-4 signal when the cell is at rest without applying the stimulating electric field. The detected signals after processing are shown in Figure 2.11. The blue curve shows the signal strength at submembranous domain and the red one in bulk cytosol of the cell. It indicates that the Calcium ion concentration is about even at different locations in the myocyte cytosol. Then, we change the filter to a 550nm longpass to detect the Di-4 fluorescence signal and record the back scattering pattern of the incident laser beam in the sample. The detected Di-4 signal is shown in Figure 2.12. To minimize the motion artifact of the myocyte, CytoD is used to immobilize the myocyte while preserving Ca^{2+} transients. The myocyte was stimulated by a short (2ms) rectangular shape electrical field pulse train at 1 Hz and the Fluo-4 signals were continuously sampled and detected for 5-10 seconds. The detected data were processed according to the procedure as described in the previous section. Figure 2.13 shows the measured temporal variation of the Ca^{2+} around the membrane region and Ca^{2+} in the bulk cytosol of the same myocyte concurrently. From our experimental results, we can draw the following conclusions: first, the calcium ion concentration indeed beats during the cell contraction. Second, the calcium concentration at the submembranous region is higher than that measured at the bulk cytosol region.

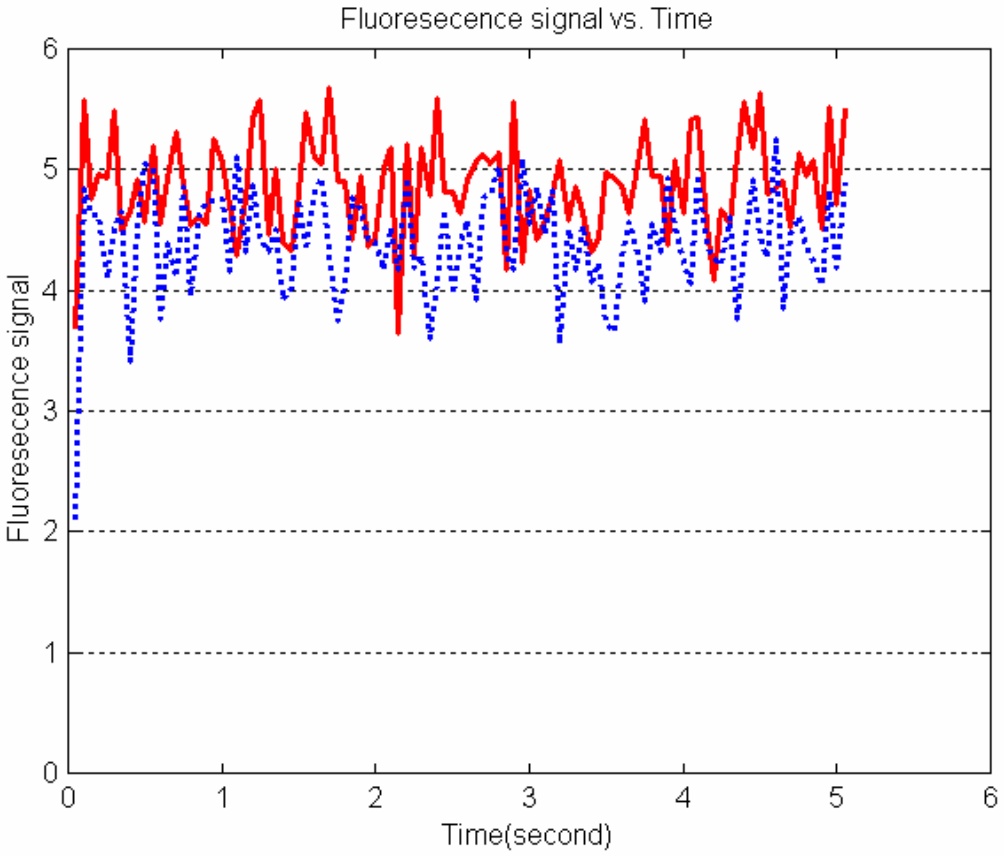

Figure 2.11 Detected Fluo-4 signals at two locations of cytosol when cell rests.

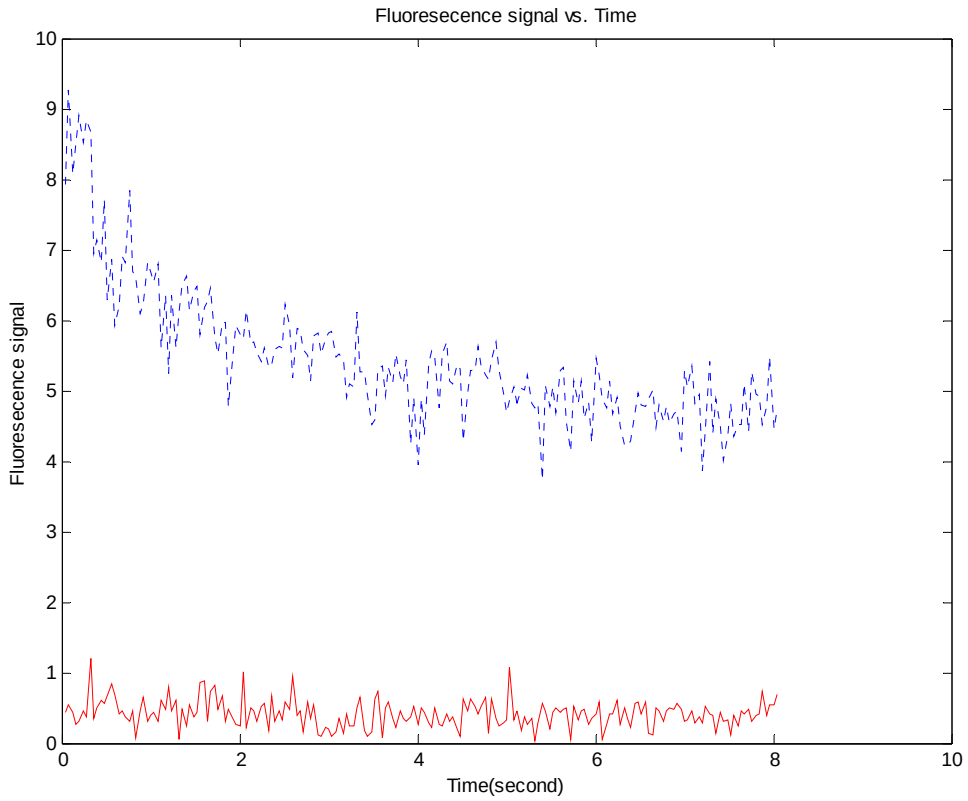

Figure 2.12 Detected Di-4 fluorescence signals (blue curve close to membrane and red curve in mid of cytosol)

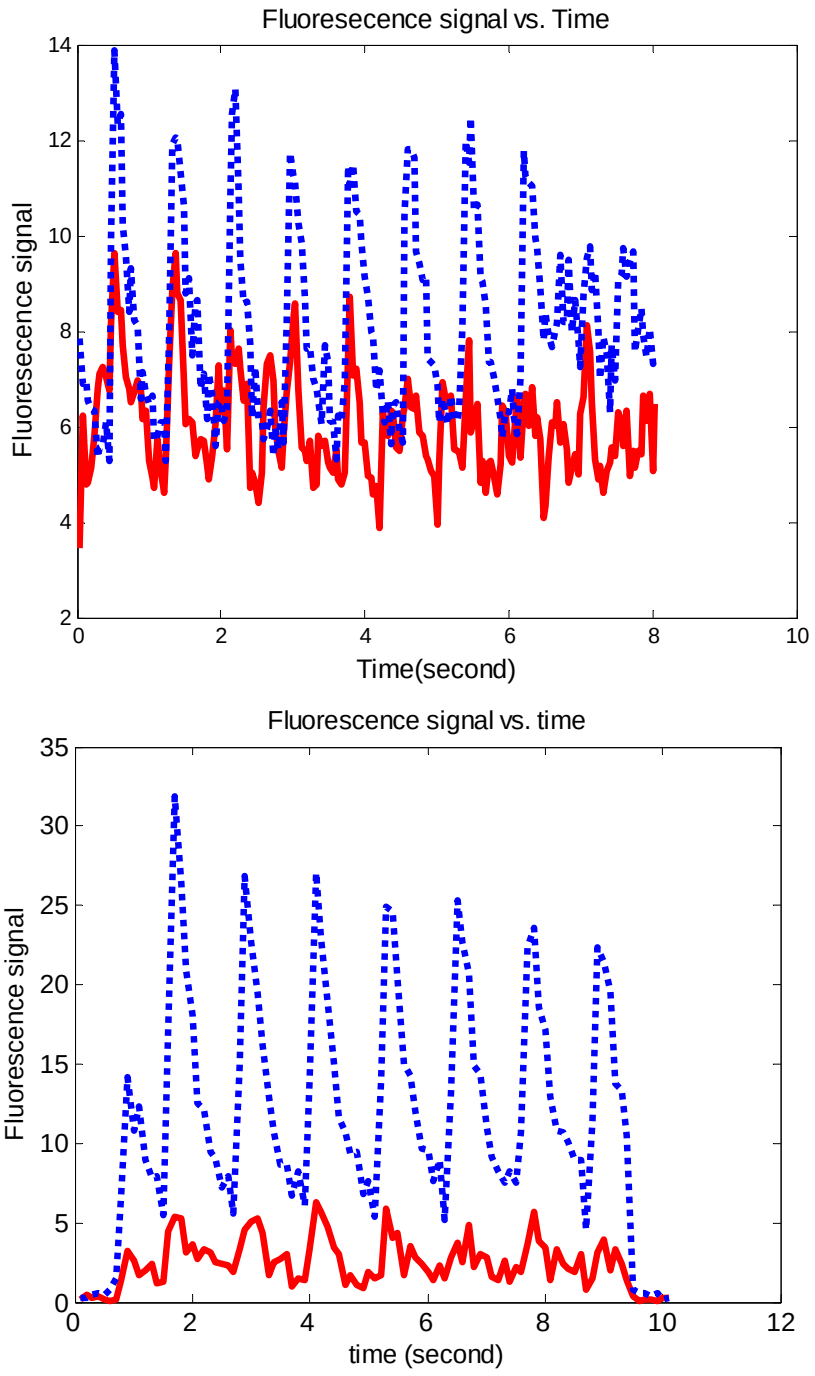

Figure 2.13: Detected intracellular Ca^{2+} concentration beating curves in two different cells. Red curve: fluorescence emission from the bulk region, Blue curve: fluorescence emission from the membrane region.

Chapter 3 DISCUSSIONS OF EXPERIMENTAL DESIGN AND NOISE ANALYSIS

3.1 Noise analysis

Because of the existence of noise, data sets produced by scientific measurements can not have an arbitrarily high signal-to-noise ratio and this may severely limit the extent to which the information can be usefully extracted.

3.1.1 Intrinsic Noise

The accuracy of any specific measurement of fundamental quantum interactions is limited by Poison statistics. Because photons are quantum mechanical events, the number *n* actually detected in any one of a number of measurements, made under identical conditions, is related to the mean of all these measurements (n_0) only by the Poisson distribution. As long as n_0 is not too small, this noise term is proportional to $n^{1/2}$, where n is the smallest number of quanta present at any single stage of the information pathway used for the particular measurement [34, 35].This means that if the average result of these measurement is n_0, the chance that any specific measurement falls in the range of $n_0 \pm n^{1/2}$ is 63%. This relationship provides the practical basis for the standard relationship between the number of quanta represented by the brightest pixel in the image ($N_{\max}$) and the maximum number of statistically distinct signal levels or gray levels (G) that can be distinguished in the image (assuming that each gray level is one standard deviation from the next).

$$G = \left(N_{\max}\right)^{1/2} \qquad (3.1)$$

Theoretically the signal-to-noise ratio can usually be improved by exposing the specimen to more light and counting more photons. However, the success of this approach may be limited by lack of time or the damage that further exposure may do to the specimen. In other words, the statistical accuracy of the data may be improved but, as the object represented by this improved data is now a damaged object, the information about it that is conveyed to the observer may actually be less accurate.

Most Confocal Laser Scanning Microscopes (CLSM) use a linear, 8-bit analog-to-digital converter (ADC) that digitizes the analog signals, and store a number directly proportional to the intensity of the sensed signal with a precision of 1 part in 256 in the computer memory. However, if the signal stored as the number 255 actually represents the detection of only 9 photons, then there will only be $(9)^{1/2} = 3$ statistically distinct signal levels recorded in the data, not 256. It is common for the signal intensity of the brightest pixel in a single-scan image from a CLSM to represent only 10 detected photons assuming the 1.6-psec pixel dwell-time that is characteristic of a 512 x 768 pixel raster scanned in 1 with a 62% duty cycle [36, 37]. This problem has been greatly improved by our non-scanning multi-channel design. With an about 50% duty cycle caused by intensity modulation, there are many more photons can be detected using our design compared with the traditional laser scanning design, and the intrinsic noise is greatly decreased.

3.1.2 The cross-talk noise:

The worst case scenario (i.e., the highest cross-talk case) happens when the two laser spots are focused in the same location. In this case, the signal separation can only be realized by different carrier frequencies. Under the ideal case in which no noise exists, as long as the lowest carrier frequency and the separation between adjacent frequencies are twice of the signal frequency (i.e., Nyquist sampling theorem), there will be no cross-talk among laser channels. However, due to the existence of the noise (e.g., the noise from the detector), there will be cross-talk among different laser channels. Without losing generality, assume that the noise is Gaussian. In this case, the bandwidth of the noise spectrum can be estimated by observing the detected signal over a finite time interval [38]. Then, we select the frequency and the frequency difference between adjacent channels at least twice this estimated spectral bandwidth, which ensures a low cross-talk noise.

3.1.3 Noise of PMT

The chief source of PMT noise is the dark current. This includes any leakage currents between the electrodes, the small pulses caused by the amplification of thermal photoelectrons emitted by the lower dynodes and sometimes DC offsets in the head amplifier, as well as dark counts produced by thermally excited leaving the photocathode. The dark current of a PMT is usually low, but it is a strong function of the temperature and, in the heated confines of some commercial instruments, it may not always be small compared to the signal level of weakly fluorescent samples. In our experimental setup, an un-cooled head-on PMT is used to detect the fluorescent signal at room temperature (about 28^0C -30^0C). The detected dark current noise is already shown in calibration results and can not be ignored.

Ideally, all photons should make an equivalent contribution to the output and as a result the output current would be exactly proportional to the number of photons. However, in practice, the digitizing circuitry found on many commercial instruments is poorly suited to quantitative applications in that identical pulses from a pulse generator are digitized as markedly different depending on their time of arrival during the digitizing interval. In our experiment, a high performance cooled PMT will be very helpful to improve the signal-to-noise ratio of our results.

3.2 Finite width of signal spectra

The frequency spectra of detected signal peaks have finite widths, which are mainly due to the following two reasons: (1) The signals themselves have certain bandwidths-for example, for the rat cardiac cell contractions, the highest frequency components during the contraction processes are in the order of tens of Hz; (2) The existence of the noise can also contribute to the broadening of the bandwidths-the major noise source is the detector noise due to the weak fluorescence signal.

3.3 FDM

A rational frequency division multiplexing design is critical for the FDM confocal microscope to improve the temporal resolution, minimize the interference among different channels, and maximize the possible channel number of the design. The working principle of our design is analogous to television cable service. The values of carrier frequencies are the key parameters. The higher the modulation frequencies, more number of channels can be designed and more bandwidth can be assigned to each channel and therefore the higher the temporal resolution can be achieved in the imaging system. A wider guard band can also be chosen to decrease the crosstalk noise among different channels.

The channel number N can be expressed:

$$N = \frac{2 * f * r}{1 + 2 * r * g_0} \qquad (3.1)$$

where r is the required temporal resolution, f is the maximum modulation frequency and g_0 is the guard bandwidth.

The frequency bandwidth of PMT is 200 kHz in our case limited by the bandwidth of the current-to-voltage conversion amplifier of the PMT. The intensity modulation of the stimulation laser beams is realized by an optical chopper. The maximum modulation frequency of the chopper is 4 kHz, therefore very limited channels can be designed with our equipment.

With the current technology, the ultrafast laser can produce pulses as short as 10^{-15} second with repetition rate of 10^9 Hz and higher [39]. If it applies to our FDM design, it suggests a great potential to combine high spatial resolution with high temporal resolution. Whereas for nanosecond and picosecond pulses optical systems behave quite similar with monochromatic light, the use of femtosecond light pulses leads to new effects [40-45]. The difference in focusing femtosecond light pulses and monochromatic light is due to the chromatic aberration of lenses which can be expressed as [42]

$$\frac{\tau}{T} = \frac{a^2 k_0}{2 f_0 (n_0 - 1) T} \left| \frac{dn}{dw} \right|_{w=w_0} \qquad (3.2)$$

Where a is the aperture radius of the lens, f_0 is the focal length, n_0 is the refractive index of the lens material, k_0 is the wave vector, and T is the duration of the incident light pulse. Index 0 is taken at the center frequency ω_0 of the pulse. Then for single-photon fluorescence confocal microscope, the intensity point spread function is different. For a given frequency component w, the illumination field from a point source in the object space is $A(\Delta w) h_1(r_1, \Delta w)$, where h_1 is the 3-D amplitude point spread function for the objective lens, and A(w) is the spectral amplitude of the incident pulse which can be modeled as a Gaussian function at transform limited case.

3.4 Fluorescence emission

The discussion of FDM confocal microscope design so far assumes that the fluorescence signal strictly inherits the modulated frequency of the illumination laser signal. It means that the transition time of fluorescence emission is much shorter than the temporal coherence of the illumination, which, however, is not true when the modulation frequency is high.

The process of fluorescence emission can be explained as follows: Upon absorption of a photon whose energy matches the difference between the ground state and some excitation state, a fluorophore molecule undergoes an upward transition to the excited state which typically is a vibrational state within the particular singlet band. The excited molecule then relaxes very quickly ($\approx 10^{-12}$ second) to the lowest vibrational level by a radiationless process. This energy loss leads to

the Stokes shift between excitation and emission spectra of fluorophores. The fluorescence competes with other decay processes to give up energy and return back to the lower state. Since de-excitation from the lower state is relatively slow, usually not much less than 100ns, molecules may become trapped in this state, thus reducing the effective concentration of fluorophore. We can conclude from the above discussion that it takes time for the fluorophore molecule to emit fluorescence. It introduces a demodulation factor ξ caused by lifetime τ (total of lifetimes of all involved energy states) of the fluorophores which can be expressed as [46]

$$\zeta = 1 \Big/ \sqrt{\left(1 + f^2 \tau^2\right)} \qquad (3.3)$$

where f is the modulation frequency.

In our experiment, we compared the detected laser signal and the fluorescence signal in both the time domain and the frequency domain. The laser signal is detected by using a high reflectance plane mirror whereas the fluorescence signal is detected by using a thin film of the fluorescence buffer. It is not difficult to find that the fluorescence emission bears the same modulated frequency of the stimulating laser signal from Figure 3.1 (a). Furthermore, all the high order harmonic frequency peaks of the laser signal have been attenuated in the fluorescence signal spectrum. In the Figure 3.1 (b), we observe a little stronger fluctuation noise in the fluorescence signal than in the laser signal because the laser signal is stronger than the fluorescence signal. The strong fluctuation artifacts at the beginning and the end of the time domain curve are introduced by the FFT used in the data processing algorithm and should be treated as invalid data.

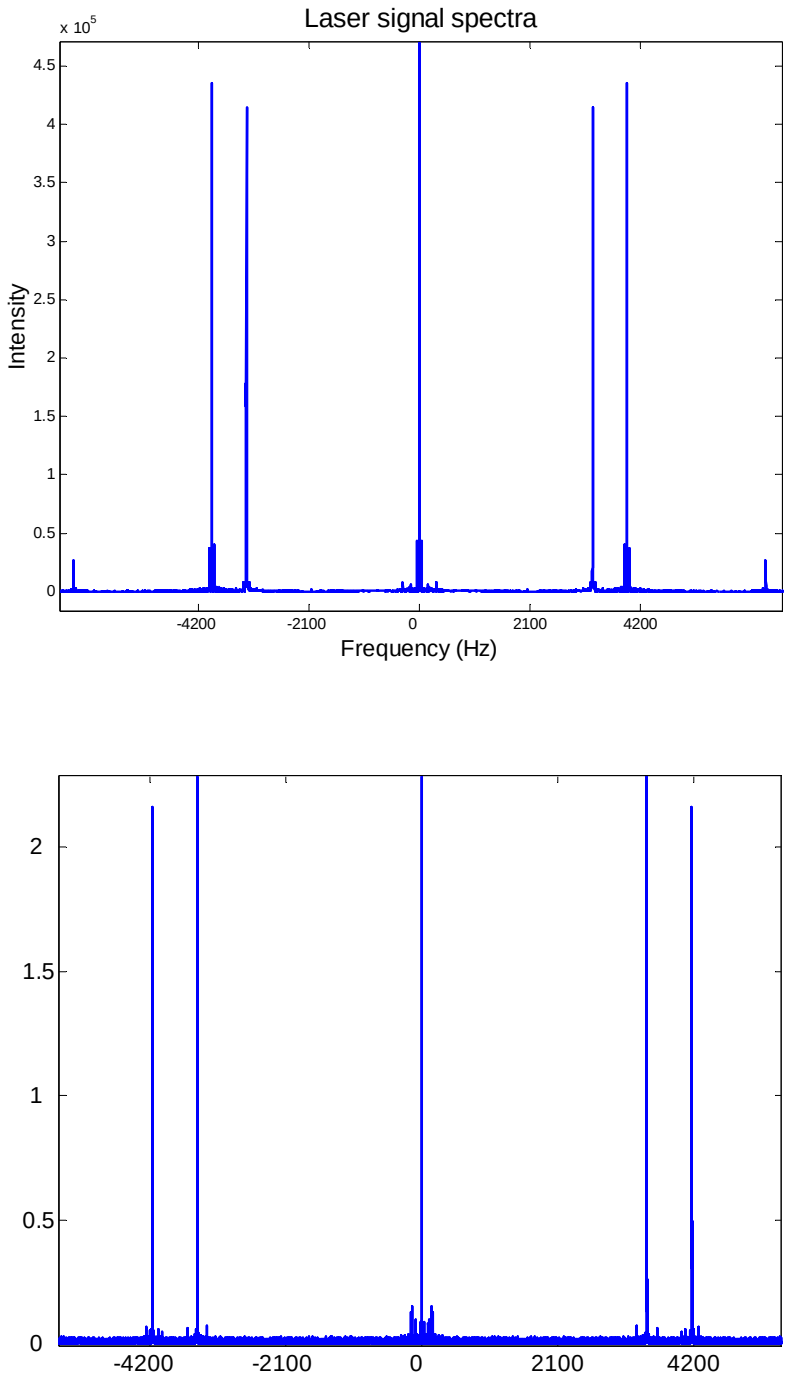

(a)

Figure 3.1 Comparison of the modulated laser signal and fluorescence signal in frequency domain.

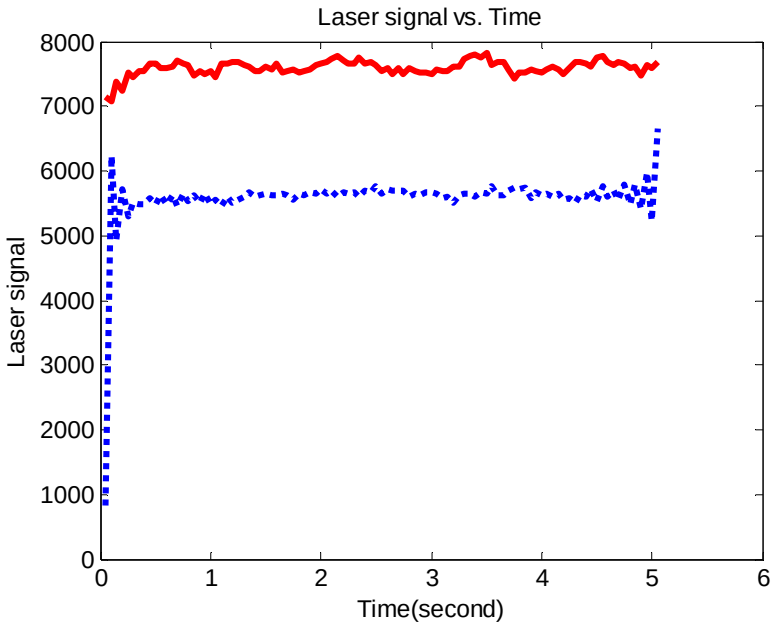

(a)

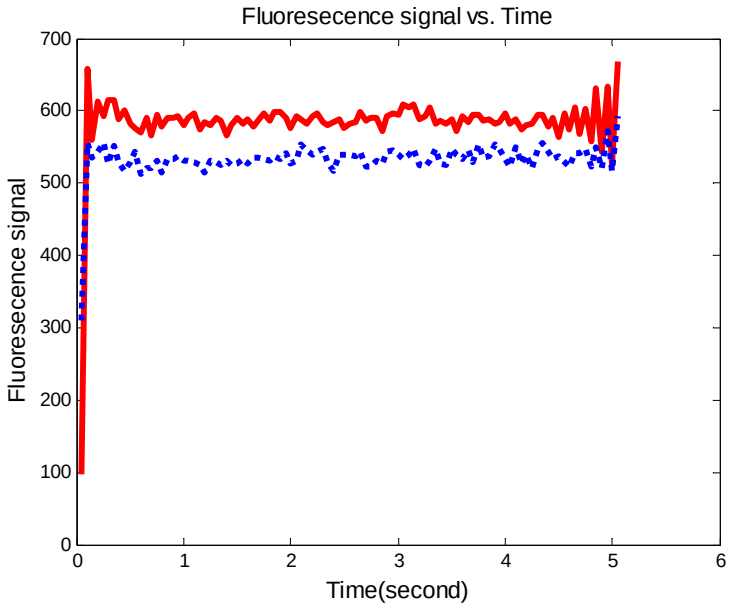

(b)

Figure 3.2 Comparison of the detected laser signal and fluorescence signal.

3.5 The maximum number of channels

The maximum number of channels is limited by two factors: (1) the response time of the fluorescent emission and the PMT photodetector and (2) the dynamic range of the photodetector. Since 1 ms temporal resolution is usually fast enough to analyze the dynamic behavior of living cells, the response-time-limited number of channels, M_r, can be estimated by the following formula,

$$M_r = \frac{Signal \cdot Temporal \cdot Bandwidth}{2 \times Temporal \cdot resolution} = \frac{1ms}{2 \times 10ns} = 5 \times 10^4 \qquad (3.4)$$

The dynamic-range-limited number of channels may be estimated in the following way: Assume that the useful dynamic range of the PMT photodetector is 30 dB (i.e., 1000 in the linear scale, that is a realistic number) and the required dynamic range from each frequency channel is 10 dB (i.e., 10 in the linear scale). In this case, the dynamic range limited number of channels, $M_{d,}$ is

$$M_d = \frac{total \cdot dynamic \cdot range \cdot of \cdot the \cdot photo\,\mathrm{det}\,ector}{dynamic \cdot range \cdot of \cdot each \cdot channel} = \frac{1000}{10} = 100 \qquad (3.5)$$

Comparing Equation (3.4) with Equation (3.5), we know that the maximum number of channels is mainly limited by the dynamic range of the photodetector.

The total number of channels of our design can be further increased by combining with the PMT array. Since a 32-channel PMT array is commercially available, by combining the frequency division multiplexing technique with the PMT array, the total number of channels can be as large as 100 x 32 = 3200, which is good enough for many confocal imaging applications.

3.6 Error caused by the spectra overlap of Fluo-4 and Di-4

To doubly label the samples with Fluo-4 and Di-4 ANEPPS simultaneously in the experiment, their respective fluorescence spectra must be sufficiently separated in wavelength in order to allow them to be separated by optical filters. The spectra of the two dyes are shown in Figure 3.3 [47]. We can see the peak separation is approximately 110nm. However, it can be seen that there is some overlap between the two spectra in which the shortest wavelengths of the Di-4 spectrum extend into the range of wavelengths for which the Fluo-4 spectrum is more intense. Similarly, the longest wavelengths of the Fluo-4 spectrum extend into the range in which the Di-4 fluorescence is more intense. Thus, Fluo-4 static error is defined as the error in a Fluo-4 resting spectrum caused by the addition of a Di-4 resting spectrum. To practically measure Fluo-4 fluorescence, a 520nm-540nm bandpass filter is used with the lower cutoff wavelength bounded by the laser line at 514nm and the upper cutoff wavelength bounded by the amount of tolerable overlap error with Di-4. Therefore, the Fluo-4 static error is calculated in terms of the areas under the curves from the wavelength of the laser up to the cutoff wavelength of interest. The following formula is used to compute the Fluo-4 static error

$$\%error=100\%*(summed\ area - Fluo\text{-}4\ area)/Fluo\text{-}4\ area \qquad (3.6)$$

where the summed area is the area under the curve resulting from the summation of the Fluo-4 and Di-4 curves. A similar analysis was performed to determine the Di-4 static and dynamic errors. The Di-4 static error, i.e., the error caused in the Di-4 resting spectrum by the addition of the Fluo-4 resting spectrum, was computed with the following formula:

$$\%error = 100\% * (summed\ area - Di\text{-}4\ area)/Di\text{-}4\ area \quad (3.7)$$

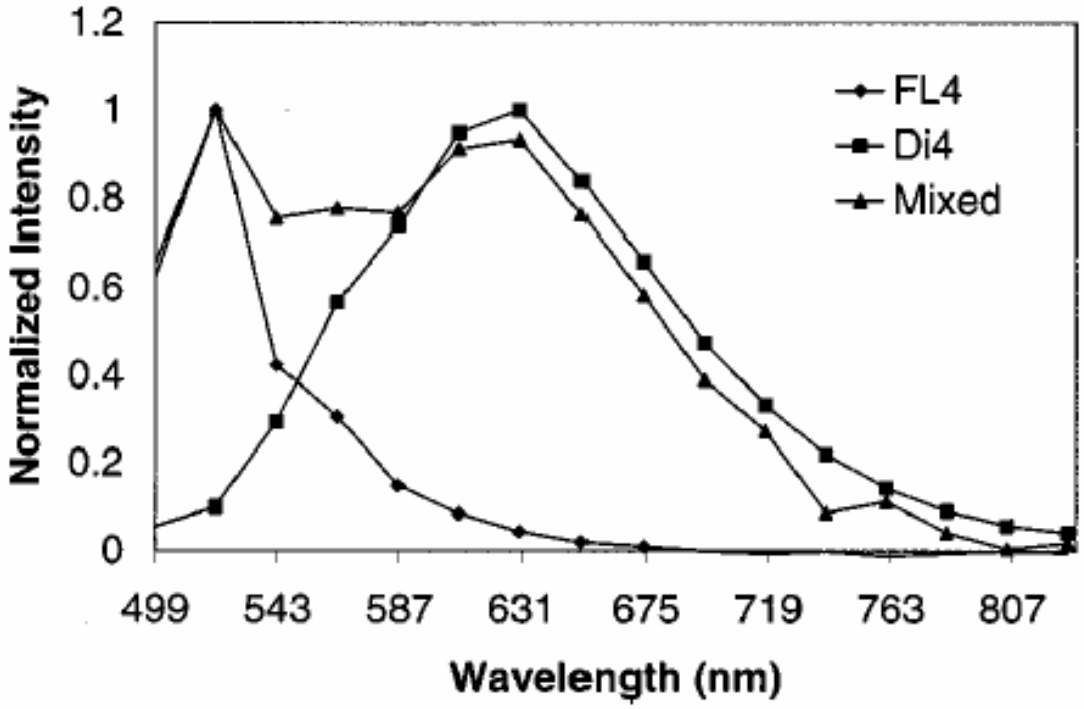

Figure 3.3 The individual Fluo-4 (FL4) and Di-4 ANEPPS (Di4) spectra and the spectrum measured with both dyes present. Measurements were obtained in rabbit hearts. The peaks of the individual spectra correspond to the local maxima of the mixed spectrum [44].

3.7 Photobleaching and photodamage

Two general aspects of the fluorescence imaging technique need to be considered. Photobleaching is the irreversible destruction of fluorophores in a defined region within a sample and then the subsequent observation of the redistribution of fluorescence by exchange of bleached and /or unbleached fluorescence molecules. Photodamage is the unwanted interaction of the excitation photons with the specimen. Both side effects should be avoided [45]. Generally both effects are dependent on the excitation energy and therefore one should reduce the illumination intensity to the minimal level at which a reasonable signal to noise ratio in the detected fluorescence can be obtained. In our experiment, the intensities of both excitation laser beams are set to be less than 0.5mW to avoid photobleaching and photodamage.

3.8 Conclusions and future work

A novel frequency division multiplexed multi-channel fluorescence confocal microscope is introduced. The fluorescence emissions from different locations are modulated at different frequencies and detected by a single high speed, highly sensitive photomultiplier tube. The spatial information of different fluorescence signals is recovered in the frequency domain by a Fourier transform of the detected signal. This approach is similar to the frequency division multiplexed cable television services, in which multiple channels at different carrier frequencies are sent in a single cable and the channel selection is realized by choosing the proper central frequency of a bandpass filter corresponding to the particular carrier frequency. The major advantages of this unique fluorescence confocal microscope are: (1) the high imaging speed, (2) and the high sensitivity. It could become an effective tool to study the transient dynamics in a cell. Although we only conducted a two-channel frequency division multiplexed confocal microscope experiment, more than two-channel multiplexing could be readily extended by slightly modifying the experimental set up.

In this part of the thesis, we first gave a brief introduction to the traditional confocal microscope design and discuss its limitations. Then we derived the point spread function and modulation transfer function of the proposed multi-channel confocal microscope. Single mode fibers served as pinholes in front of the PMT to collect the fluorescence signals. Their functions were also modeled and analyzed. The thorough calibration of the microscope, especially the balance of the two different channels was described in detail after that. The calcium ion concentration transient model at different locations in rat cardiac myocytes was then introduced. The proposed experimental design

was implemented to study the calcium ion transients in fresh isolated rat cardiac myocytes. The experimental results were given and analyzed. Finally, we discussed several important topics of the design, including error sources, maximum channel numbers of the design, modulation of the excitation light, and demodulation coefficiency of the fluorescence emissions.

Finally, we would like to point out that the experimental results of the application of this multiplexed confocal microscope to the study of transient dynamics of calcium ion concentration during the cardiac myocyte contraction is still preliminary, and mainly demonstrated the feasibility of this new type of confocal microscope. More thorough experimental study and quantitatively analysis of transient calcium ion concentration will be conducted and reported in future work. One of the most important aspects of any quantitative endeavor is the ability to confirm that the instrumentation used to perform the measurements is both accurate and precise. An understanding of the error associated with each component in the imaging system that influences the resulting image data is important. Historically quantitative disciplines demand that a quantitative assessment of uncertainty associated with measurements be presented along with results. Therefore, a thorough calibration of the instruments, particularly for the balance between two channels is very critical to collect accurate and meaningful data, and this should be done for each repeat of the experiment.

REFERENCES

1. Minsky M., ‘microscopy apparatus,’ *U.S. Patent 3 013467* (19 Dec. 1962).
2. Sheppard, c.j.r. and choudhury a. 1977, optica acta 24 1051
3. Lichtman, J. (1994). "Confocal microscopy." Scientific American: 40.
4. Pawley J., ‘Handbook of biological confocal microscopy’; *Plenum Press* 1989.
5. Cheung JY. Tillotson DL. Yelamarty RV. Scaduto RC. “Cytosolic free calcium concentration in individual cardiac myocytes in primary culture”; 1989 Jun;. Am J Physiol. 256(6 Pt 1):C1120-30.
6. Lothar A. Blatter, Jorg Huser and Eduardo Rios; “Sarcoplasmic reticulum Ca2+release flux underlying Ca2+ sparks in cardiac muscle”, April 1997 Proc. Natl. Acad. Sci. USA 4176-4181.
7. H.Cheng, W.J.Lederer, M.B.Cannell “Calcium Sparks:Elementary Events Undrelying Excitation-Contraction Coupling in Heart Muscle.”, Science. Vol.262. Oct. 1993, 740-744.
8. Tearney J., R. Webb and B. Bouma, ‘Spectrally encoded confocal microscopy’, Optics Letters, Vol. 23, No. 15 August 1998.
9. Fujita K., O., Nakanura, T. Kaneko, M. Oyamada, T. Takamatsu, S. Kawata, ‘Confocal multipoint multiphoton excitation microscope with microlens and pinhole arrays’, Optics Communications 2000, 7-12.
10. Yaqoob Z. and N. Riza, ‘Free-space wavelength-multiplexed optical scanner demonstration’, Applied Optics, Vol. 41, No. 26, Sep. 2002.
11. Lin C. and R. Webb, ‘Fiber-coupled multiplexed confocal microscope’, Optical Letters, Vol. 25, No. 13, July 2000.

12. Blom H., M. Johansson, M. Gosch, T. Sigmundssion, J. Holm, S. Hard, and R. Rigler, 'Parallel flow measurements in microstructures by use of a multifocal 4x1 diffractive optical fan-out element', Applied Optics, Vol.41, No.31 Nov. 2002.
13. Carlsson K., N. Aslund, K. Mossberg, J. Philip, 'Simultaneous confocal recording of multiple fluorescent labels with improved channel separation', J. Microsc. 1994 Dec; 176:287-299.
14. Shi, K., Peng Li, Stuart Yin, Zhiwen Liu, (2004). "Chromatic confocal microscopy using supercontinuum light." Optics express 12(10): 2096-2101.
15. GU, M., (1991). "EFFECTS OF A FINITE-SIZED DETECTOR ON THE OTF OF CONFOCAL FLUORESCENT MICROSCOPY." Optik 89(2): 65-69.
16. Kimura, S. and C. Munakata (1990). "Dependence of 3-D Optical Transfer-Functions on the Pinhole Radius in a Fluorescent Confocal Optical Microscope." Applied Optics 29(20): 3007-3011.
17. Sheppard, C. J. R., M. Gu, et al. (1992). "Signal-to-Noise Ratio in Confocal Microscope Systems." Journal of Microscopy-Oxford 168: 209-218.
18. SHEPPARD, C. (1994). "IMAGING PERFORMANCE OF CONFOCAL FLUORESCENCE MICROSCOPES WITH FINITE-SIZED SOURCE." Journal of modern optics 41(8): 1521-1530.
19. SHEPPARD, C. a. C. (1977). optica 24: 1051.
20. Wilson, T. and A. R. Carlini (1987). "Size of the Detector in Confocal Imaging-Systems." Optics Letters 12(4): 227-229.
21. Wilson, T. (1989). "Optical Sectioning in Confocal Fluorescent Microscopes." Journal of Microscopy-Oxford 154: 143-156.

22. GU, M., (1991). "IMAGE-FORMATION IN A FIBER OPTIC CONFOCAL SCANNING MICROSCOPE." Journal of the Optical Society of America. A, Optics and image science 8(11): 1755-1761.
23. Gu, M., JJ,James (1998). "Fibre-optic double-pass confocal microscopy." Optics and laser technology 30(2): 91-93.
24. Shigeharu Kimura and Tony Willson, "confocal scanning optical microscope using single-mode fiber for signal detection", Applied optics, 30(16): 2143-2150.
25. A.W.Snyder and J.D.Love, Optical waveguide Theory (Chapman and Hall, London, 1983);
26. Gu M., C. Sheppard and X. Gan, 'Image formation in a fiber-optical confocal scanning microscope', J.Opt.Soc.Am.A., Vol. 8, No.11 Nov. 1991.
27. Morton, G.A., Applied Optics, 1963, Vol. 2: 51-60.
28. Scriven D., P. Dan, and E. Moore, 'Distribution of proteins implicated in excitation-contraction coupling in rat ventricular myocytes', Biophys. J. 79:2682-2691. 2000.
29. Sommer JR, Jennings RB. *Ultrastructure of Cardiac Muscle*. New York, NY: Raven Press; 1992.
30. Soeller C, Cannell MB. Examination of the transverse tubular system in living cardiac rat myocytes by 2-photon microscopy and digital image–processing techniques. *Circ Res*. 1999;84:266–275.
31. Soeller C, Cannell MB. Examination of the transverse tubular system in living cardiac rat myocytes by 2-photon microscopy and digital image–processing techniques. *Circ Res*. 1999;84:266–275,
32. Zhang, X.-Q., Song, J., Rothblum L.I., Lun, M., Wang, X., Ding,F., Dunn,J., Lytton, J., McDermott, P. J., and Cheung, J.Y., 'Overexpression of Na+/Ca2+ exchanger alters

contractility and SR Ca2+ contents in adult rat myocytes,' Am. J. Physiol. 281: H2079-2088, 2001.

33. Biermann M. Rubart M. Moreno A. Wu J, Josiah-Durant A., Zipes DP, "differential effects of cytochalasin D and 2.3. butanedione monocime on isometric twitch force and transmembrane action potential in isolated ventricular muscle: implications for optical measurements of cardiac repolarization.", PMID 9869534;
34. Webb, R. H., and Dorey, C. K. (1990). The pixellated image. *In* "The Handbook of Biological Confocal Microscopy" (J. B. Pawley, ed) pp. 41-51. Plenum, New York.
35. Art, J. (1990). Photon detectors for confocal microscopy. *In* "The Handbook of Biological Confocal Microscopy" **(J.** B. Pawley, ed.) pp. 41-51. Plenum, New York.
36. Pawley, J. B., and Smallcomb, A. (1992). An introduction to practical confocal microscopy: The ultimate form of biological light microscopy? *copica.* **1,** 58-73. (Venezuela).
37. Pawley, J. B., and Centonze, V. E. (1994). Practical laser-scanning confocal light microscopy: obtaining optimal performance from your instrument. *In* "Cell Biology: A Laboratory Handbook" ed.), Academic Press, NY.
38. Proakis, J., Rader C, Ling F., and Nikias C. "Advanced digital signal processing, Chapter 8: Power Spectrum Estimation", p.473, Macmillan Publish Company, New York, 1992.
39. Claude Rulliere, "femtosecond laser pulses:principles and experiments, 2 edition", Springer, Oct. 2002;
40. Z. Bor, "Distortion of femtosecond laser pulses in lenses and lens system," J.Mod.Opt.35, 1907-1918 (1988);
41. Z. Bor and Z.L.Horvath, " Distortion of femtosecond pulse fronts in lenses" in Topics in Applied Physics, M. Stuke, Ed., Springer, Berlin, 1992, Vol. 70, pp. 87-94;

42. M.Kempe, U. Stamm, B. Wilhelmi, and W. Rudolph, “Spatial and temporal transformation of femtosecond laser pulses by lenses and lens system.” J.Opt.Soc.Am, B 9, 1158-1165;
43. Z. Bor, Z. Gogolak and G. Szabo, “Femtosecond-resolution pulse-front distortion measurement by time-of-flight intermetry”, Optical Letter, 14, 862-864, 1989;
44. M. Kempe and W. Rudolph, “Analysis of confocal microscopy under ultrashort light-pulse illumination”, J.Opt.Soc.Am.A, Vol. 10, No. 2. p.240, Feb. 1993;
45. Min Gu, T.Tannous, C.J.R.Shepperd, “Three-dimensional confocal fluorescence imaging under ultrashort pulse illumination”, Optical communication, 117, pp406-412, 1995;
46. Joseph R. Lakowicz, “Principles of fluorescence spectroscopy, 2ed”, Kulwer Academic/Plenum Publishers, New York, 1999;
47. Philip L. Johnson, W. S., Tamara C. Baynham, and Stephen B. Knisley (1999). "Errors caused by combination of Di-4 ANEPPS and Fluo3/4 for simultaneous of transmembrane potentials and intracellular calcium."

Chapter 4 OPTICAL COMBING AND ITS APPLICATION IN RECOVERY OF RETINA REATTACHMENT SURGERY

4.1 Introduction

Retinal detachment refers to separation of the inner layers of the retina from the underlying retinal pigment epithelium. It can cause degeneration of the retina, and cause permanent vision loss if not promptly treated and hence is considered an ocular emergency. Currently, the only treatment available for retinal detachment is surgical reattachment.

An analytical treatment to the mechanism of vision loss due to detachment is presented in [9]. The findings from that model provide a novel explanation for the mechanism of visual loss due to detachment, i.e., diffusion caused by the misalignment of the photoreceptors. During post surgery recovery, the photoreceptors and pigment epithelium regenerate and regain original contour, thus the vision can continue to improve over many months. Accelerating recovery requires a method to enhance photoreceptor realignment.

In this part, we present a novel method called “optical combing”, which can potentially improve the retina reattachment surgery results. Optical combing adopts the working principle of optical tweezers and is implemented by scanning a focused laser beam on the misaligned photoreceptors. A tightly focused laser beam can produce a trapping force when it is incident on a transparent micro-object. The trapping force can pull the micro-objects to the central point of the focused laser beam.

In our design, a focused laser beam or a focused laser beam array is applied onto the misaligned photoreceptors. By moving the laser beam or laser beam array in one direction back and forth, we expect the misaligned photoreceptors can be aligned to their original orientations just like combing hairs. In our preliminary experiments, a set of misaligned micro glass rods was rotated and re-aligned by applying this optical combing technique, which in turn verified the feasibility of our theory. The same technique was applied to a detached bovine retina in recent experiments. It is difficult to clearly identify the experimental results because the bovine retina sample has a complicated structure with thickness of several millimeters. The photoreceptors are transparent and the retina sample looks translucent in a microscope with little contrast. To further prove the feasibility of optical combing, a better monitoring technique, such as the confocal microscope technique, needs to be combined with our experimental setup.

This study is organized as follows: First, we present the primary physical features about retina detachment and the way it reduces vision. After that, a literature review of optical tweezers is provided. In section 4.3, a ray-optics model is then given to describe the forces exerted on a dielectric micro-cylindrical object in a single-beam gradient force optical trap. Simulation results for the proposed model are also reported. Preliminary experimental results are presented in section 4.3. In section 4.4 we address our future plan on this project and some obstacles we have met. Other optical tweezers designs that can be potentially applied to optical combing are also discussed.

4.2 Retina Detachment and Optical Tweezers

4.2.1 Retina detachment

The retina is the light-sensitive layer of tissue that lines the inside of the eye and sends visual messages through the optic nerve to the brain. Retina detachment is a medical emergency. The symptoms include a sudden or gradual increase in either the number of floaters, which are little "cobwebs" or specks that float about in patients' field of vision, and/or light flashes in the eye. Another symptom is the appearance of a curtain over the field of vision.

There are three different types of retinal detachment. The first, rhegmatogenous, a tear or break in the retina, allows fluid to get under the retina and separate the retina from the retinal pigment epithelium (RPE), the pigmented cell layer that nourishes the retina. These types of retinal detachments are the most common. The second is tractional; in this type of detachment scar tissue on the retina's surface contracts and causes the retina to separate from the RPE. This type of detachment is less common. The third is called exudative and is frequently caused by retinal diseases, such as inflammatory disorders and injury/trauma to the eye.

With modern therapy, over 90 percent of those with retinal detachment can be successfully treated, although sometimes a second treatment is needed. However, the visual outcome is not always predictable. The final visual result may not be known for several months after surgery. Even under the best of circumstances, and even after multiple attempts to repair, treatment sometimes fails and vision may eventually be lost.

The primary physical feature of retinal detachment that leads to the diagnosis is a gray discoloration of the elevated retina. This discoloration is directly related to the height of the detachment and reduces visibility of the underlying choroidal and vascular details. The treatment of retinal detachment entails mechanical repositioning of the retina against the pigment epithelium and reduction of the subretinal fluid by means of sclera buckling and subretinal fluid drainage. However, these treatments are only indirect means of addressing the biological/optical aspects of impaired vision. Many patients with macula-off detachment have only partial vision recovery and there are no alternative non-surgical methods to improve vision.

A detached retina is translucent whereas an attached retina appears transparent, but the cause of this change in appearance has not been fully explained. One possible explanation is that an intrinsic abnormality of the retina due to impaired metabolism can lead to retinal edema. Although retinal edema certainly occurs in detachments[1], at least one day is required to develop after experimental separation from the pigment epithelium and it does not resolve immediately upon reattachment.[2] In contrast, a detached retina regains its transparency as soon as it is reattached, either by external or internal subretinal fluid drainage, or with perfluorocarbon liquids. Moreover, cystoid macular edema does not impair retinal transparency in an attached retina. A second possibility is retinal hypoxia. Although a detached retina is probably relatively hypoxic because of its separation from the choroid,

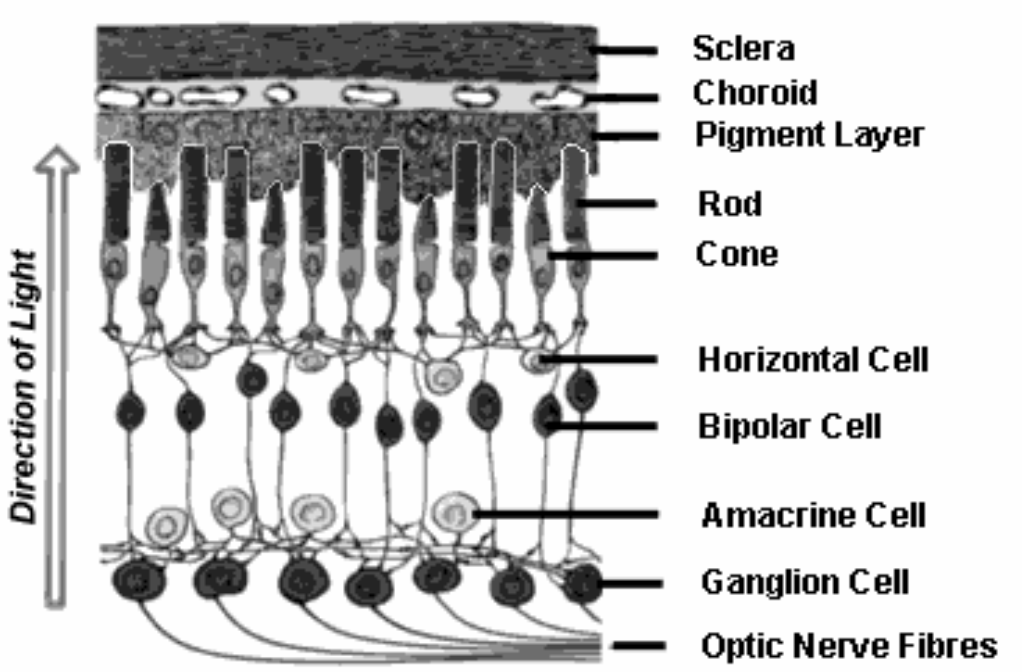

Figure 4.1 Courtesy from http://www.catalase.com/

hypoxia alone is not likely to cause central retinal artery closure for up to 30 minutes and does not cause retinal whitening. Thus, an intrinsic retinal metabolic abnormality likely does not account for the grayness of the detached retina. A third possible explanation for retinal grayness could be a loss of clarity of the subretinal fluid. However, none of the above hypotheses can explain why detached a retina regains its transparency as soon as it reattaches.

The attached retina appears transparent because it lacks pigment and has an orderly cellular architecture. In addition, the photoreceptors interdigitate with the underlying pigment epithelium to provide a smooth transition from one tissue to another. These features minimize light scattering.

Retinal detachment causes irregularities of the photoreceptors and pigment epithelium, thus light is diffused by the disordered photoreceptors. This is known as the volume scattering effect in which the light is scattered across the increased 3-dimensional space of the light path of the elevated retina. That is, since the photoreceptors are in their natural parallel arrangement the light is scattered throughout the increased volume of the retina and the subretinal space.

The scattering of light in ex-vivo postmortem bovine retinas and transparent Scotch tape at different heights from the reference plane has been compared [9]. The scotch tape model demonstrates that light scatters when the surface of the medium is irregular. In this case, irregularities in the posterior (adhesive) surface of the tape are larger than the wavelength of visible light passing through it; therefore tape is translucent or light gray in color. In addition, tape held over a formed image such as text blurs the view of the image. When pressed against a smooth surface, the tape immediately appears transparent because the irregular posterior surface is smoothed. Likewise, when the retina is detached, photoreceptor outer segments no longer interdigitate with the pigment epithelium and create an irregular surface as shown in electron micrographic studies by Kroll and Machemer.[1] Thus, scatter occurs if the irregularities of the outer segments exceed the wavelength of light. The results indicate that light diffusion by misaligned photoreceptor cells is one of the reasons causing grayness in detached retinas.

To maximize visual recovery after retinal detachment, the scattering effects must be eliminated. In other words, the retinal must be reattached in its native position so that photoreceptors can realign and have a smooth interface with the pigment epithelium. Indeed, psychophysical evidence for photoreceptor misalignment in patients with retinal detachment has been shown by the Stiles-

Crawford effect[3] and macular electroretinography in central serous chorioretinoaphy[4]. This leads us to believe that non-surgical alignment of the photoreceptor cells will reduce grayness and improve vision to some degree.

4.2.2 Optical tweezers

Optical tweezers have been successfully applied to a wide range of fields since its inception in the early 1970s[5]. Optical tweezers offer the promise of being 'cell friendly' for biological objects when applied at certain wavelengths. It is possible to remotely apply controlled forces on living cells, internal parts of cells, and large biological molecules without inflicting detectable optical damage. With the help of Pico Newton order optical force and down to angstroms positioning capability, the single-beam gradient force optical tweezers can trap or manipulate objects such as biopolymers, cells, and single biological macromolecules[6-9].

Optical tweezers can be used purely as manipulators and positioning devices to confine or constrain microscopic objects, as well as to organize, assemble, locate, or modify them. Due to their exquisitely controllable force-exerting properties, optical tweezers are also useful for a variety of nano-mechanical measurements, particularly those with biological applications.

Theoretical studies of optical tweezers have developed relatively slowly compared to the current experimental works. Several factors conspired to make general theories difficult to develop, such as large numerical apertures employed, variations in the size, shape and composition of trapped objects etc. A thorough description of the trapping power depends on the size of the particle being studied. If the diameter of the particle is greater than the wavelength of light, the ray-optics model can be

used. If the diameter of the particle is less than the wavelength of light, the electromagnetic and quantum theories have to be appreciated. For particles that are in between these two models, an additional model must be used. The electromagnetic and quantum theory method uses a full vector wave rigorous solution of the Maxwell Equations[10, 11]. Therefore it provides an accurate solution compared to the ray-optics method. However, the theoretical analysis with electromagnetic and quantum theory for non-spherical objects subject to the light beam is quite mathematically involved and difficult to apply to arbitrary light-beam profiles. The ray-optics model[7] has proven to be successful in the geometric optics regime. Although the ray-optics model [3] is less exact, it is in reasonable agreement with the forces observed experimentally. The simplified approach can easily be applied to non-spherical figures without much change; we therefore resort to it in our simulation study of optical combing.

The structure of the photoreceptors is shown in Figure 4.1. The photoreceptor, which consists of a rod and a cone, is shaped like a spherical-ended cylinder. The theoretical investigation of the optical trapping of cylindrical micro-objects has been reported. It has been proven that optical tweezers are a good tool to manipulate cylindrical micro-objects [12]. Therefore, scanned optical tweezers may be the ideal solution to align the misaligned retina cells.

A drawback of optical trapping is the damage induced by the intense trapping light. In practice, such damage limits the exposure time for trapped specimens and thus is a serious problem for some biomedical studies; particular those in vivo. In one of our experiments, we tried to expose the living retina directly to the focused laser beam with power 80mW at a wavelength of 532nm. In this case, the water in the tissue boiled after being exposed to the focused laser beam for 2-3 seconds, and the

photoreceptors were burned out. It is obvious that the heating effect can cause disasterous damage to ocular neurons and underlying retinal pigment epithelium.

Since 1987, practical progress has been made toward decreasing photo damage in optical trapping systems, primarily through the choice of trapping lasers with wavelengths in the near-infrared region [13]. The potential for damage is readily appreciated by computing the light level at the diffraction-limited focus of a typical trapping laser; for a power of just 100mW, the intensity is $10^7\,\mathrm{W}/cm^2$, with an associated flux of 10^{26} photon/s. cm^2. Proposed mechanisms for photo damage include linear absorbing[14], two-photon absorption[15, 16], and photochemical processes leading to the creation of reactive chemical species[17, 18].

Focal heating caused by linear absorption in near infrared wavelengths receives considerable attention as a limiting factor in the rapidly evolving techniques of optical trapping. There is a relative minimum of water absorption and of chromospheres absorption when working in the wavelength window 700-1100nm. The main contribution of heating is due to the absorption of water because viable biological specimens consist mainly of water. A very common and well-tested wavelength is 1064nm; another wavelength, at which there is only a small increase of temperature with increasing laser power, is around 800nm.

Experimental data of temperature-sensitive fluorescent dye in Chinese hamster ovary (CHO) cells and liposome have been reported. They confirmed the prediction that local heating of micron-sized specimens is negligible from a tightly focused CW laser source with near-infrared working wavelength. Further studies, based on assays of the rates of chromosome bridge formation in rat

kangaroo cells or cloning efficiency in CHO cells, established rough action spectra for damage over portions of the near-infrared region. This work suggests that a two-photon process leads to the loss of viability in human spermatozoa and decrease of CHO cell-cloning efficiency. In addition, work with fluorescent probes demonstrated no changes in the intracellular pH of trapped cells and no detectable changes in DNA structure under CW laser illumination.

Experimental results quantitatively showed sample heating is around 1-1.5 centigrade per 100mW when applying laser light at the proper wavelength. Moreover, the results of heating vary with different types of cells [18]. In adult salamander retinal cultures, all types of nerve cells including the photosensitive rod and cone cells could be trapped with a 980nm laser without any apparent short or long-term injury. In other cell systems, effects of the optical trap on survival were wavelength dependent[19] [20]. For CHO cells, the band of near-infrared wavelengths which gave optimal results was relatively narrow; cell proliferation was maximal at wavelength of 950-990nm and dramatically reduced at 900 and 1064nm [20]. Furthermore, the improvement in cell survival and proliferation with 950-990 nm over other wavelengths was more pronounced when the power of the laser was increased. In agreement with these data, a laser beam with wavelength of 1064nm at high power (>200mW) has been reported to damage neurons[21].

Previous work of micromanipulation by optical tweezers has been tested in a culture of mature isolated retinal cells to determine its potential in creating synaptic circuits in vitro [22]. Rod and cone photoreceptors as well as other retinal nerve cell types could be optically trapped with a 980nm diode laser mounted on an inverted light microscope using a 40X oil immersion objective numerical aperture of 1.3. Manipulation was done under sterile conditions using transparent culture dishes. To

form cell groups, one half of a culture dish was made less adhesive by application of a thin layer of silicone elastomer. Unattached cells were trapped and relocated next to cells lying on an adhesive culture substrate. With practice, up to 60% of trapped cells survived for 2 more days. The pattern and outgrowth rate for manipulated cells was comparable to un-manipulated cells. Cell growth patterns were not altered. The same sequence and timing of process outgrowth was observed in trapped and relocated photoreceptors. Organelle, nuclear and cytoplasmic structure of manipulation cells was completely normal and in photoreceptors, synaptic vesicles and ribbons were intact.

Overall, photoreceptors are photon-absorbing cells and, therefore, are susceptible to damage from the laser light. As previously reported, absorbance of light does not prevent rod and cone cells from being optically trapped and moved through the cell suspension. And optical trapping was possible with all types of photoreceptors. Optical tweezers, therefore, provide a benign technique to micromanipulate whole neurons.

4. 3 **Optical combing for the misaligned photoreceptors**

4.3.1 Optical trapping force

The geometrical optical approach can be applied to objects whose dimensions are much larger than the wavelength of light. And the Gaussian beam can be decomposed into individual rays. Each ray, with corresponding intensity, is incident onto a spherical-ended cylindrical object. In the geometrical optical approach, a ray is also treated as a stream of photons. When applying rays to the interface of

two dielectric materials with different reflective index, part of the photons are reflected, and part are refracted.

In our simulation, a spherical-ended cylindrical object with a reflective index of 1.55 stands on one end on the substrate and is immersed in water with a reflective index of 1.333. It has length L around 60um and radius R around 3um. Its cylindrical axis is aligned along the Z-axis, and the incident TEM_{00} Gaussian beam is directed along the -Z axis direction as shown in Figure 4.2. The beam waist of the Gaussian beam locates at the same height as the highest point of the spherical-ended cylindrical object.

We simplify the model by assuming that the reflected photons just leave and do not come back to the object. The refracted photons then travel through the cylinder surface and intersect with the other side of the cylinder body or the end surface of the cylinder. The force applied by the photon stream on the object is governed by Newton's Second Law:

$$F = dp/dt \qquad (4.1)$$

dp is the momentum transferred to the object by the photon stream, dt is the time interval over which dp is measured.

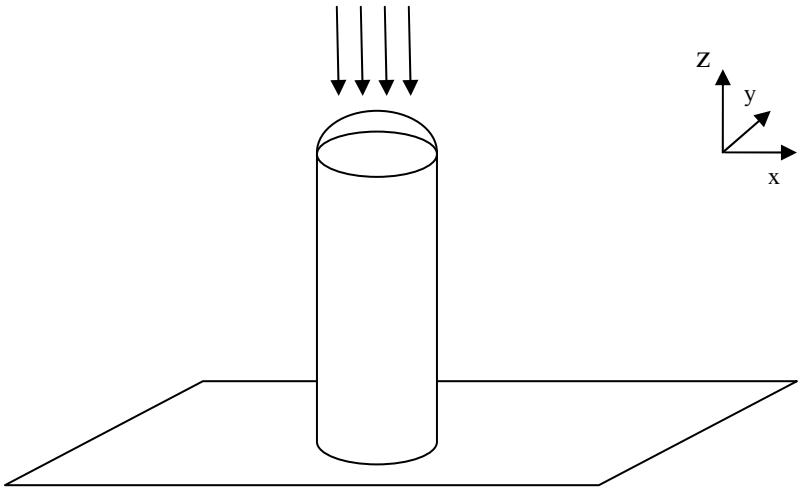

Fig. 4.2 Cylindrical object located along the Z axis with light incident normally onto it end surface.

The momentum transferred between the photon and the cylindrical object can be described as:

$$\begin{aligned}
\Delta p_{\vec{r}r} &= p_0\left[n_w\left(\vec{i}_i - \vec{i}_r\right)\cdot\vec{r}\right] \\
\Delta p_{\vec{r}t} &= p_0\left[\left(n_w\vec{i}_i - n_g\vec{i}_t\right)\cdot\vec{r}\right] \\
\Delta p_{\vec{z}r} &= p_0\left[\left(n_w\vec{i}_i - n_g\vec{i}_t\right)\cdot\vec{z}\right] \\
\Delta p_{\vec{z}t} &= p_0\left[\left(n_w\vec{i}_i - n_g\vec{i}_t\right)\cdot\vec{z}\right]
\end{aligned} \qquad (4.2)$$

$\vec{i}_i$, $\vec{i}_r$ and $\vec{i}_t$ are the incident, reflected and refracted light vectors correspondingly; $\vec{r}$ and $\vec{z}$ are the radial direction vector and z axis vector respectively; p_0 is the momentum of a single photon in vacuum given by $\frac{h}{\lambda}$; n_w and n_g are the reflective index of water and glass accordingly.

The numbers of photons that are reflected and refracted at each surface depend on the incident angle and the polarization of the light, and can be obtained separately from the power reflectance and transmittance coefficients. These coefficients are expressed by the Fresnel formulae.

$$
\begin{aligned}
t_{II} &= \frac{2\sin\theta_t \cos\theta_i}{\sin(\theta_i+\theta_t)\cos(\theta_i-\theta_t)} \\
t_{\perp} &= \frac{2\sin\theta_t \cos\theta_i}{\sin(\theta_i+\theta_t)} \\
r_{II} &= \frac{\tan(\theta_i-\theta_t)}{\tan(\theta_i+\theta_t)} \\
r_{\perp} &= \frac{\sin(\theta_i-\theta_t)}{\sin(\theta_i+\theta_t)}
\end{aligned}
\qquad (4.3)
$$

$t_{II}, t_{\perp}, r_{II}, r_{\perp}$ refer to the transmittance and reflectance coefficients of TE and TM mode respectively. θ_i, θ_t refer to the incident angle and transmission angle of ray accordingly.

In our study, we assume that the light is composed of an equal number of photons in both TE and TM polarization, and the power reflectance and transmittance can then be described as:

$$R = \left| \frac{r_{II} + r_{\perp}}{2} \right|^2 \tag{4.4}$$

We obtain the following equations by substituting the Equation 4.3 into 4.4,

$$R = \frac{(n_0 * n_s)^2 * [Cos^2(\theta_i) - Cos^2(\theta_t)]^2}{\{n_0 * n_s * [Cos^2(\theta_i) + Cos^2(\theta_t)]^2 + (n_0^2 + n_s^2) * Cos\theta_i * Cos\theta_t\}^2} \tag{4.5}$$

$$T = 1 - R$$

n_0, n_s are the reflect indexes of the micro-object and the environmental mediums.

Therefore we can express the momentum that the cylinder object obtained from the two interactions as follows:

$$dP_r = R * \Delta P_{1\vec{r}r} + T * \Delta P_{1\vec{r}t} + R * T * \Delta P_{2\vec{r}r} + T^2 * \Delta P_{2\vec{r}t} \tag{4.6}$$

$$dP_z = R * \Delta P_{1\vec{z}r} + T * \Delta P_{1\vec{z}t} + R * T * \Delta P_{2\vec{z}r} + T^2 * \Delta P_{2\vec{z}t} \tag{4.7}$$

Finally, the element of force, dF_r and dF_z, can be described as:

$$\begin{aligned} dF_r &= \frac{2 * I}{E_p} \cdot \frac{1}{\pi \cdot W(z)^2} \cdot \exp\left[\frac{-2 * \rho^2}{W(z)^2} \right] dp_r dA \\ dF_z &= \frac{2 * I}{E_p} \cdot \frac{1}{\pi \cdot W(z)^2} \cdot \exp\left[\frac{-2 * \rho^2}{W(z)^2} \right] dp_z dA \end{aligned} \tag{4.8}$$

Where I is the intensity of the laser beam, and E_p is the energy of a photon. $W(z)$ and ρ are parameters of the Gaussian beam expression.

4.3.1.1 Modeling of radial force

The simulation results of radial force, computed by numerical integration, are shown in figure (4.3), figure (4.4) and figure (4.5). In these simulation results, we depict the radial force acting on the micro-cylinder in a single-beam gradient optical trap. In figure (4.3), a three-dimension graph describes the radial force exerted by the focused Gaussian beam onto the spherical-ended cylindrical object verses the transverse displacement of the central point of the Gaussian beam to the symmetrical axis of the cylinder. The radial trapping force becomes zero when the central point of the Gaussian beam coincides with the symmetrical axis of the spherical-end cylinder. As the displacement increases, the absolute value of the trapping force increases. However, acting as a trapping force, the direction of the force is in the opposite direction to that of the radial offset, therefore the value of the force is negative. The absolute value of the force reaches its peak when the waist of the beam locates somewhere near the edge of the cylindrical object. After that, the trapping force decreases gradually to zero when the radial displacement keeps increasing, which means that there are less and less photons interacting with the object as the light beam moves away from the cylindrical object, and there is less momentum transferred to the cylindrical object. The radial force serves as a trapping force to pull the object toward the strongest point of the focused beam. In a special case, if one end of the object is fixed, the force exerts a torque onto the cylindrical-object and makes it rotate around the fixed end.

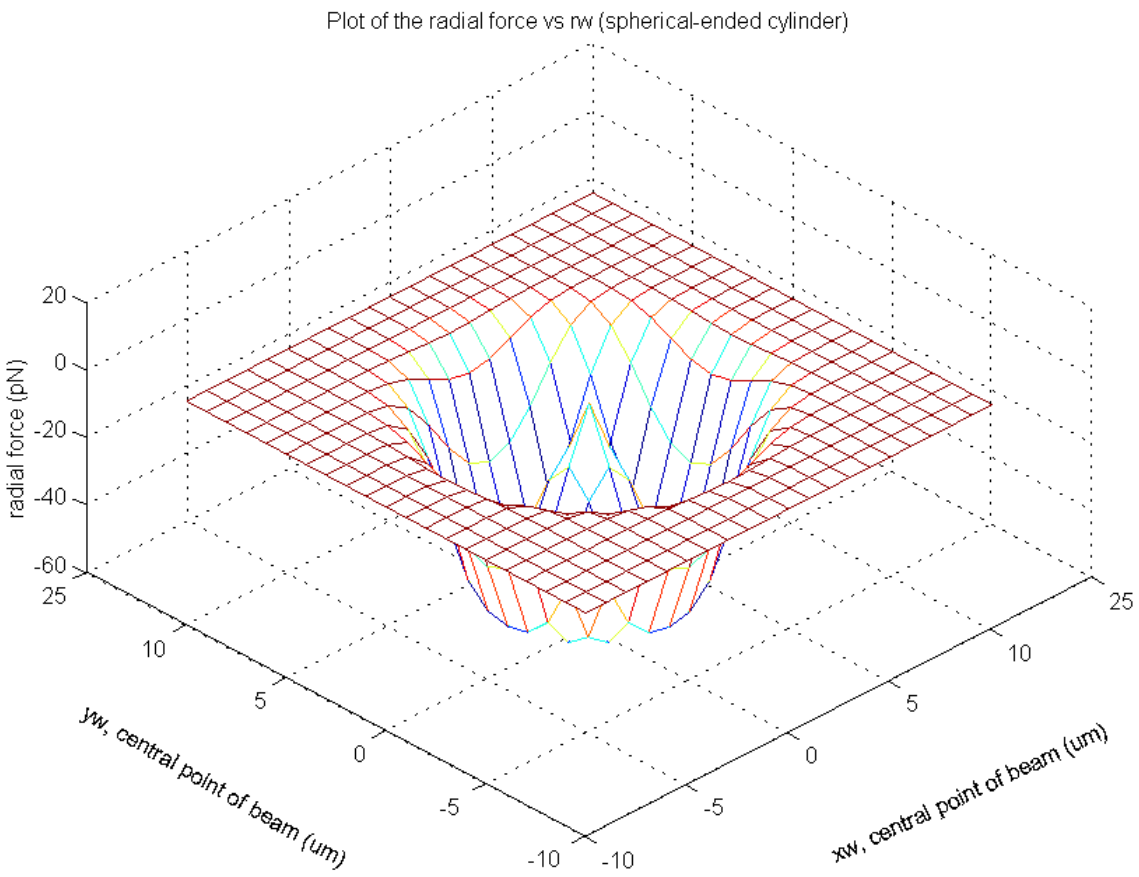

Figure (4.3) Radial force versus radial displacement. beam waist=2um; offset displacement between beam waist and symmetrical axis of spherical-ended cylinder=5um; radius of cylinder=5um, laser power=50mw, wavelength of light=0.514um.

In figure (4.4) and figure (4.5), we show similar radial force results in a one-dimensional graph. We can clearly see how the force varies as the displacement increases. Moreover, we compare the results by applying three different laser powers. As shown in these two figures, we get a larger trapping

force when the power of the laser increases. There are two more issues that need to be mentioned: First, the working wavelength of the light source becomes 0.85um instead of 0.514um in Figure (4.2). We can see that the trapping force becomes smaller when the working wavelength becomes larger. Second, the radii of the cylinder are not the same in figure (4.4) and figure (4.5). We can tell that the trapping force becomes larger when the radius of the cylindrical object increases; which means more photons interact and transfer momentum to the object.

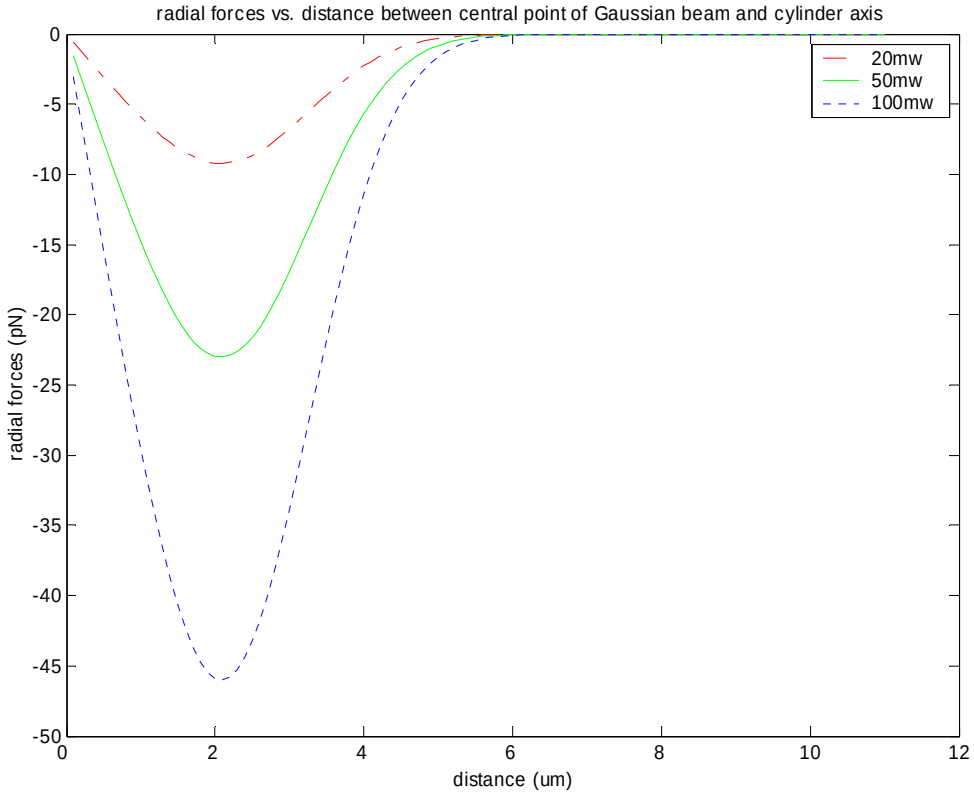

Figure (4.4) **Radial force vs. radial displacement** beam waist=2um; displacement between beam waist and symmetrical axis of spherical-ended cylinder=0um; radius of cylinder=3um, wavelength of light=0.85um.

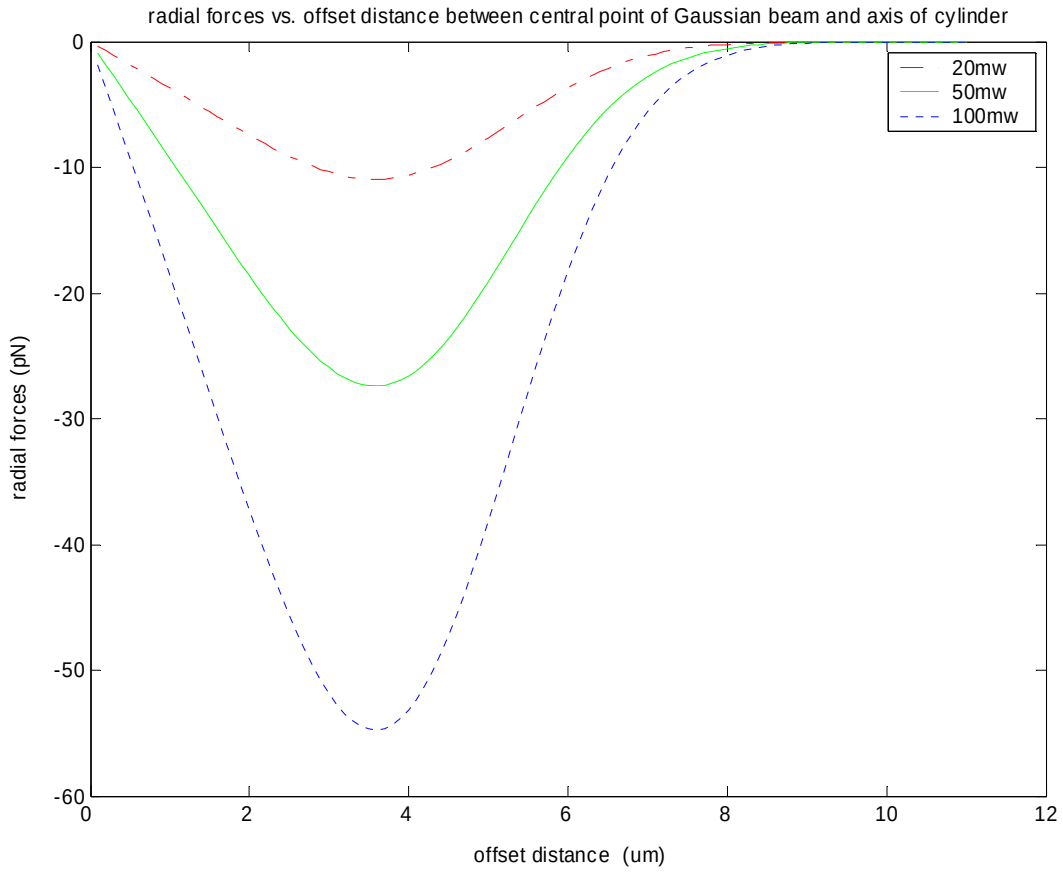

Figure (4.5) **Radial force vs. radial displacement.** beam waist=0.5um; displacement between beam waist and symmetrical axis of spherical-ended cylinder=1um; radius of cylinder=5um, wavelength of light=0.85um;

4.3.1.2 Modeling of axial force (Z-axis)

The Z-axis trapping force is investigated under the same scenario. In figure (4.6) and figure (4.7), we plot the axial force variation versus separation distance between the minimum waist of the Gaussian beam and highest point of the spherical-ended cylindrical object. The force is at its maximum value when the distance is zero, then gradually decreases to zero as the distance increases. Since the spherical end of the cylinder has a finite area, this simulation result can be easily interpreted that there are fewer photons interacting with the object as the beam waist gets further away from the object. Laser power (50mW) in figure 4.7 is different from that in figure 4.6 (20mW). The general shape of the curve does not change; however, the maximum value of the force increases and the curve shifts downward.

Figure 4.8 and 4.9 show the Z-axis force, plotted as a function of the (X,Y) coordinates which is the transversal position of the minimum beam waist. The graphs indicate that the axial force reaches its peak value when the central point of the Gaussian beam is located at the origin of the (X, Y) plane, which coincides with the symmetrical axis of the cylinder. The value of axial force decreases as the displacement increases. The curve is symmetrical to the Z-axis. The simulation result in Figure 4.9 varies more slowly than that in Figure 4.8. It is because the radius of the cylindrical object is 8um in Figure 4.9 comparing to 5um in Figure 4.8. This obeys the common sense that: the larger the radius of the object, the more photons interact with the object. In experiments, this means the focused laser beam exerts more force on micro-rods with larger radii.

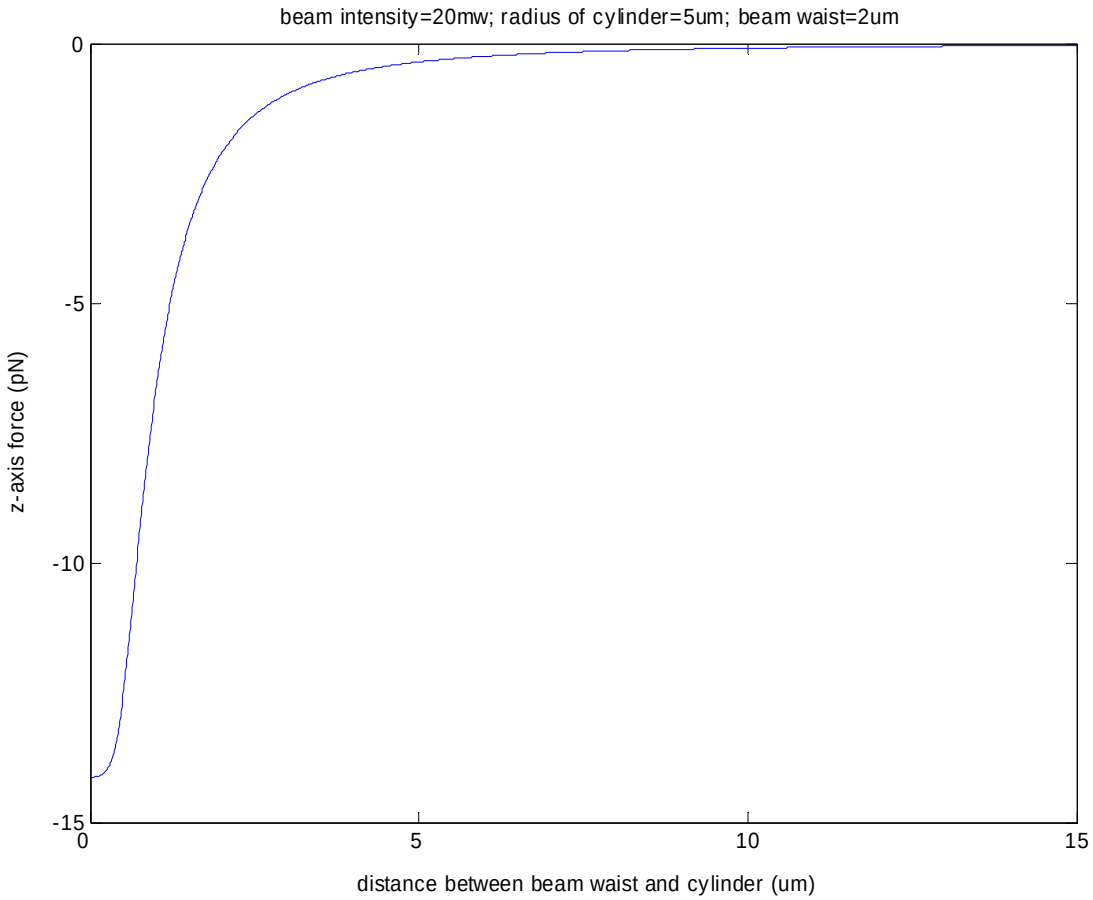

Figure (4.6) Z-axis force vs. the longitudinal distance between the Gaussian beam waist and the highest point of cylindrical object.

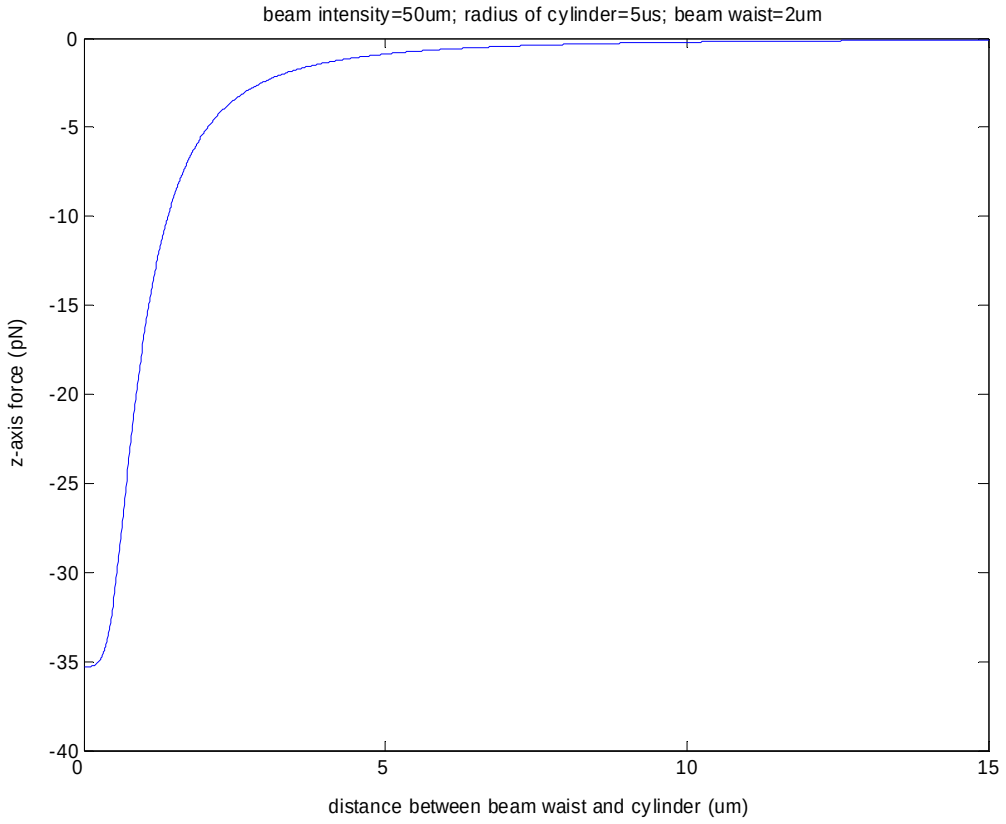

Figure (4.7) Z-axis force vs. the longitudinal distance between the Gaussian beam waist and the highest point of cylindrical object

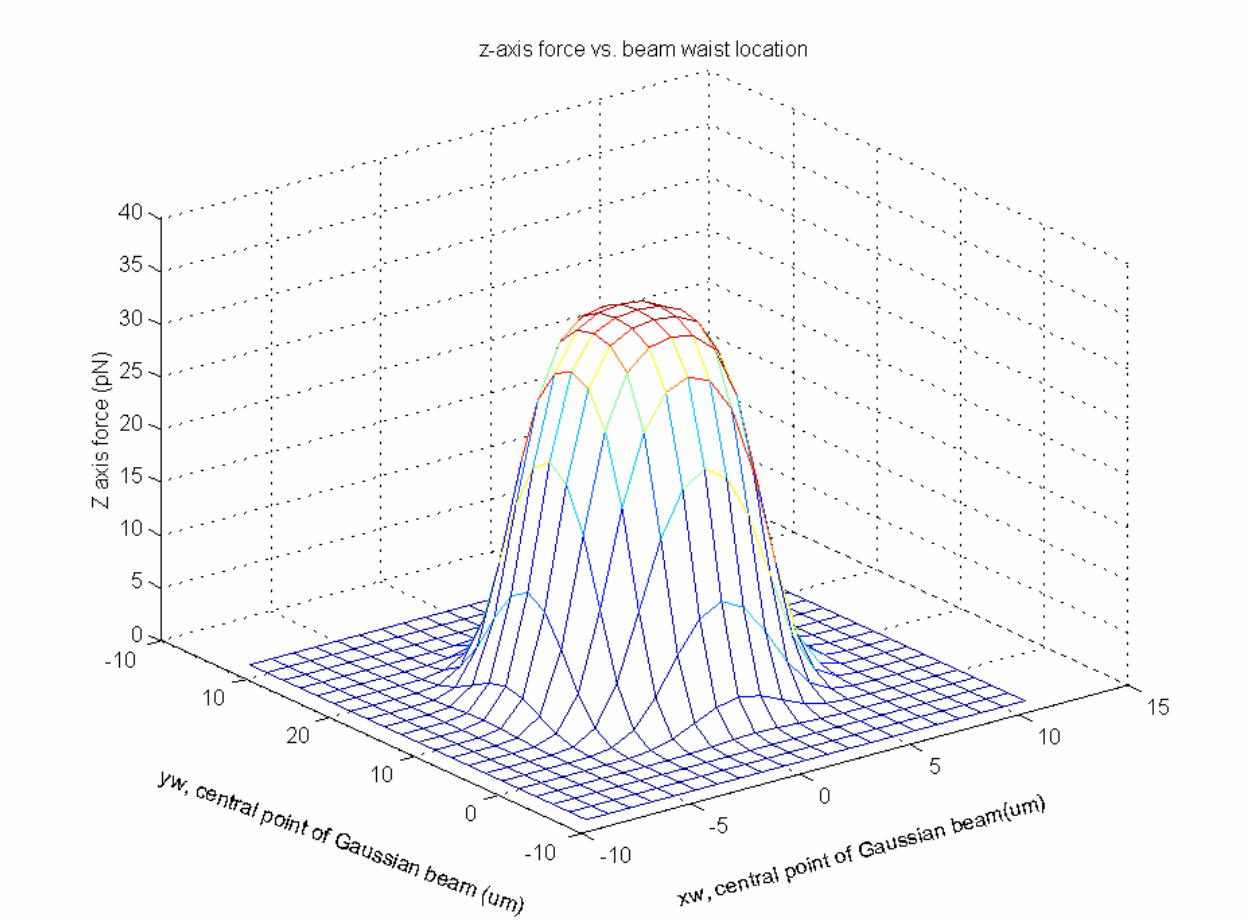

Figure (4.8) intensity of beam=50mw; Radius of cylinder=5um; transversal displacement of beam waist and symmetrical axis of cylinder=5um; wavelength=0.514um; ng=1.5468; nw=1.33; beam waist=2um.

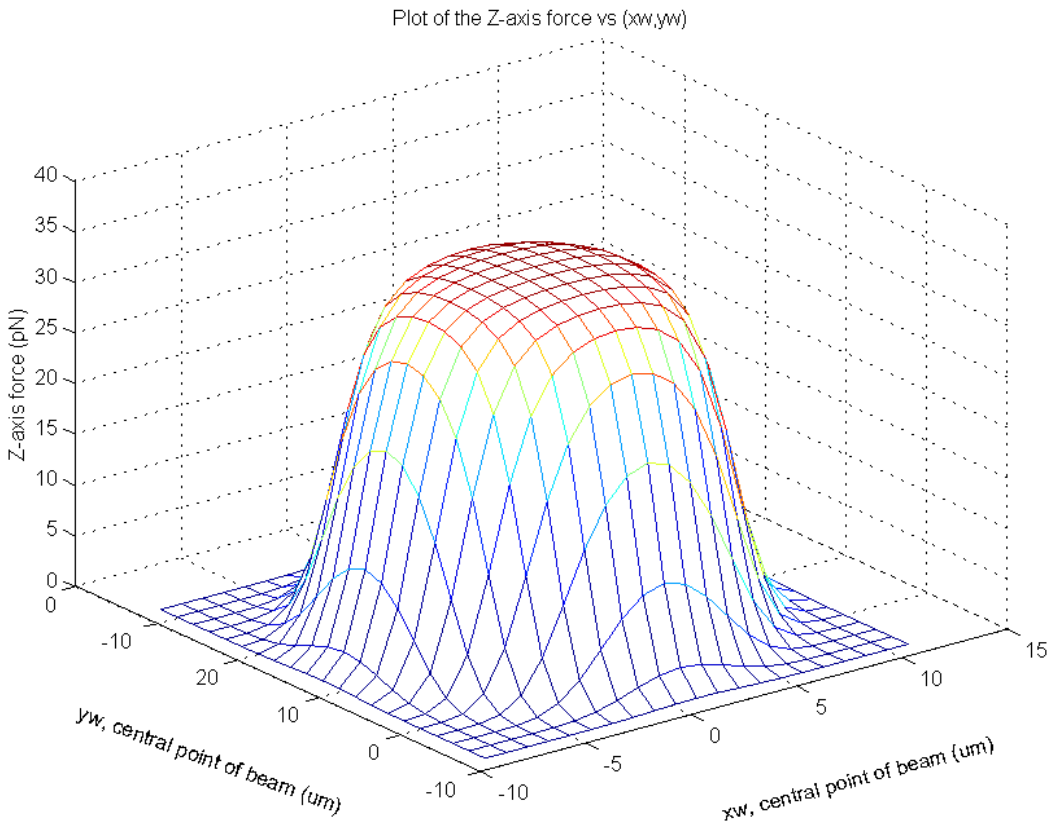

Figure (4.9) Beam waist=2um; transversal displacement between beam waist and symmetrical axis of cylindrical object=2um; radius of cylinder=8um; beam intensity=50mw; wavelength of beam=0.514um.

Our simulation results comply with the previous works [12]. Other studies also showed some key points of the trapping efficiency. Ashkin showed theoretically that the change in the intensity distribution of the incident laser beam is an important factor affecting the optical trapping efficiency [23]. Wright, et al., reported that the optical trapping efficiency increases as the numerical aperture of the objective lens and the size of the trapped particle increase [24].

4.3.2 Modeling the interaction between the focused optical light and retinal cells

The diameter of the rod is around several microns, which fits for the ray-optics model. Figure 4.10a shows a simplified diagram of the misaligned photoreceptors. To align the photoreceptors as in Figure 4.10b, the focused Gaussian beam needs to be applied to the rods and cones. By scanning the laser beam or moving the sample stage, we can therefore manipulate them in the same way that we did the cylindrical glass rods. The focused laser beam will work like a comb if we scan the light source back and forth. The trapping force will pull the rods and cones to the center of the focused light as the light source moves, so that the photoreceptors can be aligned along the moving direction of the light. The axial force also exert onto the photoreceptors, however, because the direction of the force is along the elongated axis of the cylindrical rod, it does not play an important role in the combing process. Depending on the position of the minimum beam waist, the force may direct upward and pulls the photoreceptors away from the pigment epithelium; or direct downward and press the rods to the pigment epithelium.

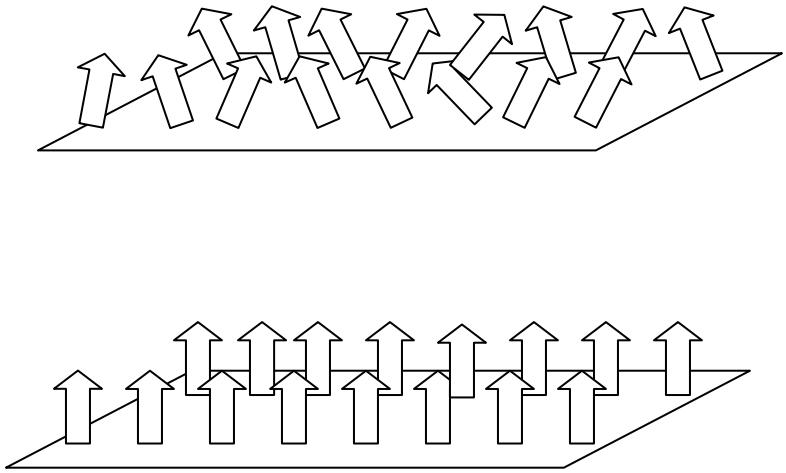

Figure 4.10. The misaligned photoreceptors compares to the well-aligned photoreceptors.

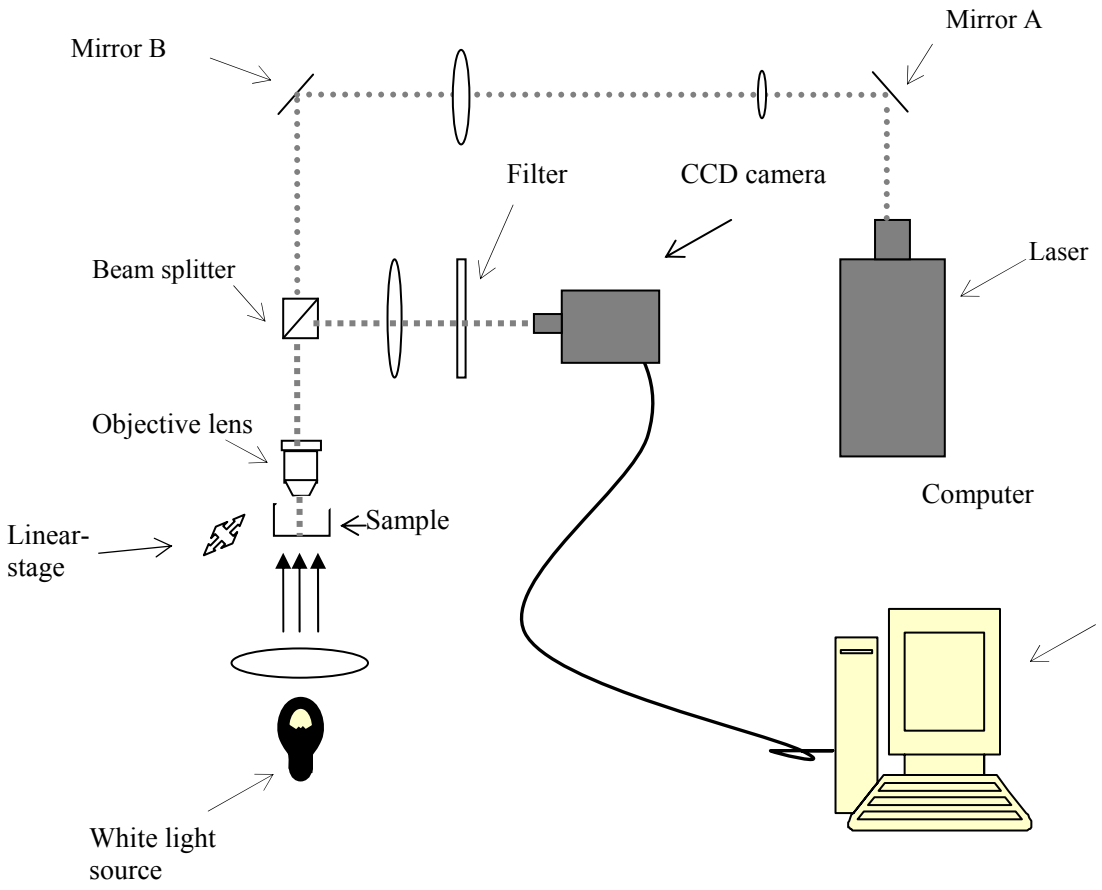

Figure (4.11) Schematic of experiment setup.

The schematic diagram of a single-beam optical trap is shown in Figure 4.11. In our experimental setup, two continuous wave laser systems are used, a Nd:Yag laser (1064nm) and a doubled-frequency Nd:Yag laser (532nm). Both laser systems can operate at a linearly polarized TEM00 Gaussian beam. The 532nm laser serves as an alignment tool of the setup since it is difficult to align the invisible infrared laser directly. To set up the experiment environment, we first align the 532nm laser with the infrared laser and then work with the green laser to build up the system. Once the optical tweezers setup works with the green laser, we switch to the infrared laser and do some fine tuning to make the system 'cell friendly'.

Shown in Figure 4.11, the light from the Nd:Yag laser system is directed onto a pair of collimating lenses to adjust the beam width, then the light beam with proper beam size is incident on a cube beam splitter. Part of the light is reflected and goes away and part of light transmits through the beam splitter and reaches the back aperture of the objective lens. Next the light is focused by the objective lens and produces a diffraction-limited minimum waist. The sample is placed in the chamber controlled by a 3-axis linear translation stage. When aligned with the objective lens, the sample is exposed to the focused beam and gets trapped. By moving the three-axis linear stage, we can manipulate the sample by the trap.

The operation of the optical trapping system depends on the ability of focusing light into a very small spot since the value of the trapping force is proportional to the gradient of the amplitude of the light beam. The smaller the spot can be focused, the bigger the trapping force that can be achieved. In the case of a Gaussian beam in the paraxial regime, the diameter of the focused spot can be expressed as:

Figure 4.12 The sample of a detached bovine retina

$$d \approx \frac{1.3\lambda f}{nw} \qquad (4.9)$$

Where λ is the wavelength of light, f is the focal length of the lens, n is the refractive index of the medium, and w is the beam waist. We can see from the equation that the only parameter that can be adjusted is the waist width since all other parameters are fixed as long as the equipment settings are fixed. Furthermore, a beam can not be focused to a diffraction limited spot if the diameter of the incident beam is smaller than the size of the lens aperture. Conversely, a large incident beam would result in loss of optical power, which consequently reduces the trapping efficiency. In such a case, choosing a proper ratio of the beam radius-to-the aperture radius can be a dilemma. Experimental results showed that the optical trapping efficiency increased with the ratio of the beam radius-to-the aperture radius and became constant over the region $w_0 / R \geq 1.5$ [25]. While the opening region could mean some problems with the simple conclusion, a ratio which is a little bit larger than 1.5 will be a reasonable value to obtain the best trapping efficiency. In turn, a pair of collimating lenses with different focus length is used as the beam size controller in the system setup as shown in figure 4.11.

It is very difficult to orient the cylinders' elongated axis along the Z axis, which means the cylinders can hardly stand on one end with no exerted force. In our first experiment, we leave the cylinder glass lying on a glass substrate with the laser beam incident from the top. The cylinders are originally lying randomly, i.e., the elongated axis of cylinders orient along different directions. This is shown in Figure (4.13). After we move the focused laser beam close to one end of the cylinder and rotate the cylinder by moving the laser beam, we align the cylinders in one direction as shown in figure (4.14).

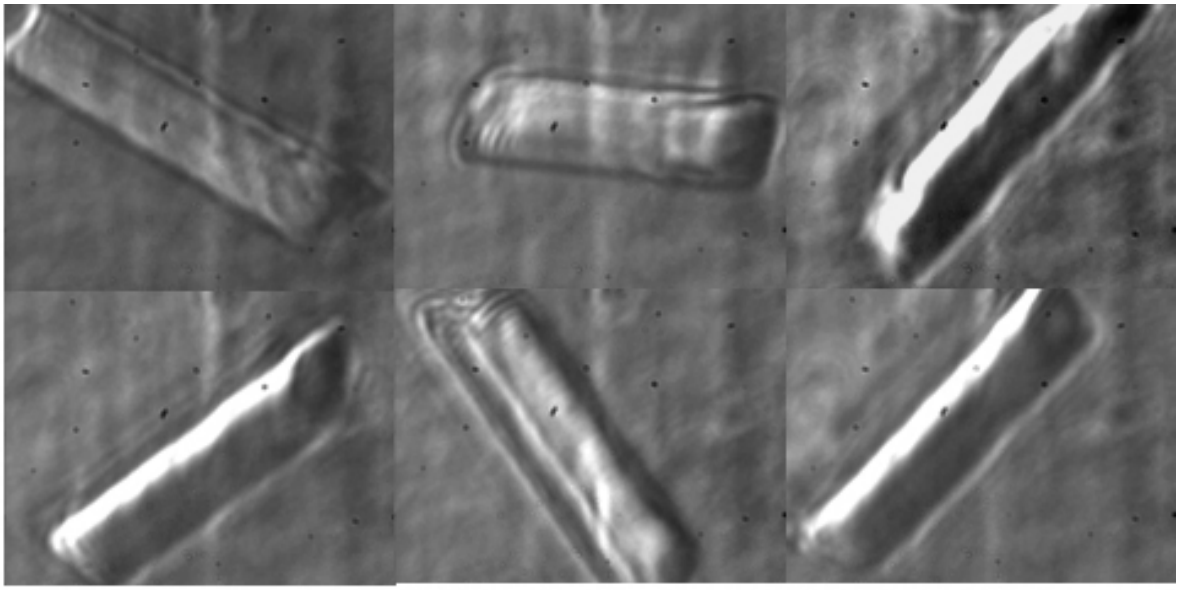

Figure 4.13 cylinders in random direction

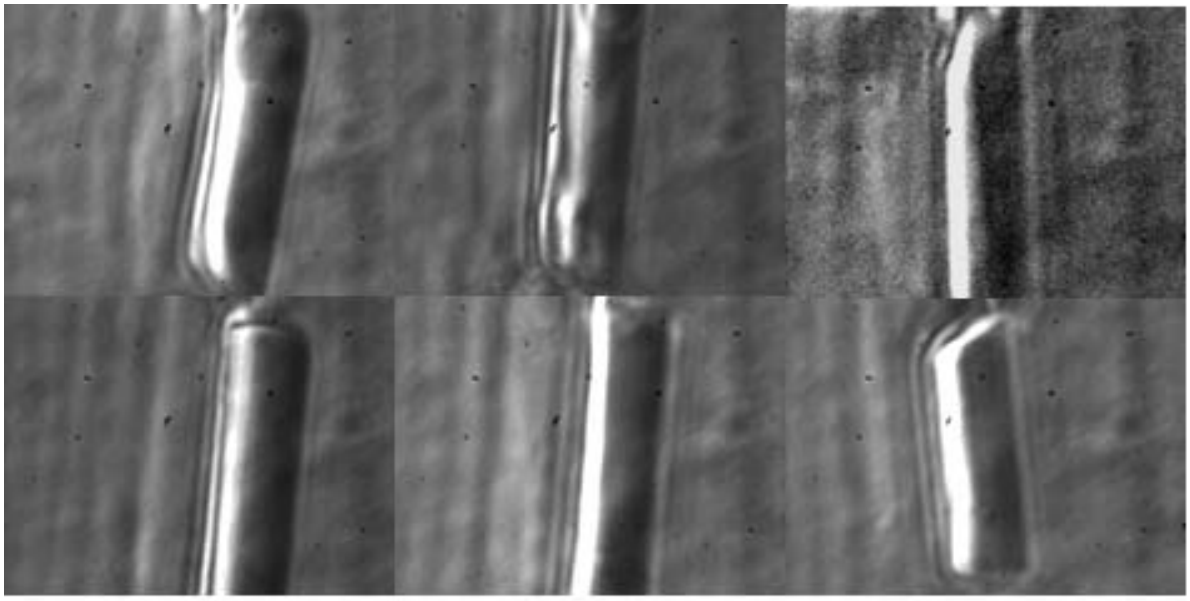

Figure 4.14 cylinders aligned by optical tweezers

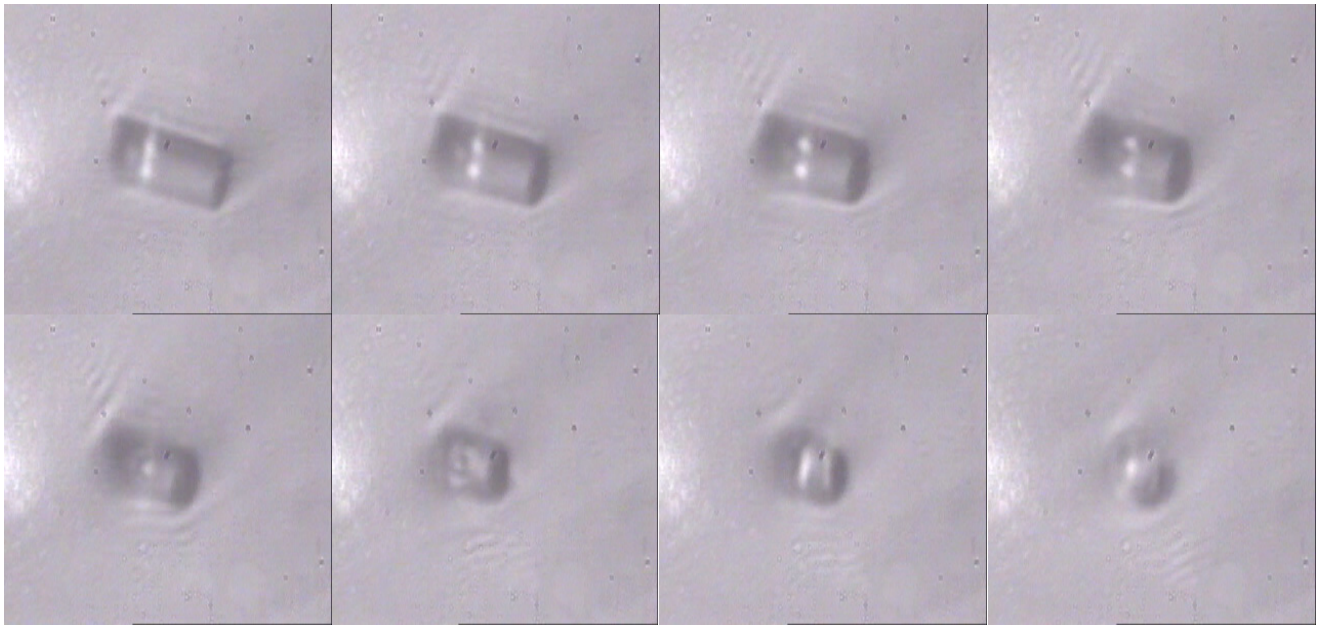

Figure 4.15 the micro-cylindrical object rotated in longitudinal plane.

Figure 4.15 shows another experimental result of rotating the micro-cylindrical object in the longitudinal plane. The micro-object is lying on the bottom of the sample holder while immersed in distilled water. As the focused laser beam moves close to one of the micro-objects and is finally incident on it, the micro-rod is pulled to stand up. A series of figures depict the process that the cylindrical gradually stands up from the lying position. In Figure 4.16, we show additional results after the micro-object has been pulled to stand up. While continuously moving the incident laser beam in the transversal plane, the micro-object can also be pulled to follow the movement of the laser focus. While moving by the focused beam, the micro-rod rotates itself along the elongated axis. The force of pulling can be estimated by subtracting the buoyant force from the weight of the micro-object. The trapping of the micro-rod is firm since the micro-object even follows the movement of focused beam and steps over another lying micro-rod.

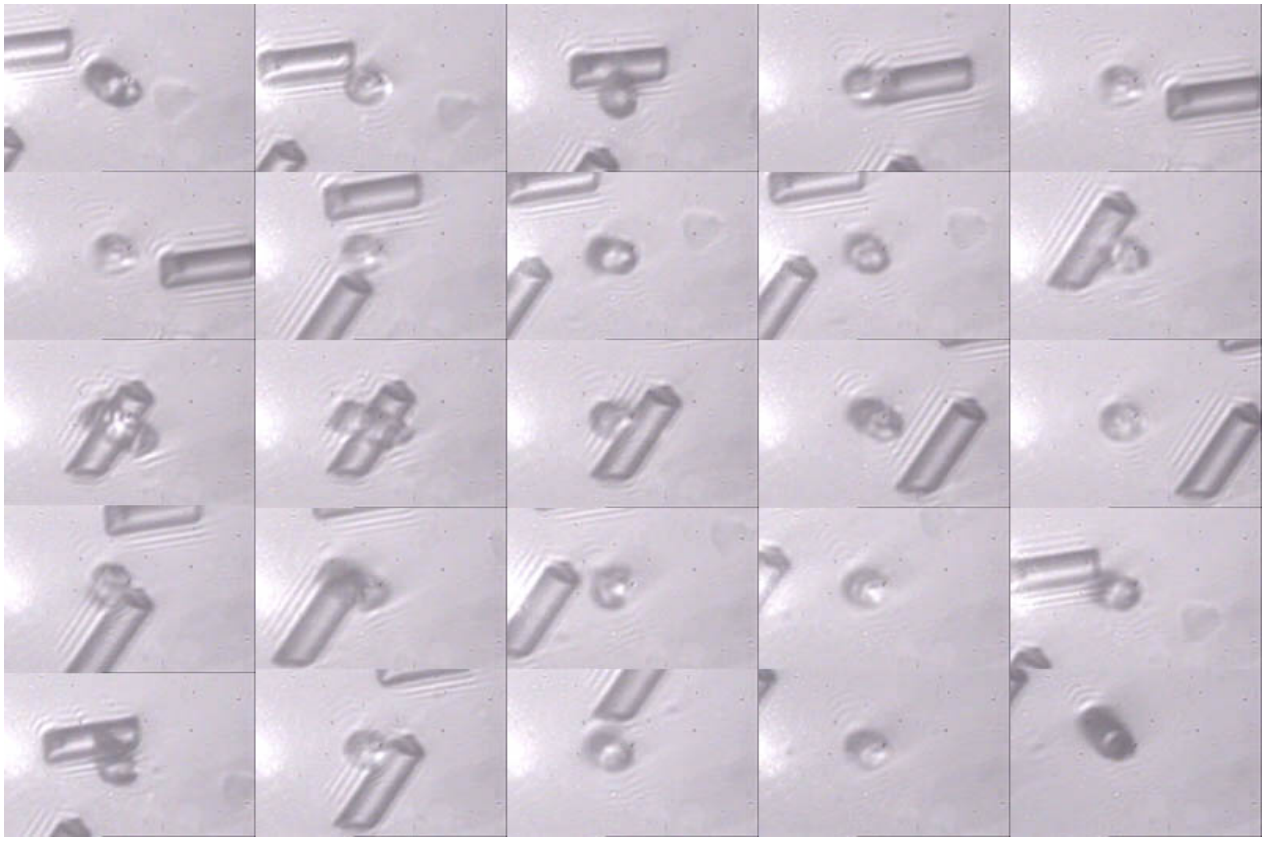

Figure 4.16 the micro-cylindrical object rotated in longitudinal plane and moved in transversal plane while it stands on its one end by laser beam.

4. 4 **Discussions and future work**

In the previous section, we discussed how optical combing may improve the recovery results of retina reattachment surgery. However, scanning the focused laser beam back and forth in one direction is only the easiest design to realign the misplaced photoreceptor. An optical tweezers array can be an alternative solution to optical combing. Several different implementation designs of optical tweezers arrays have been reported recently: dynamic holographic optical tweezers can create several high-quality optical traps in arbitrary 3D configurations and have the advantage of dynamically reconfiguring optical trap patterns under computer control[26, 27]; SLM(spatial light modulator) also provides a convenient way to obtain optical tweezers arrays with only one laser source. The use of addressable liquid crystal phase shifting arrays allows for the dynamic reconfiguration of a tweezers array for active particle manipulation [28]. Other diffractive optics can replace liquid crystal phase shifting arrays to generate three-dimension arrays of traps. Scanning a single tweezers rapidly among a number of positions to create a time-averaged extended trapping pattern is another solution [29].

Another relatively new finding shows that it is possible to controllably rotate or align microscopic particles of nonabsorbing material in a TEM00 Gaussian beam trap. The only requirement is that the particle is elongated along one direction[30]. Light can carry angular momentum as well as linear momentum, and a laser beam carries angular momentum in two distinct forms: spin angular momentum, associated with the polarization of the beam; and orbital angular momentum, associated with the spatial structure of the beam. Torque results from the scattering of light if either the orbital angular momentum or the spin angular momentum is altered. This introduces the possibility to

controllably rotate or orient optically trapped micro particles by using a plane-polarized beam to align the particle with the plane of polarization. A rotating plane-polarized beam can rotate the particle at a controllable rate, or a circularly polarized beam can rotate the particle with constant torque. Thus, this method can be used to rotate or align a wide range of naturally occurring particles, including photoreceptors.

Optical tweezers have a great potential to accelerate the recovery of the retina reattachment surgery. However, we still have several obstacles to tackle with before we can finally achieve the targets.

First, the trapping force of the focused infra-red laser beam has to be strong enough to comb the photoreceptor. The radius of the retina is several micrometers. The trapping force decreases when dealing with small objects and working at long wavelength. There is a difference between the human retina and the one trapped by optical tweezers[22]. The salamanders they studied have the largest known vertebrate cells. Salamander photoreceptors, for instance, measure approximately 15um in diameter and 30um in length excluding the outer segment and synaptic terminal. The outer segment of rod cells adds an additional 40um of length and the terminal extends another 10um making an intact rod cell approximately 80um long. We tried to use a multimode laser diode because it can generate stronger laser power (up to 4W). However, the beam pattern of the multimode laser diode has a very large divergent angle and rectangular shape. We can couple around 100mW of laser power into the back aperture of the objective lens, which is larger than what we can get by using the Nd:Yag laser, but the beam pattern is not symmetric, therefore it does not work well to trap small objects.

Second, to comb the retina in situ, we have to use an objective lens with a long working distance instead of the oil-immersed or water-immersed objective lens. Figure 4.17 shows the structure of the human eye. The retina is inside the eye. It can not be accessed by normal oil-immersed objective lenses which generally have a working distance of several millimeters. In our experiment, we have used an objective lens with a long working distance (Mitutoyo Mplan 80x N.A. 0.6, LWD 15mm). It has a smaller numerical aperture compared with "wet" objective lens. From the simulation results, we already know that the trapping force decreases if the numerical aperture of the objective lens decreases. In our experiment, we can still trap the micro-rod with a long working distance objective lens, but with higher incident laser power. However, this is a problem for our optical combing design because higher laser light power causes photo damage to the sample.

In contrast to the relatively transparent neurons, melanin absorbs light strongly in visible wavelengths and near infrared wavelengths. It is reported that retinal-pigmented epithelial cells can easily get heated and even exploded when illuminated by focused laser light [22]. Melanin is in the iris in the front of the eye and also in the back of the eye, behind the retina. The light arriving at the macula consists of image-carrying rays as well as light that has been reflected repeatedly by the inside wall of the eye. These reflected rays induce a type of glare called "veiling" that compromise vision. Ocular melanin reduces glare therefore minimizing veiling in a manner similar to the black paint inside a common camera by reducing the internal reflections of light in the eye. Without this "black paint", there would be significant light scatter inside the eye and subsequent loss of contrast.

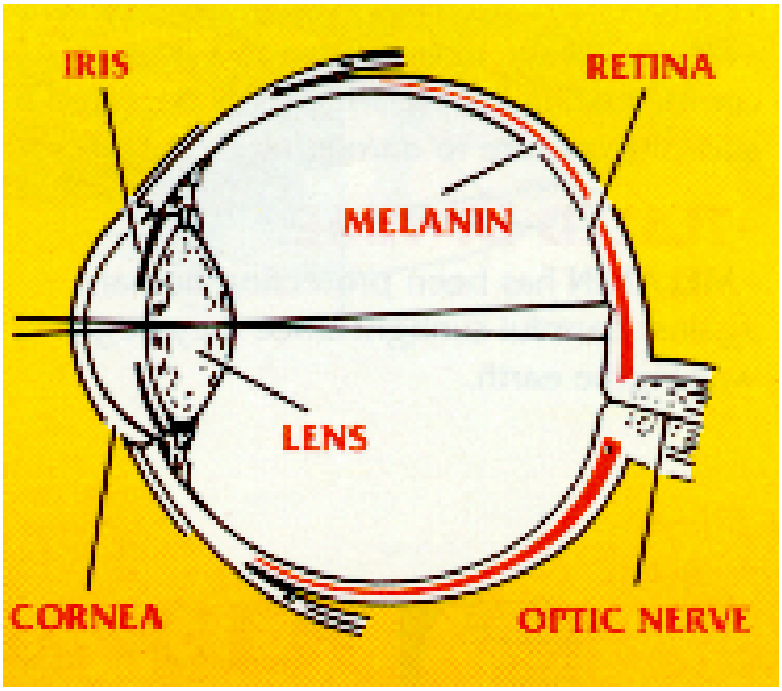

Figure 4.17 Schematic of the human eye.

The function of melanin could cause problems if 'optical combing' is used as the post-surgery treatment of retina-reattachment operation. Damage to the retinal tissue occurs by absorption of light and its conversion to heat by the melanin granules in the pigmented epithelium or by photochemical action to the photoreceptor. The absorption coefficients of melanin and other materials in the optical/NIR (400–1100nm) range are shown in Figure 4.18 [31, 32].

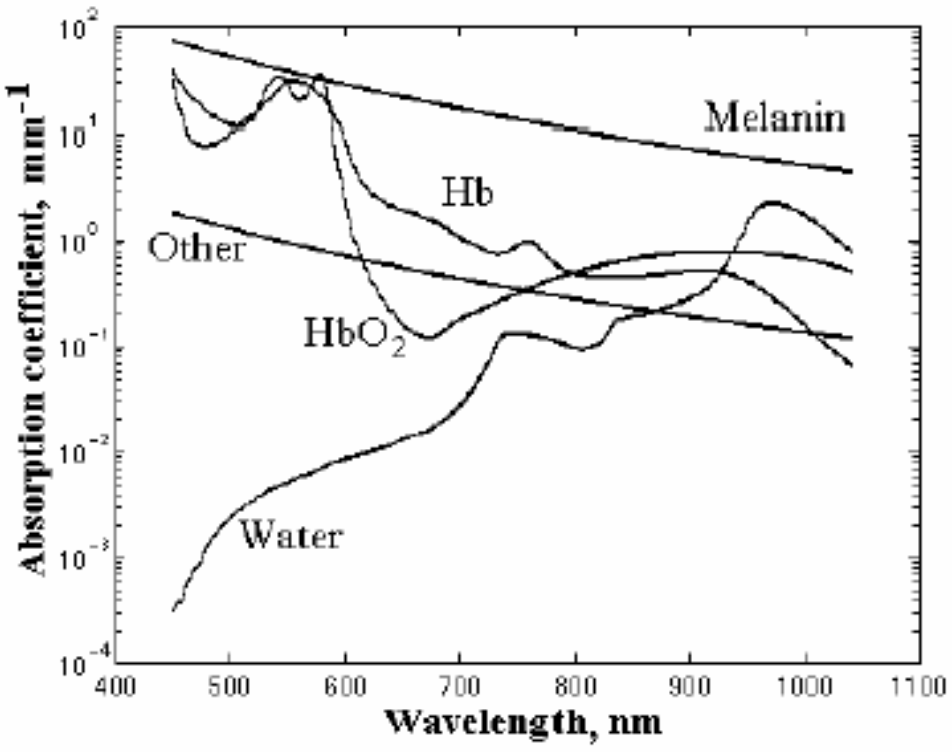

Figure 4.18, Absorption coefficients of oxy-, deoxyhaemoglobin and water as a function of wavelength

We have to search for a proper window of laser power which is strong enough to exert the appropriate trapping force onto the photoreceptors, at the same time it has to be small enough to prevent the thermal damage caused by melanin absorption. Scanning speed is another factor. If we could scan the laser beam quickly, we could decrease the heat accumulation and alleviate the damage. On the other hand, 'optical combing' requires accurate positioning to comb the photoreceptors in situ.

4.5 Conclusions

We reported a novel post surgery treatment, optical combing, to enhance the visual outcome in retina reattachment surgery. The major research question addressed in this study is weather optical combing is a viable technique for retinal realignment. In optical combing, optical trapping force by tightly focused light is used to align the photoreceptors in detached retinas by scanning the focused laser beam back and forth. This treatment would help to enhance photoreceptors realignment, therefore improving the vision recovery of surgery.

We first discussed how detached retinas reduce human vision. After that, a literature review on optical tweezers was presented. Previous work on trapping retinal neurons by optical traps was introduced, which provided the experimental basis for our project. Another important topic, the localized cell heating caused by the focused laser radiation, was also discussed. A ray-optics model was then given to describe the forces exerted on a dielectric micro-cylindrical object in a single-beam gradient force optical trap. We discussed the interaction between the TEM_{00} Gaussian beam and cylindrical micro-objects. The trapping force was modeled and simulated. An experimental setup was also build and applied to manipulate the micro-cylindrical objects to prove the feasibility of the design. We successfully trapped and rotated the micro-cylindrical objects in both the transversal plane and longitudinal plane. Experiment results confirmed that optical combing would be an effective tool to align the misaligned photoreceptors because they have similar optical properties, such as transparency and shape, with micro-cylindrical objects. We then applied optical combing to align the photoreceptors of bovine retina sample. Our experimental results showed it is difficult to identify the aligning results of optical combing because the bovine retina sample has a

thickness of 3-4 millimeters. The photoreceptors can not be imaged with enough contrast by a conventional optical microscope. To clearly monitor the experimental results, a confocal microscope is recommended to improve the imaging quality. Finally, we addressed some obstacles met during the study and the possible solutions which are the future works to further this study. Other optical tweezers designs that can be potentially applied to optical combing are also introduced.

References

1. Kroll AJ, M.R., *Experimental retinal detachment and reattachment in the rhesus monkey:electron microscopic comparisons of rods and cones.* Am J Ophthalmol, 1969. **1969:68**: p. 58-76.
2. R., m., *Experimental retinal detachment in the owl monkey, II:histology of retina and pigment epithelium.* Am J Ophthalmol, 1968. **1968:66**: p. 396-410.
3. Enoch JM, V.L.J.J., Okun E., *Realignment of photoreceptors distrurbed in orientation secondary to retinal detachment.* invest ophthalmol, 1973. **12**: p. 849-853.
4. Miyake Y, S.N., Ota I, Horiguchi M., *Local macular electroretinographhic responses in idiopathic central serous chorioretinopathy.* Am J Ophthalmol, 1988. **106**: p. 546-550.
5. Ashkin, A., *Acceleration and trapping of particles by radiation pressures.* Phys. Rev. Letter, 1970. **24**: p. 156-159.
6. Ashkin, A.D., J.M., *Optical trapping and manipulation of single living cells using infra-red laser beams.* Ber. Bunsen-Ges. Phys. Chem., 1989. **98**: p. 254-260.
7. Ashkin, A.D., J.M., *Forces of a Single-beam gradient laser trap on a dielectric sphere in the ray optics regime.* Methods in cell biology, 1998. **55**: p. 1-27.
8. Block, S.M., *Compliance of bacterial flagella measured with optical tweezers.* Nature, 1989. **338**: p. 514-518.
9. Block, S.M., Goldstein, L.S., *bead movement by single kinesin molecules studied with optical tweezers.* Nature, 1990. **348**: p. 348-352.
10. M.I.Mishchenko, J.W.H.a.L.D.T. *Light Scattering by Nonspherical Particles: Theory, Measurements, and Applications*. in *Academic*. 1999. Sasn Diego, Calif.

11. S.C.Hill, P.W.B.a., *Light scattering by Particles:computation methods*. 1990: world scitific.

12. Gauthier, R.C., *Experimental confirmation of the optical-trapping properties of cylinderical objects.* Applied Optics, 1999. **38**(22): p. 4861-4869.

13. A.Ashkin, *Optical trapping and manioulation of singel cells using infrared laser beams.* Nature, 1987. **330**: p. 769.

14. M.W.Berns, L.Y.G.J.S., *Physiological monitoring of optically trapped cells:assessing the effects of confinement by 1064-nm laser tweezers using microfluorometry.* Biophys. J., 1996. **71**: p. 2158-2167.

15. Konig, K.H.L.M.W.B., *Cell damage by near-IR microbeams.* Nature, 1995. **377**: p. 20.

16. Konig, K., H.Liang, M.W.Berns, *Cell damage in near-infrared multimode optical traps as a result o fmultiphoton absorption.* Opt. Lett., 1996a. **31**: p. 1090-1092.

17. S.M.Block;, K.S., *Biological applications of optical forces.* Annu. Rev. Biophys. Biomol. Struct., 1994. **23**: p. 247.

18. Y.Liu; D.K.Cheng, G.J.S., M.W.Berns,, *Evidence for localized cell heating induced by infrared optical tweezers.* Biophys. J., 1995. **6**: p. 2137-2144.

19. Konig, K., Tadir Y, Patrizio P, Berns MW, *Effects of ultraviolet exposure and near infrared laser tweezers on human spermatozoa.* Hum Reprod, 1996. **11**: p. 2162-2164.

20. Liang H, V.K., Krishman P, Trang TC, Berns MW, *Wavelength dependence of cell cloning efficiency after optical trapping.* Biophys. J., 1996. **70**: p. 1529-1533.

21. Dai J, S.M., *Mechanical properties of neuronal growth cone membranes studied by tether formatin with laser optical tweezers.* Biophys. J., 1995. **68**: p. 988-996.

22. E. Townes-Anderson, R.S.S.J., D.M. Sherry, J.Lichtenberger, M.Hassanain, *Mircromanipulation of Retinal Neurons by optical tweezers.* Molecular vision, 1998. **4**: p. 12.

23. Ashkin, A., Biophys. J., 1992. **61**: p. 569.

24. W.H. Wright, G.J.S.a.M.W.B., Applied Optics, 1994. **33**: p. 1735.

25. Hyun-ik kim, I.-J.J., Seok-ho Song, Pill-soo Kim, *Dependence of the opotical trapping efficiency on the ratio of the Beam Radius-to-the Aperture radius.* Journal of the Korean Physical Society, 2003. **43**(3): p. 348-351.

26. Dufresne, E., *Computer-generated holographic optical tweezer arrays.* Review of Scientific Instruments, 2001. **72**: p. 1810-1816.

27. Jennifer Curtis, B.K., *Dynamic holographic optical tweezers.* Optics Communications, 2002. **207**: p. 169-175.

28. M.Reicherter, T.H., Opt. Lett., 1999. **24**: p. 608.

29. Sasaki, K., Opt. Lett., 1991. **16**: p. 1463.

30. Alexis I. Bishop, T.A.N., Norman R. Heckenberg, *Optical application and measurement of torque on microparticles of isotropic nnonabsorbing material.* Phys. Rev. Letter A, 2003. **68**(033802).

31. Thompson CR, Gerstman BS, Jacques SL, Rogers ME, *Melanin granule model for laser-induced thermal damage in the retina, Bull Math Biol 1996 Jul; 58 (4): 809-810*

32. SA Prahl, SL Jacques, "Sized-fiber spectroscopy", SPIE proceedings of Laser Tissue interaction IX, VOL 3254, pp.348-352, SPIE Bellingham, 2000

APPENDIX A

LABVIEW CODES AND GUIS

Appendix A1: Block Diagram of FDM confocal microscope Labview data collection program

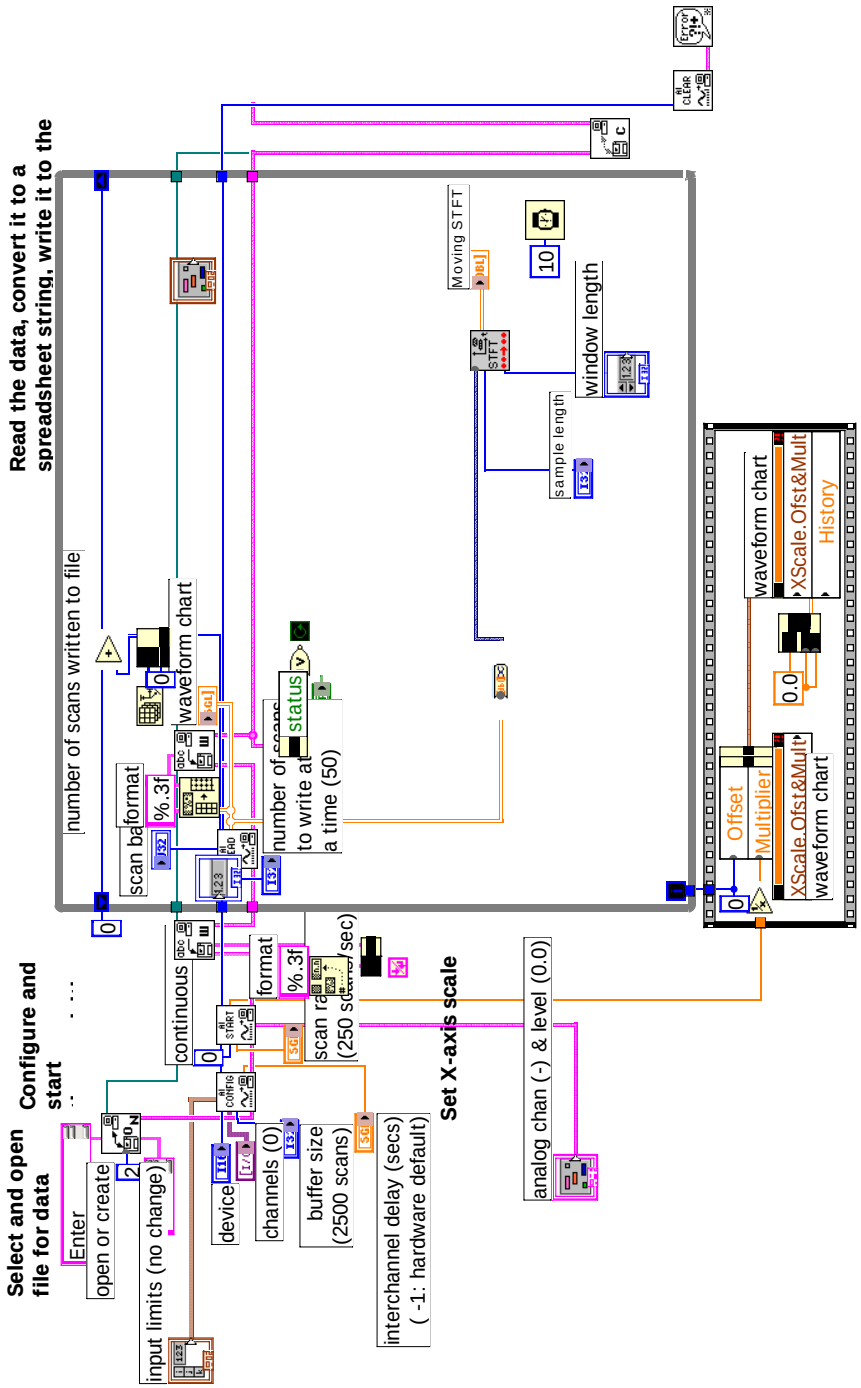

Appendix A2: Front panel of FDM confocal microscope Labview data collection program

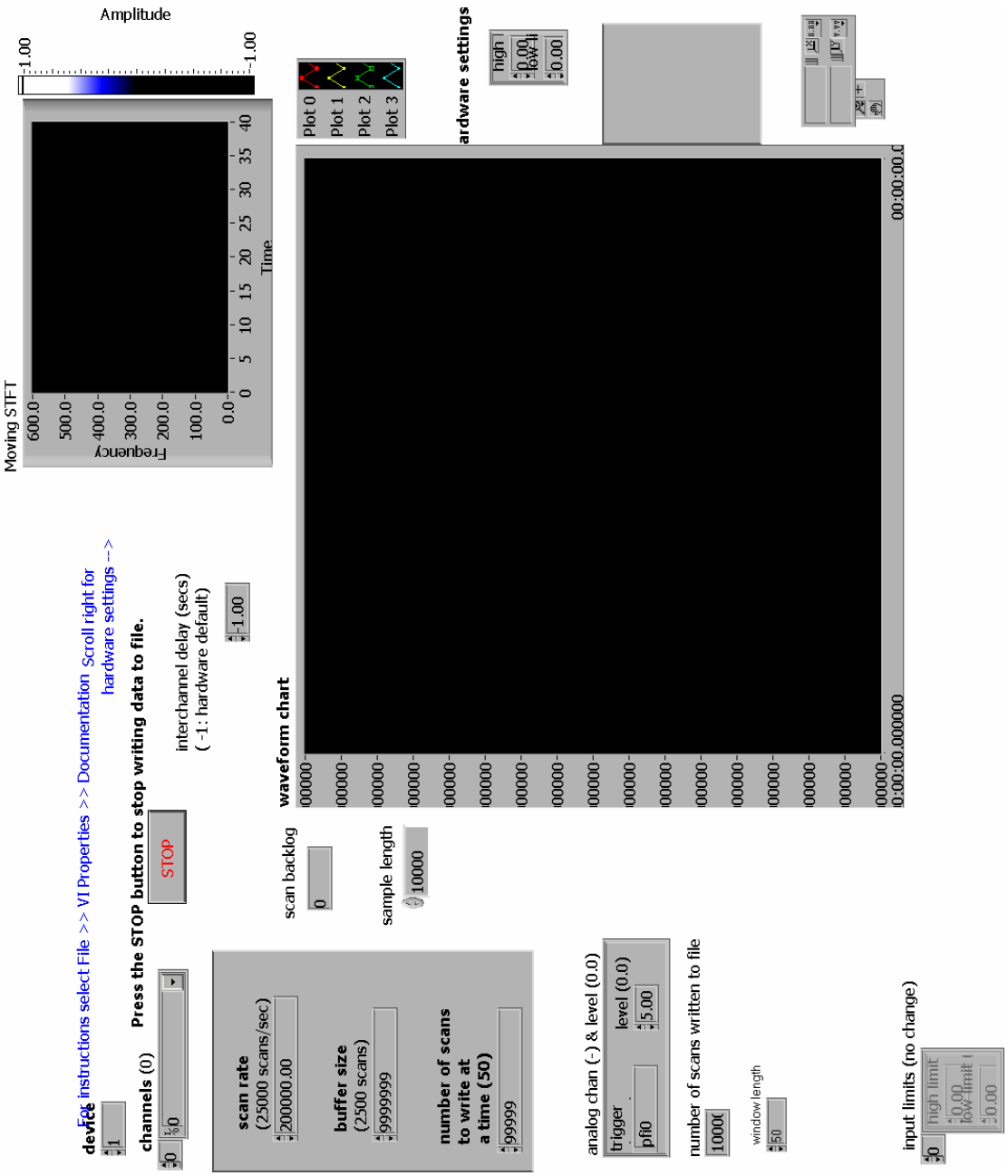

Appendix A3: Labview code of Function Generator to control data collection time and synchronization between optical shutter and NI DAQ controller.

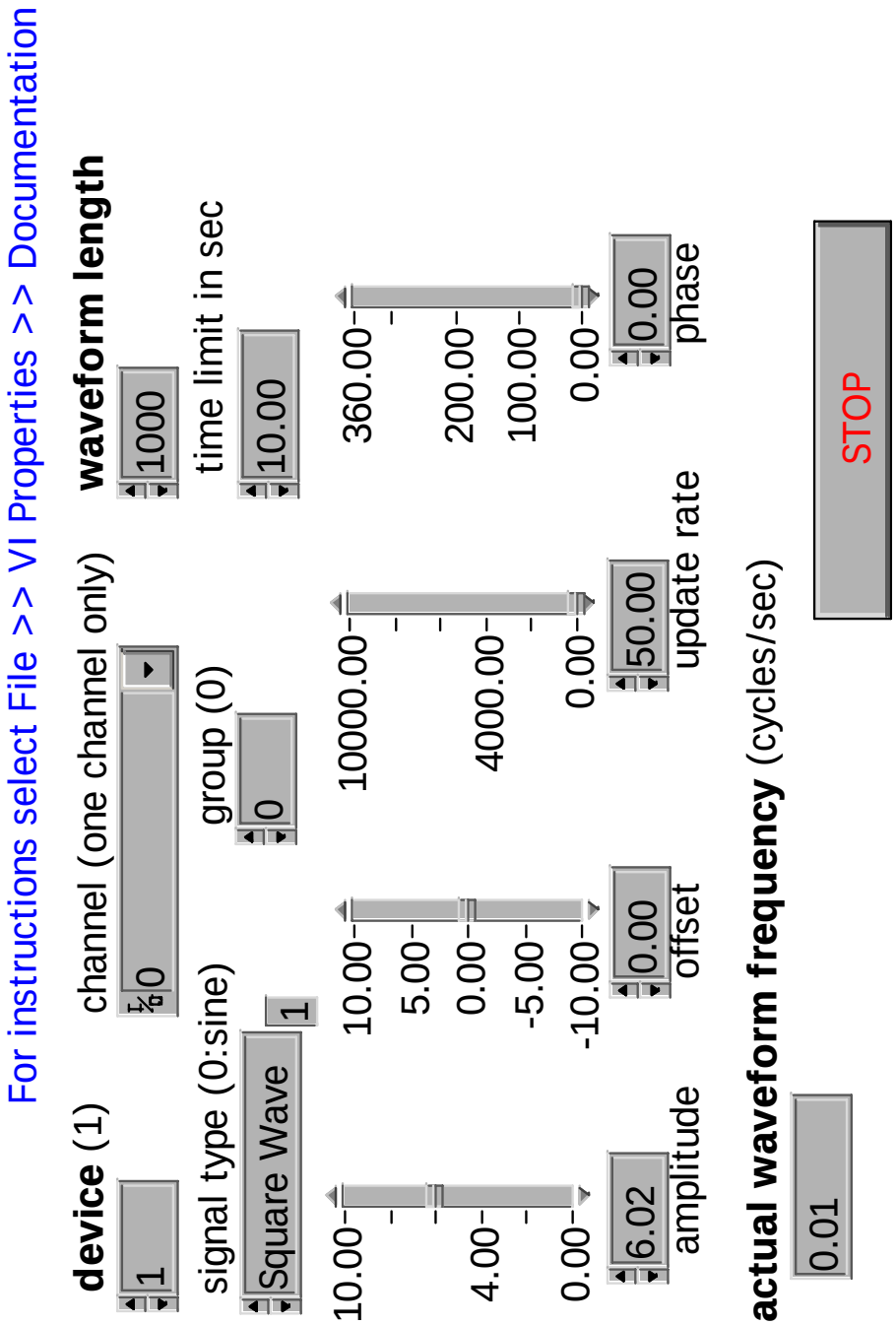

APPENDIX B

MATLAB CODES FOR OPTICAL TRAPPING FORCE SIMULATION

```
%%%%%%%%%%%%%%%%%%%%%%%%%%%%%%%%%%%%%%%%%%%%%%%%%%%%%%
% This function calculate the transversal trapping force by optical tweezers
%%%%%%%%%%%%%%%%%%%%%%%%%%%%%%%%%%%%%%%%%%%%%%%%%%%%%%

function fr_sph=fr_sph(x,y,p,zw,rw)
% this code deals with the case that lowest order guassian beam incident in Z direction, with the highest intensity %
% locates at (xw,yw,zw), that is saying that the beam waist is at plane (xx,yy,zw). The cylinder with the central axis aligns %
% with the X axis, which means the cylinder aligned perpendicular to the laser beams's propagation axis. %
% coordinate, z axial direction, x is theta1 %
% xx,yy,zz are the variable of coordinate. %
global rad;

% reflective index %
n0=1.3333;
ns=1.55;

% parameters about the incident beam    %
   lanbda=0.514; % mircometer

% this part is an example about lowest mode of Gaussian beam %
   w0=2;          % 0.5 mircometer %
   zz0=pi*(w0^2)/lanbda;
   ww=w0*sqrt(1+((zw-rad)/zz0)^2);
isph1=2.*p.*exp(-2.*(rw^2+rad^2.*(sin(x).^2)+2*rw*rad.*sin(x).*cos(y))./ww.^2)/(pi.*ww.^2);


   % parameters about the reflectance & transmittance coefficient %
   % rte and rtm are the complex amplitude reflectance for TE adn TM polarization %
   % we assume that photon stream can be considered to be composed of an equal number%
   % fphotons in both polarizations  rr= (abs(( rte + rtm )/2))^2 %
   % theta2=asin(sin(x)*n0/ns)

   rr4=(n0.*ns).^2.*((cos(x)).^2-(cos(asin(sin(x)*n0/ns))).^2).^2;
   rr5=n0*ns*(cos(x).^2+cos(asin(sin(x)*n0/ns)).^2);
   rr6=(n0.^2+ns.^2).*cos(x).*cos(asin(sin(x)*n0/ns));
   rr1=rr4./((rr5+rr6).^2);
   tt1=1-rr1;
   rr2=rr1;
   tt2=tt1;
```

```
% % Radial force
    f1rr=n0.*sin(2.*x).*rr1;
    f1tr=ns.*sin(x-asin(sin(x)*n0/ns)).*tt1;
    f2rr=2*ns.*sin(x-asin(sin(x)*n0/ns)).*tt1.*rr1;

    fr_sph=(-f1rr+f1tr-f2rr).*10000.*(rad.^2).*sin(2.*x).*(isph1).*cos(y)/3;
```

```
%%%%%%%%%%%%%%%%%%%%%%%%%%%%%%%%%%%%%%
% This code draw the meshed figure of trapping force vs. transversal
% displacement
%%%%%%%%%%%%%%%%%%%%%%%%%%%%%%%%%%%%%%

global rad;
rad=5;  %radius of cylinder %
zw=10;

%for rw=1:10,
   %rsph(rw)=dblquad(@fr_sph,0,pi/2,0,2*pi,[],[],0.025,zw,rw-1);
   %end

for yw=-10:10
   for xw=-10:10,
      zf(xw+11,yw+11)=dblquad(@fr_sph,0,pi/2,0,2*pi,[],[],0.05,zw,xw,yw);
   end
end
[X,Y]=meshgrid(1:21,1:21);
mesh(X,Y,zf);

title('Plot of the radial force vs rw (sphere)')
xlabel('xw, central point of beam')
ylabel('yw, central point of beam')
zlabel('radial force (pN)')
clear all;
```

```
%%%%%%%%%%%%%%%%%%%%%%%%%%%%%%%%%%%%%%%%%%%%
% This code calculates the axial force caused by the focused Gaussian beam
%%%%%%%%%%%%%%%%%%%%%%%%%%%%%%%%%%%%%%%%%%%%

function force=axial(x,y,xw,yw)
% coordinate, z axial direction, x is thta1 %
global z;

% reflective index %
n0=1.3333;
ns=1.5468;

% radius of the bean %
%rad=1.5;
rad=8;

% parameters about the incident beam    %
   lanbda=0.514; % nanometer

% this part is an example about lowest mode of Gaussian beam %
   p=0.05;      %total power in the beam 20mw%
   w0=2;           %2 mircometer%
   z0=pi*(w0^2)/lanbda;
   ww=w0*sqrt(1+((z-rad)/z0)^2);
i=2*p*exp(-2.*((rad.*sin(x).*sin(y)-yw).^2+(rad.*sin(x).*cos(y)-xw).^2)./ww.^2)/(pi.*ww.^2);


   rr4=(n0.*ns).^2.*((cos(x)).^2-(cos(asin(sin(x)*n0/ns))).^2).^2;
   rr5=n0*ns*(cos(x).^2+cos(asin(sin(x)*n0/ns)).^2);
   rr6=(n0.^2+ns.^2).*cos(x).*cos(asin(sin(x)*n0/ns));
   rr1=rr4./((rr5+rr6).^2);
   tt1=1-rr1;
   rr2=rr1;
   tt2=tt1;

% Axial Force
   i1rz=n0.*(1+cos(2.*x)).*rr1;
   i1tz=(n0-ns.*cos(x-asin(sin(x).*n0./ns))).*tt1;
   force=-10000.*i.*rad.^2.*sin(2.*x).*(i1rz+i1tz)./6;
```

```
%%%%%%%%%%%%%%%%%%%%%%%%%%%%%%%%%%%%%%
% This code draw the meshed 3D figure of axial force vs. transversal
% displacement.
%%%%%%%%%%%%%%%%%%%%%%%%%%%%%%%%%%%%%%

global z;
z=10;

for yw=-10:10
   for xw=-10:10,
      zf(xw+11,yw+11)=dblquad(@fz,0,pi/2,0,2*pi,[],[],xw,yw);
   end
end
[X,Y]=meshgrid(1:21,1:21);
mesh(X,Y,zf);

title('Plot of the Z-axis force vs (xw,yw)')
xlabel('xw, central point of beam')
ylabel('yw, central point of beam')
zlabel('Z-axis force (pN)')
clear all;
```

VITA

Fei Wu

March 26, 1973	Born at Beijing, People's Republic of China
1990-1994	Majored in Electrical Engineering, Nanjing Institute of Science and Technology, China
1995-1998	System Engineer, AT&T China Co. Ltd.
1999-2000	Research Assistant, Applied Research Laboratory, Penn State University
2001-2002	Application Engineer, International division, Hughes Network Systems
2002-present	Research Assistant, Department of Electrical Engineering, Penn State University

FIELD OF STUDY

Major Field: Electro-optical Research
Professional Society: The International Society for Optical Engineering (SPIE) student member

PUBLICATIONS

Fei Wu, Xueqian Zhang, Joseph Cheung, Kebin Shi, Zhiwen Liu, Stuart Yin, Paul Raffin, Frequency division multiplexed multi-channel fluorescence confocal microscope, Sep. 2006 in *Biophysics Journal*.

Stuart Yin, Jae Hun Kim, Fei Wu, Paul Ruffin, Ultra-fast speed, low grating lobe optical beam steering using unequally spaced phased array technique, *Journal Optical Communication*, 2005

Fei Wu, Jae Hun Kim, Stuart Yin, Terahertz and Supercontunuum generation by ultrafast laser pulses, *Proc. SPIE Int. Soc. Opt. Eng*. 6314-66 (2006)

Fei Wu, Kebin Shi, Stuart Yin, Zhiwen Liu, 3D method via time and spatially multiplexed confocal microscope, *Proc. SPIE Int. Soc. Opt. Eng*. 6000-11 (2005)

Fei Wu, Yi Yang, Stuart Yin, High precision fiber taper fabrication using the immersion depth control in chemical etching, *Proc. SPIE Int. Soc. Opt. Eng 5911-34* (2005)

Shizhuo Yin, Thomas W. Gardner, Fei Wu and Milind Cholker, Optical combing to align photoreceptors in detached retinas, *Proc. SPIE Int. Soc. Opt. Eng. 5314-298* (2004)

Stuart Yin, Jae Hun Kim, Fei Wu, Paul Ruffin, Claire Luo, Ultra-fast speed, low grating lobe optical beam steering using unequally spaced phased array technique, *Proc SPIE Int. Soc. Opt Eng 5911-04* (2005)